PERGAMON

Renewable and Sustainable Energy Reviews
3 (1999) 77–184

RENEWABLE
& SUSTAINABLE
ENERGY REVIEWS

A review of progress in thermophotovoltaic generation of electricity†

T.J. Coutts*

National Renewable Energy Laboratory, Golden, Colorado 80401, U.S.A.

Received 15 September 1998; accepted 18 September 1998

1. Introduction

1.1. Basic concepts

This review paper discusses thermophotovoltaic (TPV) generation of electricity. It is intended for reading by those seeking an overview of the state-of-the-art of the field, rather than for the specialist. It draws heavily on the proceedings of recent conferences in the subject (in particular, on the Proceedings of the Third National Renewable Energy Laboratory (NREL) Conference on Thermophotovoltaics) and on historical references from an earlier time when TPV appeared an attractive option for the generation of electricity.

TPV devices convert radiation using exactly the same principles as do photovoltaic (PV) devices; namely photons of radiation are absorbed by a semiconductor *p*/*n* junction (a diode), which causes the generation of excess electrical charge. The excess photogenerated positive and negative charge is separated by a combination of

---

† I began writing this paper immediately after the Third NREL Conference on Thermophotovoltaic Generation of Electricity, which was held in May 1997, and intended the review to provide a general overview of TPV and of key papers presented at this conference. Given the length of the paper and the amount of time taken in its writing, subsequent events have outdated some of the material included in the latter category. Publications at the Fourth TPV Conference in October 1998 indicated that significant progress had been made in the field since the Third Conference and I recommend that those interested read the proceedings of the Fourth conference, once again published by the American Institute of Physics. Nevertheless, the more general information in this review remains relevant and, hopefully, timely. In my opinion, the most significant evidence of recent progress is: increased international interest; a broader appreciation of the importance of the need for careful and complete characterization of materials, devices, and systems; substantial gains in fundamental understanding and performance of the quaternary alloy GaInAsSb; the introduction of new radiator concepts; and more attention being paid to modeling of both real and conceptual systems. There was also further evidence of interest in non-military applications, particularly from the European and Japanese attendees.

* Corresponding author. Tel.: 001 303 384 6561; fax: 001 303 384 6430; e-mail: tim_coutts@nrel.gov

PII: S1364-0321(98)00021-5

diffusion to and drift across the electrostatic junction. This process establishes a potential difference between the two sides of the junction. The magnitude of the potential difference depends on the external load; if this is infinite, the open-circuit voltage is established; if it is shorted, then the voltage is zero and the short-circuit current is delivered to the external circuit. At some point between these two extremes of the current/voltage characteristic, the power delivered to the external circuit is maximized.

The key differences between PV and TPV conversion are the temperatures of the radiators and the system geometries. In a PV device (a solar cell) the radiation (more or less, blackbody) is received from the sun at a temperature of about 6000 K and at a distance of about 150×10^6 kilometers. A TPV device, however, receives radiation (either broad- or narrow-band) from a surface at a much lower temperature (1300–1800 K being considered the practical feasible range) and at a distance of perhaps only a few centimeters. Although the blackbody power radiated by a surface varies as the fourth power of the absolute temperature, the inverse square law dependence of the power received by the detectors dominates. Hence, whereas the power received by a non-concentrator solar cell is of the order of 0.1 W cm^{-2}, that received by a TPV converter is likely to be 5–30 W cm^{-2}, depending on the radiator temperature. Consequently, the power density output from a TPV converter is expected to be significantly greater than that from a non-concentrator PV converter. This will be discussed in greater detail in Section 2, which deals with irradiance. The information will subsequently be used in converter modeling, which is discussed in Section 3.

1.2 Recent developments

The study of TPV conversion dates back about 30 years, but there has been a resurgence of interest during the last few years, mainly because of the availability of high-performance converters. There is presently widespread interest in the United States (U.S.A.) and, although interest elsewhere is limited [1], there is evidence [2, 3] that it is growing. In the U.S.A., several entrepreneurial companies have been founded, and there is growing interest from much larger aerospace companies. Several government agencies in the U.S.A. are now funding projects in TPV, mainly but not exclusively, through SBIR (Small Business Innovative Research) grants. Three conferences [4, 6] have been organized by NREL, and both the Army Research Office (ARO), and the Defense Advanced Research Projects Administration (DARPA) have organized workshops [7, 8]. These were organized with the specific objectives of helping the sponsoring organizations define the potential of TPV for military applications. Finally, the number of papers on TPV, presented at the IEEE Photovoltaic Specialists Conference, has increased significantly during the last five years, from two to ten (see, for example [9]). A thorough bibliography of publications in TPV was published by Broman [10] several years ago.

The technology has benefited considerably from the successes of the High-Efficiency Solar Cells program of the U.S. Department of Energy and, in particular, from work on III–V semiconductor devices. Several PV devices with conversion efficiencies of greater than 30% have now been made by research groups at NREL and elsewhere

[11, 12] and the techniques developed are now being applied to TPV converters. In addition, high-quality silicon devices are commercially available, and several approaches use these [13, 14]. Although the cost of TPV devices and systems are initially likely to be high, the military niche market may be prepared to pay a premium for the strategic advantages offered by TPV. This may ultimately benefit non-military markets, which will inevitably be even more sensitive to costs. Market studies, which will be discussed in more detail later, show that there is a wide diversity of both military and non-military markets, and it seems likely that the total value of these (in the relatively near future) might be of the order of $1Bn per annum [15].

1.3. Potential advantages

The potential advantages offered by TPV systems include the following (not necessarily limited to this list):

(i) High power-density outputs. Power densities of greater than 1 W cm^{-2} have been achieved, but potentially, this could be increased to 2–3 W cm^{-2}.
(ii) Supply and demand are always in phase. Unless storage is available, a solar cell can only produce electricity while the sun is shining. This is a distinct advantage for TPV systems. Hybrid systems using both PV and TPV, which would capitalize on the advantages of both technologies, may also be feasible.
(iii) Versatile fuel-usage. In principle, any fuel, including nuclear, may be used to heat the radiant surface.
(iv) Lightweight. This may be expected because of the high power densities, although this attribute has not yet been demonstrated.
(v) Quiet. There are no moving parts, so the generation process should be silent. This may be of strategic advantage for military applications, but may also be appealing for various non-military applications, such as power supplies for recreational vehicles.
(vi) Low maintenance. This advantage is claimed because no moving parts will be involved. On the other hand, little experience is available for systems operating under the high temperatures expected to be used.
(vii) Safe. Although claimed, this is somewhat speculative at present.
(viii) Pollution-free. This assumes that clean fuels are to be burned and their flame-temperature will be less than that at which NO_x is produced.
(ix) Potential low cost. Although it has been claimed that the cost of substrates is unlikely to dominate the total cost of a TPV system [16] (in large-volume production), there may still be advantages and opportunities to develop polycrystalline thin-film systems, thereby again capitalizing on developments in DOE's National PV Program. Such possibilities have been discussed by Contreras et al. [17], who suggested using thin films of $Ga_xIn_{1-x}As$; by Dhere [18], who proposed several potential materials; and by Biter et al. [19], who suggested using copper indium diselenide ($CuInSe_2$), because this material has already been well-developed in the National PV Program. Even though the cost of typical substrates (with the exception of Si) is presently high, this is not inevi-

table. With increasing demand, the cost could decrease greatly. The comparative advantages of thin-film and single-crystal systems are, therefore, not yet clear.

(x) Possibility for cogeneration of electricity and heat. Most TPV system configurations developed to date are expected to recuperate the waste heat to maximize system efficiency. On the other hand, Sweden already exploits cogeneration in community heating schemes, and this is also a possibility for TPV [1].

Perhaps the greatest potential for TPV generation of electricity is in its application to industrial waste heat. Many industrial sectors (e.g., glass, aluminum, steel, castings) consume huge quantities of heat supplied by natural gas or electricity. The glass industry is a particularly good example. It is made clear in various reports from the industry [20] that two-thirds of the energy consumed is wasted: simply being discharged into the atmosphere, with consequent harmful heating effects. The waste heat also worsens operating conditions, as well as costing money and profits. The energy wasted apparently amounts to the equivalent of 1.0 gigawatts continuous usage for the float-glass industry alone! Recovery of even a small fraction of this energy could represent considerable energy savings to the nation and costs to the industry. The glass industry sees one of its major targets for the future as the reduction of waste heat. It seems likely that similar arguments could be made for other industrial sectors.

Although some of these applications are speculative and some are only relevant to the military, they point to some key differences between PV and TPV. Most TPV work performed to date concerns the semiconductor converters, and there is comparatively little experience with systems. Hence, the promise of TPV is encouraging but is, as yet, largely unproven. Much more work needs to be done on system demonstration. On the other hand, somewhat negative comments may still be made about PV systems, despite the large investment over the last 20 or so years. There is, as yet, only a minimal concentrator-PV industrial base, and the PV systems in use mainly operate without optical concentration. As mentioned above, the power density outputs are low and the cost of the power generated remains too high to permit large-scale penetration of domestic markets in the U.S.A. and other developed countries. However, it must be remembered that PV is well in advance of TPV: the only funding available for TPV development at present is for military applications, and this probably only for a limited investment period. Another difficulty is that, unlike PV, TPV generators will involve more distinct components and technologies including the burner, the radiator, and means of photon and heat recuperation. Very few organizations have experience in more than one of these, and it is therefore expected that partnerships will form to overcome inexperience and to maximize commercial opportunities. Another key difference is that the optimum design of a TPV system is a function of the radiator temperature, which is not a variable in PV.

In this paper, we shall first present a historical review of TPV from its beginnings some 30 years ago. This will be followed by some discussion about the nature of irradiance and, in particular, about selective radiators. Next, a brief review of elementary modeling will be given to estimate the required bandgaps of the semiconductor converters, the likely converter performance, and to help determine potentially suitable semiconductors. The fabrication and characterization of several types of converters are discussed in detail.

Both blackbody (graybody) and selective radiators will be considered, and it will become apparent that both of these require a means of recirculating long-wave photons to achieve a high system-efficiency. In Section 4, the means being considered to achieve this will be discussed. Next, we shall go on to discuss the fabrication of practical systems and review their performance, insofar as measurement of this is possible at present.

1.4. Historical background

The possibility of using infrared radiation and converting it to electricity using the photovoltaic effects was first appreciated by Aigrain [21]. Early work focused on the use of silicon (Si) PV converters and selectively emitted (narrow-band) radiation. The principles of the latter mechanism will be discussed in the next section. In brief, some materials radiate in relatively narrow wavelength bands. Their emissivities are low outside the band and high within the band. If the upper wavelength limit of the emission band is approximately equal to the bandgap of the converter, the conversion efficiency is expected to be high. The only photons present in the incident spectrum are those with energies close to that of the bandgap. The absence of high-energy photons prevents heating of the converter through thermalization of excited carriers. The absence of low-energy photons also means less converter heating, which occurs via free-carrier absorption. Consequently, if the incident spectrum can be represented by a delta function, the conversion efficiency should be high. Ideally, the radiator should have an emissivity of zero both above and below the band-edge of the semiconductor converter, and an emissivity of unity at the band-edge. The energy required to heat a selective radiator to a specific temperature would be less than that for a blackbody radiator, and the efficiency should be higher. Alternatively, the same amount of fuel will heat the selective radiator to a higher temperature, at which the electrical power density output will be greater. In general, the emissivities without and within the emission band are not zero and unity, respectively, but are much less ideal. Nevertheless, the concept is appealing; the availability of the key components (relatively low-cost Si cells and a selective radiator of ytterbium oxide, Yb_2O_3) virtually ensured that the technology made its beginnings with selective radiator-based systems. It continues to be well-favored by U.S. federal government programs.

The rare-earth series in the periodic table begins with cerium and ends with lutetium. They are not rare in the mineralogical sense; they are, in fact, plentiful and low cost. They behave selectively because of their electronic structure, as will be discussed in Section 2. The earliest solar cell technology was based on Si solar cells, which have been used from the very start of space programs, to provide space-craft power.[1] Early workers in TPV technology realized that the two essential components (silicon cells and rare-earth radiators) were available at the time the concept was first invented (see Guazzoni et al. [22], Bracewell et al. [23], Ruth et al. [24]).

---

[1] The GaInP/GaAs tandem solar cell has been well received by the space community and is presently being used on several missions, although it was developed under the aegis of the terrestrial program.

Si-based TPV has problems because it requires radiator temperatures well in excess of those of which most engineers have any experience. As will be explained in the next section, Si would be acceptable for a radiator temperature of 2000 K or greater, but the durability of radiator materials is unknown under these extreme conditions. Although all the rare-earth oxides are refractory and have very high melting points, their behavior when subjected to such high temperatures for a prolonged period, particularly when they must remain stable, is unknown. The engineering difficulties can be lessened if the radiator temperature is decreased by several 100 K, but then Si becomes even less ideal. Hence, early workers examined lower-bandgap semiconductors and, in particular, germanium (Ge) [25]. The performance, however, was relatively poor, and there are fundamental reasons to expect this. The high effective mass of electrons in Ge, compared with III–V semiconductors of similar bandgap, suggests that the reverse saturation current will inevitably be much larger and the open-circuit voltage correspondingly smaller. Additionally, Ge is a difficult material to passivate electronically, although there have been efforts to develop suitable passivating layers. Venkatasubramanian et al. [26] demonstrated that typical open-circuit voltages were less than 200 mV, referenced to a solar spectrum. It may be somewhat misleading to assume that this would improve under the much higher flux densities encountered in TPV, but the early signs are not promising. Although there may be room for improvement using passivation schemes, it seems unlikely that the performance would equal that of III–V devices of similar bandgap.

Funding for TPV languished around 1980, presumably because of the absence of a high-quality converter, and the topic only recovered when low-bandgap III–V devices became available. In the opinion of the author, this is the principal reason for the recent resurgence of interest in TPV. The III–V semiconductors are widely used in a variety of electronic and opto-electronic devices, and all aspects of their growth and device fabrication are now well-developed. The range of bandgaps extends from GaP ($E_g \sim 2.2$ eV), which is used for light-emitting diodes, to InSb ($E_g \sim 0.18$ eV), which is used for infrared detectors. The materials GaSb and $In_{0.53}Ga_{0.47}As$ both have bandgaps of about 0.73 eV and are now being used for TPV converters. In fact, it is probably safe to say that without the success of these materials, interest in TPV would still be non-existent. Further discussion of the fabrication and performance of devices based on GaSb and InGaAs, and on other semiconductors, will be deferred until Section 3.

In Section 2, we shall discuss the nature of radiation from broad-band and selective radiators. This will help explain interest in the respective technologies. In Section 3, we outline the elementary modeling used to establish the ideal bandgaps for broad-band radiators and the various semiconductors that could be used. This section will also introduce the concept of photon recirculation; this will be more thoroughly developed in Section 4. The performance of actual devices, as discussed at the Third NREL Conference on TPV, is also discussed in Section 3. In Section 4, photon recirculation is discussed in some detail, because it is such a vital part of efficient TPV systems. In Section 5, we briefly discuss modeling of the performance of systems and the performance of the rather small number of actual systems in operation. Finally, in Section 6, we summarize the material in this review paper.

2. Revisionary ideas on radiation

2.1. Introduction

The incident energy on a TPV semiconductor is provided by a radiating surface at a temperature in the approximate range of 1300–1800°C. The radiator (or emitter, as it is sometimes called) may have an emissivity that is more or less uniform across the entire spectrum, or it may be low across specific wavelength ranges and near unity in others. The first of these is known as a broad-band (blackbody or graybody) radiator, whereas the second is known as a selective radiator. If the emissivity is unity across the entire spectral range, then the surface is said to be a blackbody. We shall now discuss some of the physical properties of each of these and use the information later in modeling of devices and systems.

First, we shall discuss the reasons for two different approaches. A blackbody radiates across a wide range of wavelengths, most of which are unusable by a TPV converter. As will be seen later, if a high system efficient ($>20\%$, for example) is to be achieved, there is no option but to return these longwave photons to the radiator. Depending on how it is modeled, the ideal bandgap of a converter operating at 300–350°C (when used with a blackbody radiator) is about 0.4–0.5 eV, which does not correspond to commercially available semiconductors. Although there are several possible approaches to fabricating such semiconductor converters, an alternative is to use a selective radiator in conjunction with a wider-bandgap semiconductor. In principle, a low-cost silicon solar cell could be used if the peak of the radiated energy corresponded to its bandgap (~ 1.16 eV). With an ideal selective radiator, there would be no longwave or shortwave photons: only photons close to the bandgap energy. This would give a higher efficiency than the broad-band approach, for which both longwave and shortwave photons cause problems. Some of the longwave photons cause heating of the converter, and the remainder must be returned to the radiator. The shortwave photons, with much more than bandgap energy, also cause heating of the cell, although they generate photo-current. Neither approach has yet demonstrated its superiority.

Figure 1 shows the variation of the percentage of convertible blackbody radiation with the bandgap of the semiconductor, the temperature of the radiator being treated parametrically. For low temperatures, the percentage is relatively small, for even low-bandgap materials; but for silicon, it is less than 1%. As the bandgap decreases, the convertible percentage increases but, as will be seen in the next section, the power-density output is far less. For silicon, the broad-band approach (coupled with a low-temperature radiator) simply does not make technical sense but, in principle, the selective radiator approach does.

2.1.1 Broad-band radiators

This approach uses a radiator that behaves according to Planck's law of radiation. The radiated spectrum extends across a wide wavelength range and, for a radiator temperature of, say, 1500 K, the peak in the radiated spectrum occurs at about 2.5 μm, or an energy of about 0.5 eV. The optimum bandgap for a radiator at 1500 K is

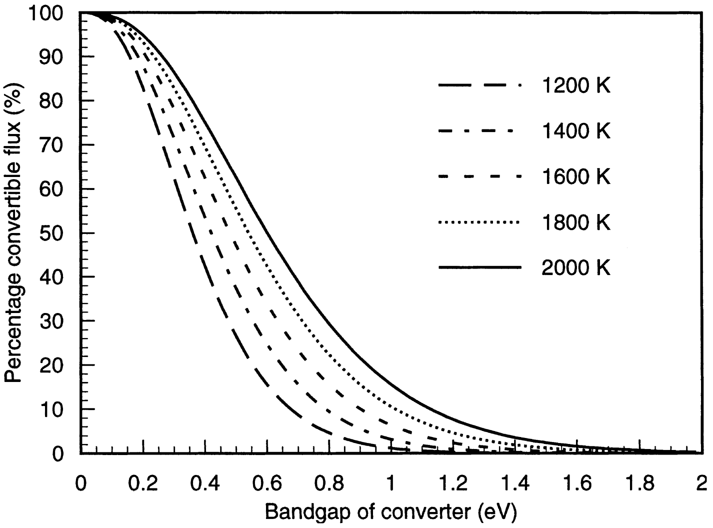

Fig. 1. Percentage of convertible flux from blackbody radiators at the temperatures shown, with the bandgap of the converter.

actually more like 0.45 eV, assuming room-temperature operation. The options for realizing this bandgap will be discussed later. The longwave tail of the Planck spectrum extends indefinitely and, even at a wavelength of 10 μm, the radiated flux (for a radiator at 1500 K) is still about 10% of the maximum. Consequently, all the photons between about 2.5–10 μm must be recirculated, the options for which are described in Section 4. In practice, photon recirculation is required for both selective and broad-band approaches because of non-idealities in the former.

2.1.2 Physical principles of broad-band radiators

Before considering modeling of TPV converters, we shall first review some ideas about radiation and discuss the differences in the fluxes, energy densities, and both energy and wavelength ranges. These make interesting comparisons with the equivalent solar quantities and illustrate the attraction of TPV.

The sun is assumed to behave as an ideal blackbody and, like any radiating object, it follows Planck's law of radiation. This gives the flux radiated per unit area, per unit bandwidth, of either wavelength or energy. The conversion between the two is straightforward and will be discussed in greater detail below. Planck's law is:

$$F(T_{\text{emit}}, \lambda) = \frac{2\pi c}{\lambda^4}\left[\exp\left(\frac{hc}{\lambda k T_{\text{emit}}}\right) - 1\right]^{-1}, \tag{1}$$

where c is the speed of light, λ is wavelength, h is Planck's constant, k is Boltzmann's constant, and T_{emit} is the absolute temperature of the radiator. The dimensions are $\text{m}^{-3}\ \text{s}^{-1}$, which, with the appropriate conversion factor, is equivalent to $\text{cm}^{-2}\ \text{s}^{-1}\ \mu\text{m}^{-1}$. For some purposes, it is useful to consider the spectral power density. This quantity may be expressed in watts cm^{-2} μm^{-1}, or watts cm^{-2} eV^{-1}. Figure 2a shows the spectral flux and energy as functions of wavelength. Figure 2b shows the same quantities as functions of photon energy. Both figures refer to a blackbody radiator at a temperature of 1500 K. Although not useful to us here, these curves are the basis

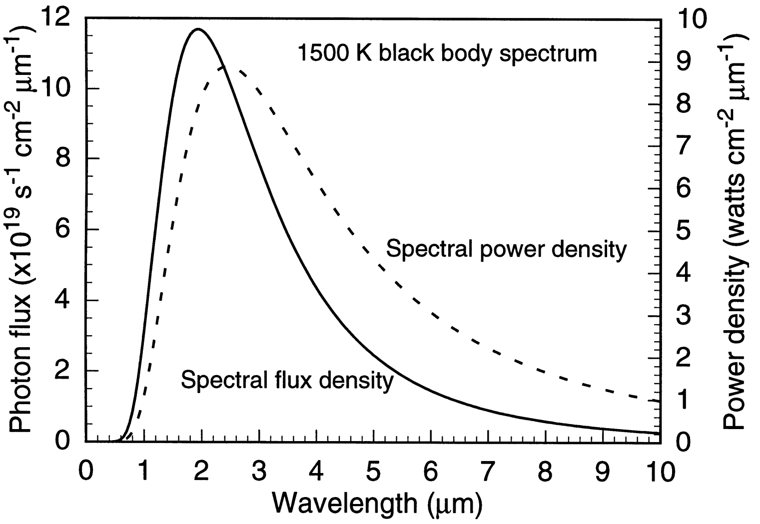

Fig. 2a. Spectral flux and power density as a function of wavelength for a blackbody temperature radiator of 1500 K.

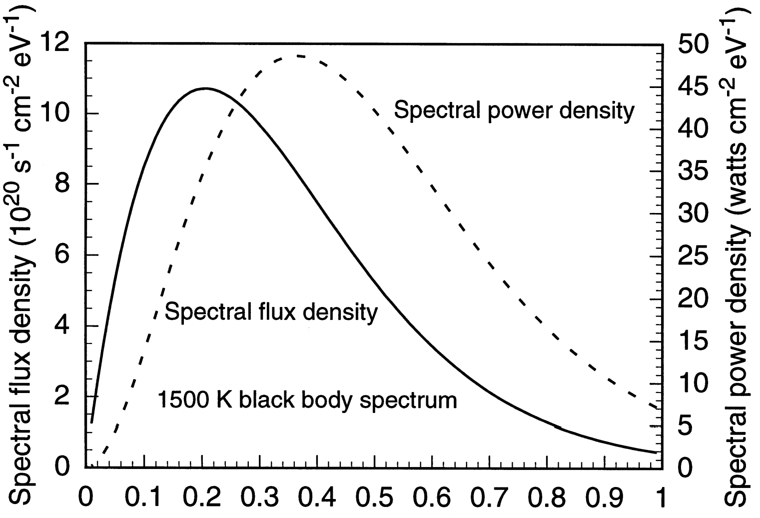

Fig. 2b. Spectral flux and power density as a function of photon energy for a blackbody temperature radiator of 1500 K.

of some of the device modeling discussed in Section 4. They also enable us to locate the regions of the radiated spectrum in which either most photons or most energy are found.

The sun is about 149.6×10^6 km from the earth, and its radius is 695.6×10^3 km. The ratio of the surface area of the sun to that of the sphere bounding the earth's orbit is 2.2×10^{-5}, which is the fraction of the radiation from the sun incident per unit area on the surface of the earth. The total energy radiated by the surface of the sun (which can be considered to be a blackbody at a temperature of 5762 K) is given by the Stefan–Boltzmann law:

$$E_r = \sigma T_{\text{emit}}^4, \tag{2}$$

where σ is the Stefan–Boltzmann constant (5.7×10^{-12} W cm^{-2} K^{-4}). Equation (2) is obtained by integration of eqn (1) over all wavelengths. As discussed below, a spectrally dependent emissivity is sometimes included in Planck's equation to allow for non-blackbody emission from the hot object.

The surface area of the sun is 1.52×10^{12} km^2 and that of the sphere, of which the earth's surface forms part, is 2.813×10^{17} km^2. Hence, the energy incident at the imaginary boundary of the vacuum of space and the earth's atmosphere is 0.135 W cm^{-2}. This is defined as the Air Mass zero (AM0) spectrum, so called because of the absence of any atmospheric absorption effects. Once the radiation passes through the atmosphere, absorption by water vapor, CO_2, and other gases reduces its intensity and by the time it reaches the surface of the earth, the total energy is about 35% less than the AM0 value.[2] In contrast, the distance between the radiating surface in a TPV conversion system and the semiconductor converter is likely to be as little as 2–3 cm. The surface itself may, or may not, be a blackbody, and its temperature is likely to be in the range of 1300–1800 K.

If the radiant surface is a blackbody, then the emissivity is unity over the entire spectral range. In a selective radiator, it is near zero for much of the spectral range, but is ideally near unity in the main emission band.

For the moment, we shall take the emissivity as unity and deal with the selective case later. At such a close distance from the radiator to the converter, the solid angle may be taken as 4π steradians for a cylindrical geometry, or 2π for a planar geometry. Using the approach used above, the total energy incident at the converter is 10–50 W cm^{-2}. This is much greater than the incident solar energy at the earth's surface, which is the major attraction of TPV.

---

[2] A knowledge of the solar flux may be of use to those attempting to design solar-powered TPV systems based on intense optical concentration. Such systems envisage heating up a radiator to temperatures in the range of relevance to TPV and using these with semiconductor converters. On the other hand, the question must be asked as to why there is any advantage in going through an intermediate stage of degrading the energy from optical to infrared wavelengths. The power density outputs would be much greater from solar cells used under optical concentration of the solar spectrum than from TPV cells using the radiation from a solar-heated infrared radiator.

2.1.3 Summary of blackbody radiators

The above material provides a background in blackbody (or graybody) radiation to help understand one of the advantages of TPV: namely, the high power densities compared with flat-panel PV. Silicon carbide (SiC) appears to be potentially useful for broad-band radiation because it has an emissivity of about 0.9 that is more or less independent of wavelength. It does not sublime until a temperature of about 2700°C, which is above the practical temperatures envisaged for radiators. Realistically, we should probably consider the upper practicable temperature of the radiator as about 1600°C; hence, SiC should be suitable, at least for the immediate future of this technology. We shall make similar comments on the selective radiators discussed in the next part of this section.

In recent years, most of the funding from military sources has been on components expected to be useful on broad-band systems. This is because the temperature of the radiator for the particular military application is expected to be limited to about 1300 K and, as discussed earlier, it is most unlikely that a selective radiator could be used for such a low temperature. As was shown in Fig. 1, the proportion of radiant energy from a radiator at a temperature of 1300 K that could be converted by a silicon solar cell is very small. At higher radiator temperatures, however, it seems quite possible that the selective-radiator approach could find its place, provided that the radiators can be made sufficiently efficient. Consequently, it is quite likely that both broad-band and selective radiators could find their niche in TPV systems, with the distinction possibly being the radiator temperature.

2.2. Selective radiators

Nelson is generally regarded as one of the progenitors of the selective-radiator technology and provided an excellent introduction to the topic in the first NREL conference on TPV [27]. The subject is much less familiar to most researchers than blackbody radiation, and a background explanation of the properties of selective radiators is given in this section. The rare-earth oxides radiate in a relatively narrow band of wavelengths, the peak and range of which are determined by their electronic structure. The lanthanide oxides (the chemical series starting with cerium and ending with lutetium) behave in this manner because the f-electrons that determine their optical properties are not able to interact with other ions. Therefore, they do not form energy bands, and their absorption and emission spectra are more like those of ions in a gas than in a solid. It has been claimed that their off-band emissivity is low, whereas their in-band emissivity approaches unity. They also have the advantage of being, in the main, refractory materials with melting points of 2500–2800 K.

The ideal system would be based on a selective radiator with an emission band occurring at a slightly larger energy than that of the band-edge of the semiconductor converter. Provided that the shortwave and longwave radiation received by the semiconductor converter is minimal, then the only wavelengths absorbed would correspond to the near-band-edge region of the semiconductor. Very efficient conversion would occur, provided that the selective radiator behaved in the nearly ideal manner described. Ytterbia and erbia emit in wavelengths that correspond to the bandgaps of silicon and germanium,[3] respectively. A high-temperature ytterbia radiator, at a temperature of about 2000 K, operating in conjunction with a silicon solar cell, should function very efficiently. However, as Fig. 1 indicates, the power-density output would still be relatively small for such a high radiator temperature. The attraction of this system is that low-cost, high-efficiency cells are, in principle, already available. An erbia selective radiator could operate effectively at a lower temperature in conjunction with a lower-bandgap semiconductor converter. Germanium is unlikely to be useful as a converter, because of its large electron mass, which leads to a reduced voltage.[4] On the other hand, several compounds and alloys from the III–V family of semiconductors do appear to have great promise.

Unfortunately, the rare-earth oxide radiators do not behave in the ideal manner described, and there is always significant off-band emissivity. For wavelengths greater than 3–4 μm, the emissivity of these materials rises rapidly toward unity (because of lattice vibrations) and, if an efficient system is to be constructed, the long-wavelength photons must be reflected back to the radiator to conserve energy and maximize system efficiency. In the short-wavelength range, the higher-energy photons are absorbed by the cell and generate excess minority charge, but the photons have more energy than needed to do this. The excess energy is dissipated as heat in the cells. Ideally, therefore, a means of returning both the longer- and shorter-wavelength photons to the selective radiator is required. This may be achieved in a variety of ways that have been discussed at the three conferences on thermophotovoltaics organized by NREL [5], and some of these options are discussed in Section 4.

2.2.1. Physical principles of selective radiators

The unusual properties of the rare-earth oxides are due to their electron configuration and the order in which the orbitals and shells are filled with electrons. To understand this, it is necessary to appreciate the assignment of quantum numbers in the periodic table. As with the blackbody radiators, the forthcoming material is essentially revisionary. Most papers in TPV that refer to the properties of rare-earth oxides deal with them at a rather superficial level, and there may appear to be a lack of clarity. We shall now discuss elementary concepts in quantum mechanics and the properties of the lanthanides.

From the early developments of quantum mechanics, it was realized that electrons around the nucleus had to be described very specifically and that they are not free to assume arbitrary values of momentum. Four quantum numbers are needed to describe the momentum of a specific electron uniquely. The principal quantum number of an electron is given the symbol n, and this gives the number of the orbit, as was originally

---

[3] Silicon and germanium have bandgaps of approximately 1.16 and 0.66 eV (300 K), respectively. GaSb has a bandgap of about 0.7 eV, similar to that of $In_{0.53}Ga_{0.47}As$.

[4] A large effective mass leads to a large density of intrinsic carriers, which causes a large reverse saturation current density and, consequently, a reduced open-circuit voltage.

hypothesized by Bohr.[5] The azimuthal quantum number describes the angular momentum of the electron and has the symbol l. The magnetic quantum number gives the way in which the electron behaves in a magnetic field and has the symbol m_l. All electrons have a spin of $\pm 1/2$, the spin being given the symbol m_s. No two electrons in an atom can have precisely the same set of quantum numbers (as required by the Pauli exclusion principle), and a given set of four numbers completely defines the momentum of a particular electron. n can have any positive integer value of unity or greater, although the maximum is seven in the periodic table. l can have any integer value from zero to $n-1$. If $n = 3$, for example, l may assume values of 0, 1, or 2. If $n = 4$, l may be 0, 1, 2, or 3. m_l can take integral values, including zero, between $-(l-1)$ to $+(l-1)$. In other words, the number of distinct angular momentum states is simply $(2l+1)$. For each of these, the spin may be $\pm 1/2$. Hence, the total number of states for a given value of l (i.e., a given shell) is $2(2l+1)$. If l has the value zero (defined by the symbol s), then there are only two states allowed. Values of $l = 1$, 2, or 3 are described by the symbols p, d, and f, respectively. The maximum number of electrons for successive values of the principal quantum number is 2, 6, 10, and 14 for $n = 1$, 2, 3, and 4, respectively.

Once a given shell has filled, it is necessary for additional electrons to occupy higher momentum shells or (and) a state with a higher principal quantum number. Thus, for $n = 1$, only s ($l = 0$) electrons are permitted, and there may be two of them. Hydrogen is described as $1s^1$, and He is described as $1s^2$. Strict sequential filling of the orbitals and shells is not a required selection rule, which is a statement that has consequences for the elements of higher atomic number.

The lanthanides occur in the long series in the periodic table between xenon and radon, and their physical properties are dominated by their 4f electrons. There are many Websites that deal in detail with their properties e.g., the rare earths include scandium [21], yttrium [39], and the lanthanides [58–71]. Yttrium is often included in the rare-earths because it is commonly found in the same ores as the lanthanides. The lanthanides are usually defined as the elements from cerium [58] to lutetium [71], and it is in these that we find the materials of interest to TPV. Lanthanum occurs immediately before cerium, but is sometimes not included in the series. As with some of the lower-order series, outer shells are filled earlier than some of the inner shells. In the case of the lanthanides, the $4s^2$, $4p^6$, $4d^{10}$, as well as the $5s^2$ and $5p^6$ electrons are all within the [Xe] core. These are essentially not involved in the behavior of the lanthanides. The main characteristic of importance to us is that the 4f shell fills before the 5d shell

---

[5] Bohr's hypothesis stated that an electron may only have specific values of momentum given by: $mvr = nh/2\Omega$, with m being the mass of the electron, v its velocity, r the distance of its orbit from the nucleus, h is Planck's constant, and n is an integer. The value of n determines the orbits and velocities that the electron can have. When this relationship is coupled with the balance between the centripetal and electrostatic forces, Bohr's formula ultimately results. The additions of the azimuthal quantum number, l, removes the constraint that the orbits must be circular and allows them to be elliptical. The angular momentum is $lh/2\Omega$, the total momentum being given by the sum of the linear and angular momenta. It is important not to adhere to the Bohr model of the atom too rigidly. There are many examples of its inability to explain observations. The ideal approach is to use wave mechanics, in which the locations of the electrons are described probabilistically, rather than by analogy with planets around a sun.

because, for atomic numbers of about 60 and greater, the energy of the former [4f] is less than that of the latter [5d].

The complete lanthanide series is shown in Table 1. All the elements have a characteristic valence of three, although [28–30] some have other possibilities. The valence is governed by the $6s^2$ electrons, in addition to which the $5d^1$ and either one or two of the 4f electrons can contribute. Both Ce and Pr can lose one or two 4f electrons, as can Tb. All of these can have valence three or four. Sm, Eu, and possibly Yb can lose either zero or one 4f electron (in addition to the 6s electrons) to have valence two or three. Although, the valence of all the lanthanide oxides is usually shown as three, examination of the catalogues of suppliers shown that much more complicated compositions are more usual.

The chemical properties of the lanthanides depend on their valence electrons, which are mainly from the 6s and 5d orbitals, although, with some of the elements, either one or two 4f electrons may participate. When any of the lanthanides react (say with oxygen), their valence electrons are lost in the formation of the oxide. The 4f electrons are, in the main, left behind. There is a strong attractive force between the nucleus and the 4f electrons, and the distance of these from the nucleus is very small. They are therefore very strongly localized with wave functions that have very limited spatial extent. Hence, they are unable to interact with other ions, and energy bands are unable to form.

The optical properties of the lanthanide oxides are thus more like those of gaseous materials because of the localization of their 4f electrons. When the material is heated, the emitted spectra consist of relatively sharp lines in a limited portion of the spectrum, rather than being like a blackbody spectrum. This property was first exploited by Baron von Welsbach [31] in the Coleman-type lantern. In his design, the material

Table 1
The Lanthanide Series

Element	Atomic number	Electronic configuration	Valence
Lanthanum	57	$[Xe]5d^1 6s^2$	3
Cerium	58	$[Xe]4f^1 5d^1 6s^2$	3 or 4
Praesodymium	59	$[Xe]4f^3 6s^2$	3 or 4
Neodymium	60	$[Xe]4f^4 6s^2$	3
Promethium	61	$[Xe]4f^5 6s^2$	3
Samarium	62	$[Xe]4f^6 6s^2$	2 or 3
Europium	63	$[Xe]4f^7 6s^2$	2 or 3
Gadolinium	64	$[Xe]4f^7 5d^1 6s^2$	3
Terbium	65	$[Xe]4f^9 6s^2$	3 or 4
Dysprosium	66	$[Xe]4f^{10} 6s^2$	3
Holmium	67	$[Xe]4f^{11} 6s^2$	3
Erbium	68	$[Xe]4f^{12} 6s^2$	3
Thulium	69	$[Xe]4f^{13} 6s^2$	(2?) or 3
Ytterbium	70	$[Xe]4f^{14} 6s^2$	2 or 3
Lutetium	71	$[Xe]4f^{14} 5d^1 6s^2$	3

consisted of thoria mixed with a precise amount of ceria (the rare-earth component). When heated, this material could be made to radiate in the central portion of the visible spectrum by adding the proper amount of ceria.

Other materials behave in a similar, although not identical, fashion. For example, if we examine the two series beginning with scandium [21] and yttrium [39], we see that there is similar behavior with the 3d (for scandium) and 4d (for yttrium) sub-shells filling after the 4s and 5s sub-shells are already filled. However, the d-electrons are not nearly as highly localized as the f-electrons that govern the properties of the lanthanides. The very narrow bands that form in the latter case are much wider in the case of the d-electron materials because they are able to make many other transitions. Consequently, the bands are much broader, i.e., the selectivity is less than that of the lanthanides.

Ferguson et al. [32] investigated the properties of cobalt-doped $MgAl_2O_4$, which is an important material in this context because its electronic structure is [Ar] $3d^7$ $4s^2$. The properties of Co are thus dominated by the seven 3d electrons when the two 4s valence electrons have been removed in the reaction with oxygen. The $MgAl_2O_4$ is simply a dielectric host material for the cobalt. The emission band corresponds well to the region of spectral response of gallium antimonide (GaSb). At the time of writing, this combination forms the basis of the only TPV system nearing the point of being a commercial product. The attraction of this approach is that the power radiated is much more than that radiated by the highly selective rare-earth oxides. More will be said of this in Section 7.

Sometimes, the selective radiator (the rare-earth oxide) is incorporated in a host material, usually a dielectric, and unless the combination is well-designed, the radiative properties of the host can dominate the combination. Parent et al. [33] realized that the background radiation, which is usually blackbody (or graybody) in nature, could be suppressed by making the thickness of the material less than its optical absorption depth. The absorption depth is typically about 5–10 μm. It follows that there is also very little emission from materials less than this thickness. For very thin films, the selective-radiator properties are excessively suppressed (which is the same thing as saying that the sample is too thin to absorb or emit at any wavelength). For greater thicknesses, the background radiation increases and internal scattering becomes excessive.

2.2.2. Practical rare-earth oxide radiators

Nelson [34] solved the problem of producing very thin radiators by making bundles of fibers of a fabric soaked with a solution of the rare-earth salt of interest. Thin-film approaches have also been attempted and will be discussed later. Most work was done on fibers of Yb_2O_3, but Er_2O_3 and Ho_2O_3 were also used. The fiber was dried and then heated to high temperature to remove the fabric and to oxidize the rare-earth metal. The remaining structure consisted only of rare-earth oxide fibers. The fibers were supported by a ceramic substrate, and they were inserted in bundles into holes in the latter. The fuel passed through the holes from the rear of the substrate and burned just below the tip of the fibers, rather than near the substrate. This minimized the background blackbody radiation from the substrate. A schematic of the substrate and fiber bundle structure is shown in Fig. 3.

Nelson [35] obtained data on the magnitude of the radiated power density from the Yb_2O_3 fibers that could be converted by a silicon solar cell. This was measured as a function of the radiator temperature, the ratio of fuel to air, and the fuel pre-heat temperature. Figure 4 shows the variation of the optical output as a function of the fuel loading in W cm^{-2}. Alongside each point in the figure is a number giving the fuel/air ratio. This set of data was obtained without fuel pre-heating. The main point to note is the relatively low efficiency of the fuel-to-photon conversion process. Only a few W of optical power are available for conversion, and the converter efficiency of the latter process is likely to be less than 20–30% of photons to electricity. However, the potential power-density output of the actual system is on the order of 1 W cm^{-2}. The project for which this converter was designed was for stand-alone gas boilers. In these, the fans and blowers could continue to operate even in the event of a power failure. Chubb et al. [36] investigated thin-film-based radiators because it is straightforward to reduce the characteristic dimension (i.e., the reciprocal of the absorption coefficient) to the appropriate range.

It is important to be able to calculate the efficiency of the thin-film rare-earth-oxide radiators and also to calculate its radiated power density for a specific temperature. Chubb et al. [36] tackled this problem by splitting the entire radiated spectrum into

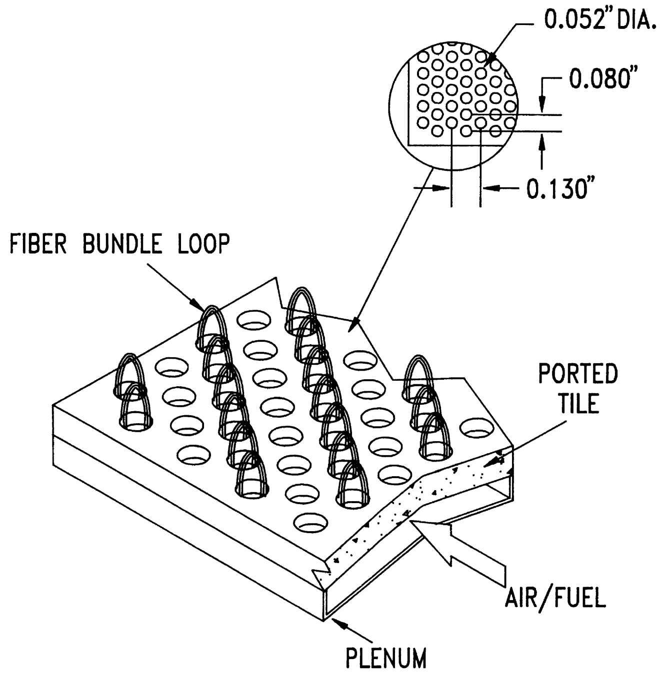

Fig. 3. Selective radiator based on fiber bundles of ytterbia. Reproduced by permission of the American Institute of Physics, and the author(s) [34].

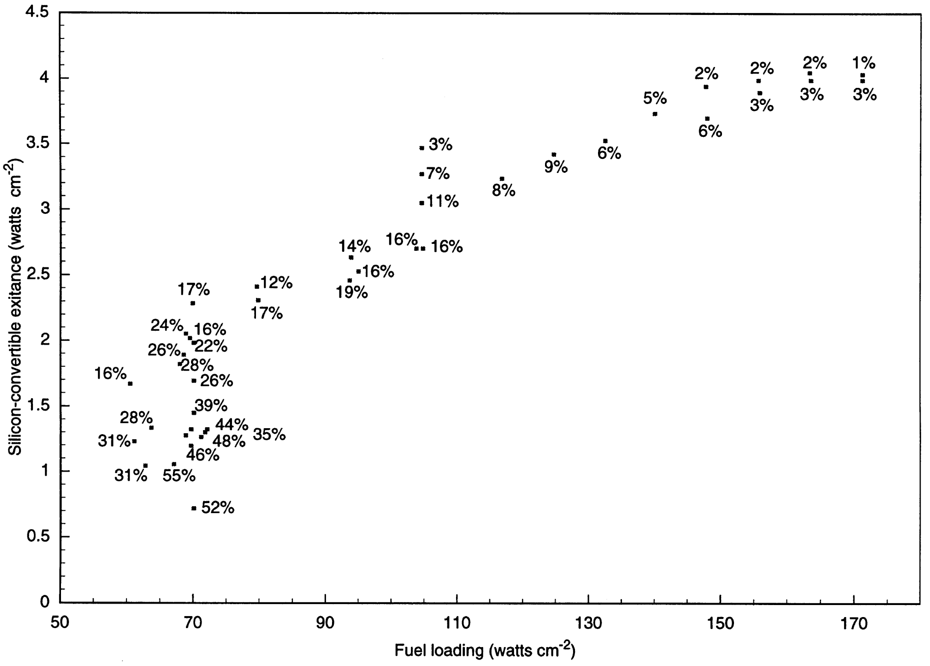

Fig. 4. Variation of the quantity of radiation convertible by silicon cells with the fuel loading. The numbers in the diagram indicate the richness of the fuel/air mixture. Reproduced by permission of the American Institute of Physics, and the author(s) [34].

three wavelength ranges: below-band (described by a constant extinction coefficient); within-band (where the extinction coefficient is a function of wavelength); and above-band-gap radiation (described by a constant extinction coefficient). It was also assumed that there could be a thermal gradient across the thickness of the film. The analysis was extremely mathematical; as in other section, we shall forego the mathematical detail and concentrate on the approach and the results. The model was used to predict the emissivity and power density radiated by the thin-film radiators; data for erbium in a host of yttrium aluminum garnet are shown in Figs 5(a) and 5(b).

The emissivity was integrated across the entire spectrum considered, and various radiator temperatures were considered. As can be seen, the emissivities are certainly not near unity, and the power densities are, as with Nelson's data, several W cm^{-2}. Chubb et al. [36] were interested in TPV as a means of providing power for space vehicles on missions very distant from the sun (e.g., the Pluto fly-by), with the source of heat being radioactivity. Consequently, relatively low radiator temperatures ($\sim$1200 K) are likely. For such a low temperature, the radiated power densities are rather low. Also, it must be noted that these are theoretical results, and practical experience with selective radiators is less convincing. Much more work is required on this aspect of TPV technology before it can be reduced to practice. Most published data show normalized results with no indication of the actual magnitudes involved.

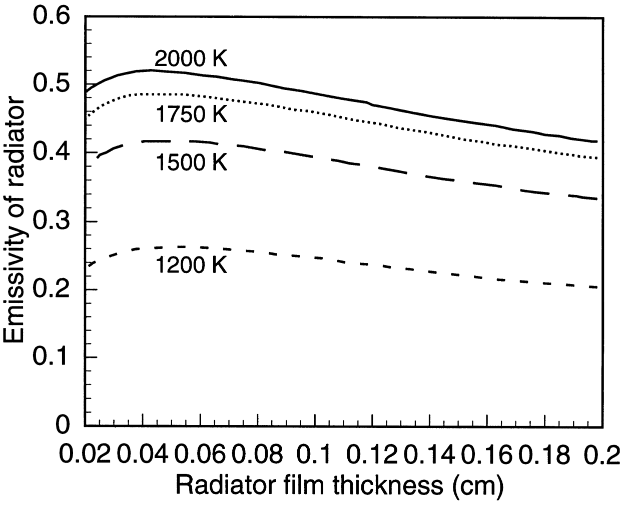

Fig. 5a. Variation of the emissivity of a thin-film of erbium/YAG with the film thickness, with the radiator temperature being treated parametrically. Reproduced by permission of the American Institute of Physics, and the author(s) [36].

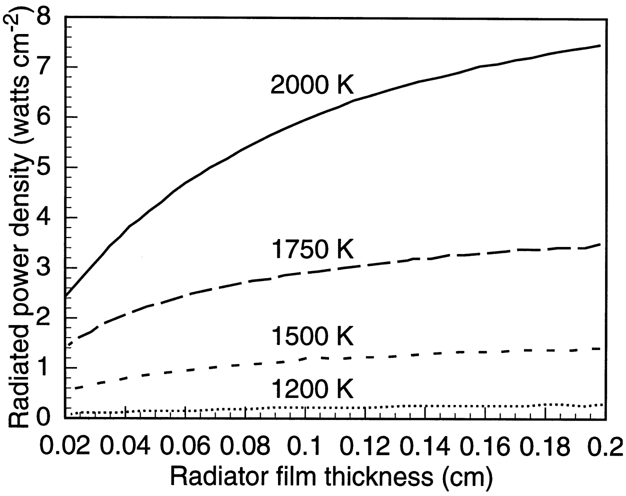

Fig. 5b. Variation of the radiated power density of a thin-film of erbium/YAG with the film thickness, with the radiator temperature being treated parametrically. Reproduced by permission of the American Institute of Physics, and the author(s) [36].

2.3. Summary

In this section, we have reviewed elementary models of blackbody radiation and explained the highly selective radiative properties of the rare-earth oxides. The spectral power-density in the former case is used later to calculate the performance of converters. The broad-band approach is the primary option for radiators in the lower temperature range, assuming that the alternative is to use silicon cells with selective radiators. However, narrow-bandgap semiconductors used with selective radiators have been discussed by Wilt et al. [37], in which case both approaches could be viable. None of the radiator materials is likely to be limited by problems of stability, and the rare-earth materials are certainly likely to be more stable even when higher temperatures are used. It is not likely, however, that such temperatures ($\sim 2000^{\circ}$C) will be used in practical systems in the immediate future. Finally, it should be pointed out that the only system at even the prototype stage is based on $MgAl_2O_4$ (a selective, but relatively broad-band, radiator) coupled with a narrow-bandgap semiconductor (GaSb).

Systems based on germanium and silicon have not, thus far, realized their potential cost advantages, and it is probably true to say that the re-emergence of interest in TPV technology arises from the current availability of high-quality, low-bandgap semiconductor converters from the III–V family of compounds and alloys. Also, there are several other approaches for fabricating selective radiators. Only two have been discussed here, but the Third NREL TPV conference proceedings contain other [38, 39, 13] approaches. Each of these has significant advantages, including such features as durability, low cost, ease of fabrication, and mechanical robustness. The proceedings of the earlier NREL TPV conferences also contain interesting approaches. This aspect of TPV is still very much in its infancy, one reason being the prior lack of high quality semiconductor converters that have only become available in the last few years. If TPV does succeed in becoming a large-volume business, then more attention will undoubtedly be paid to this important aspect of the technology.

3. Modeling, fabrication, and characterization of TPV converters

3.1. Modeling of TPV semiconductor converters

A complete TPV system consists of five discrete components, possibly the most complicated of which is the semiconductor converter. The efficiency of the other components, however, is just as important to the overall efficiency of the complete system. The approach taken here is to consider only the semiconductor converter, because this reflects the author's own experience and the fact that the efficiencies of the other components are much more difficult to quantify. In a later section, we shall discuss modeling of systems. For example, it is straightforward to calculate the heat liberated by burning a unit mass of a given fuel, but it is much more difficult to take into account the details of system design when trying to calculate how much of that chemical energy is converted into photons by the radiator. Clearly, the surface temperature of the radiator must be less than that of the combustion gases, but the situation is more complicated than this. There are also likely to be strong effects due to nonuniformities in the radiated distribution of photons caused by variations in surface temperature, in turn caused by the specific design.

The performance of the filter (assuming one is used) is also a rather vague quantity, unless the back-surface reflector technique described in Section 4 is used. This approach is relatively free of wavelength dependence, although other filters are not so simple. There are variations in the optical properties of some of the filters because of the strong angular dependence of the incident radiation and the vagaries in actual vs designed properties (e.g., thickness of thin-film layers). In fact, if a complete system is to be modeled, then the most sensible approach probably uses Monte-Carlo methods, as discussed by Gethers et al. [40] at the Third NREL TPV conference.

Finally, the radiated flux depends sensitively on the nature of the radiator. If one is considering a selective radiator, then the presence of off-band radiation must be accounted for. As mentioned earlier, because of lattice vibrations, it is inevitable that the emissivity increases at wavelengths longer than about 3–4 μm. Therefore, unless the relevant proportions of useful and useless radiation are known, it is impossible to perform accurate modeling. As Chubb et al. [41] have pointed out, there are also complicating effects due to internal scattering and the thickness of the radiator. Blackbody radiators are, perhaps, simpler to treat analytically, but they are still subject to uncertainties. Some of the issues mentioned above still apply; furthermore, emissivities of these radiators are, in general, not known in detail as a function of wavelength (in other words, they are not necessarily true blackbodies) and there are several other influences.

For all these reasons, we shall consider only the converter in this section. It is probably true to say that the converter is still the most important component of the TPV system. Even with these restrictions, the methods are severely limited and merely help to establish an upper limit on the performance and to assist in accounting for likely losses.

With all these negative-sounding comments in mind, it is as well to state our assumptions at the outset. We are considering a highly idealized converter, with zero parasitic losses, perfect photon recirculation (see details in Section 4), nearly ideal quantum efficiency, no heating of the device, and perfect junction characteristics. Despite these unrealistic assumptions, the modeling procedures indicate the most useful range of bandgaps for the semiconductors and, therefore, the typical materials that may be considered. All modeling is only as useful as the input parameters are accurate, and with most TPV materials, the solid-state electrical and optical parameters are unknown. Of the funding available to date, very little has been devoted to characterization, which ultimately spells disaster! Nevertheless, a start must be made, and we need to know the type of semiconductor that can be seriously considered to enable systems to be made.

The approaches reviewed in this section were developed by Cody et al. [42] who considered devices limited only by radiative recombination (i.e., the principle of detailed balance, originally developed by van Roosbroeck et al. [43]; by Shockley et al. [44], by Gray et al. [45], who took an approach based on treating the converters as endoreversible heat-engines; and by Wanlass et al. [46], who used an empirical approach based on how the reverse saturation current behaves as a function of bandgap. As will be seen, the conclusions differ significantly.

3.2. *Radiative recombination* [44, 43]

The principle of detailed balance was applied to the interaction of photons with creation of electron-hole pairs. To maintain equilibrium, the recombination rate (expressed in $\mathrm{cm}^{-3}\ \mathrm{s}^{-1}$) of the excess charge must also be equal to the incident flux. This analysis led to an expression for the excess carrier lifetime, as limited only by radiative recombination. If other recombination processes are significant, such as recombination via defects, Auger recombination, and free-carrier absorption, then the lifetime is necessarily reduced. Hence, the value of the lifetime calculated from radiative recombination is an upper limit, and it provides a means of calculating the upper limit on the efficiency of *p–n* photovoltaic converters. The rate of recombination was given in the original paper by van Roosbroeck et al. [43]:

$$\Re = 32\pi^2 c\left(\frac{kT_{\mathrm{emit}}}{ch}\right)^4 \int_0^\infty \frac{n^2 \kappa u^3}{e^u - 1}\,\mathrm{d}u \quad (\mathrm{cm}^{-3}\ \mathrm{s}^{-1}). \tag{3}$$

In this formula, c is the speed of light, k is Boltzmann's constant, h is Planck's constant, T_{emit} is the temperature of the radiator, n is the refractive index of the semiconductor, k is the extinction coefficient of the semiconductor, and u is a dummy variable given by:

$$u = \frac{eE}{kT_{\mathrm{emit}}}. \tag{4}$$

Thus, van Roosbroeck et al. [43] were able to calculate the recombination rate for germanium using measurements of the refractive index and the extinction coefficient, and performing the integration numerically. In a later paper, Shockley et al. [44] calculated the upper limit on the efficiency of a silicon cell and made a number of interesting philosophical points. Among these was (interpretation of the present author) that it is vital to know the upper limit of the efficiency of any electronic device so that one knows how much further the device can be developed before the extra effort becomes questionable. The analogy was drawn with heat engines and the Carnot efficiency. The latter cannot be achieved due to losses such as friction and inefficient heat exchangers, but it tells the engineer how much further the system could, in principle, be developed. In the case of solar cells, the equivalent of friction is the series resistance and the reflectance losses. Hence, they derived the maximum efficiency of a *p–n* junction photovoltaic converter as:

$$\eta = \left[x_{\mathrm{g}} \int_{x_{\mathrm{g}}}^{\infty} x^2/(e^x - 1)\,\mathrm{d}x\right] \Big/ \int_0^\infty x^3/(e^x - 1)\,\mathrm{d}x, \tag{5}$$

in which:

$$x_{\mathrm{g}} = \frac{eE_{\mathrm{g}}}{kT_{\mathrm{emit}}}, \tag{6}$$

where E_{g} is the energy gap of the semiconductor. The efficiency was plotted against the normalized variable u, and this showed for a solar cell that the maximum efficiency, as limited only by radiative recombination, was about 44%, as is shown in Fig. 6. The model assumes that the converter was placed at the center of a spherical enclosure and that it was held at a temperature of 0 K. The lower x-axis is the bandgap of the converter normalized by the thermal energy of the radiator. The upper x-axis is the bandgap of the converter for a radiator temperature of 1500 K. With more realistic limitations, including that of the cell having a finite temperature, the potential is inevitably less than this.

Nevertheless, the assumption that the semiconductor is in equilibrium with the incident photon flux shows that the prospects for improving the efficiency were much better than originally predicted by earlier semi-empirical papers by, for example, Prince [47], Loferski [48], and Wolf [49]. As is now known, the efficiency of modern silicon solar cells, at least in the laboratory, exceeds that of the original semi-empirical predictions. This is the essential point made by Cody et al. [42] in the context of TPV conversion. Although several interesting applications exist for TPV generation of electricity, many more would emerge if the improvement in this technology were comparable with that of solar cells. For example, if it were possible to approach 70–80% of the efficiency predicted by the radiative recombination limit, then TPV generators would greatly interest automobile manufacturers and oil producers, which are markets of enormous volume. It may well be that with a sustained, well-funded program, the efficiencies could approach the same fraction of the theoretical limit as does that of solar cells.

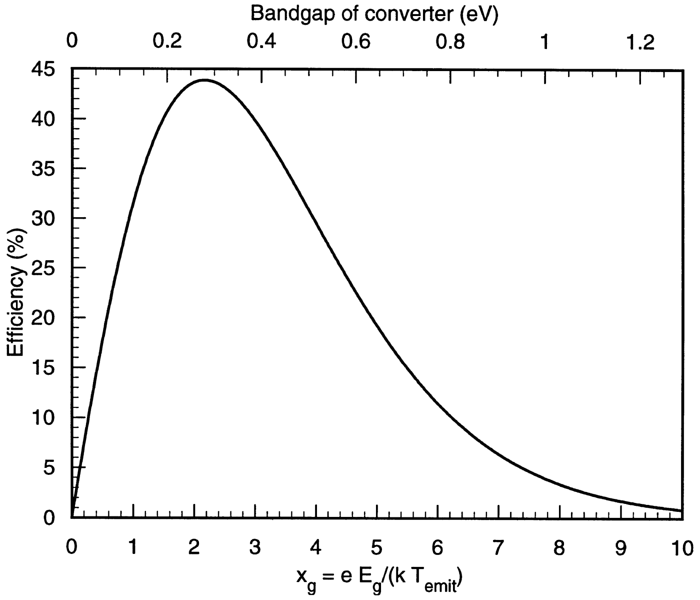

Fig. 6. Modeled variation of the efficiency of a *p*/*n* junction converter. Reproduced by permission of the American Institute of Physics, and the author(s).

3.3. Endoreversible heat-engines

The approach discussed in this section was developed by Gray et al. [45] and a similar approach was used by Cody et al. [50]. De Vos [51] considered solar cells as endoreversible heat-engines and applied his ideas to solar cells. The upper limit on any heat engine is given by the Carnot efficiency, viz:

$$\eta = 1 - \frac{T_{\text{cell}}}{T_{\text{emit}}}. \tag{7}$$

For a TPV device and radiator at temperatures of 300 and 2000 K, respectively, the maximum efficiency is therefore 85%. This would apply to a lossless system. The efficiency of a lossless system is:

$$\eta = \frac{P_{\text{OUT}}}{P_{\text{IN}}}, \tag{8}$$

where P_{IN} is the radiation that is incident on the converter and is not returned to the radiator (this does not imply that it is all convertible). The view-factor in a TPV system is the equivalent of the concentration ratio in solar cell technology, but it must always be less than unity. If we restrict the discussion to an ideal flat-plate geometry, then the view factor, F, is unity. In a cylindrical geometry, it is less than this and depends on the radii of the radiator and the cells. In the present case, we shall consider only the ideal flat-plate case. As mentioned several times already, a fraction of the incident radiation is not convertible by the cell: this can be expressed as:

$$P_{\text{R}} = \int_{E_0}^{E_{\text{L}}} P_{\text{E}}(E)\,\mathrm{d}E + R\int_{E_{\text{L}}}^{E_{\text{H}}} P_{\text{E}}(E)\,\mathrm{d}E + \int_{E_{\text{H}}}^{\infty} P_{\text{E}}(E)\,\mathrm{d}E \tag{9}$$

P_{E} is the power density emitted by the radiator. The first and last terms of eqn (8) represent the radiation that lies outside a band-pass filter defined by the energies E_{L} and E_{H}. The second term represents that part of the useful energy that should have passed to the TPV converter but is somehow reflected back to the radiator (e.g., by grid lines or by the surface of the cell). The input power can therefore be defined as:

$$P_{\text{IN}} = P_{\text{E}} - \beta P_{\text{R}}. \tag{10}$$

The quantity β represents the efficiency with which P_{R} is returned to the radiator, and it allows for absorption in the filter and scattering outside the bounds of the optical cavity.

In the analysis given by De Vos [51] the output power is given by:

$$P_{\text{OUT}} = \frac{2\pi V}{c^2 h^3}\left[(1-R)\int_{E_{\text{L}}}^{E_{\text{H}}} \frac{E^2}{\exp\left(\frac{E}{kT_{\text{emit}}}\right)-1}\,\mathrm{d}E - \frac{1}{F}\int_{E_{\text{g}}}^{\infty} \frac{E^2}{\exp\left(\frac{E-V}{kT_{\text{cell}}}\right)-1}\,\mathrm{d}E\right] \tag{11}$$

V is the applied potential (this can be thought of as the amount by which the potential

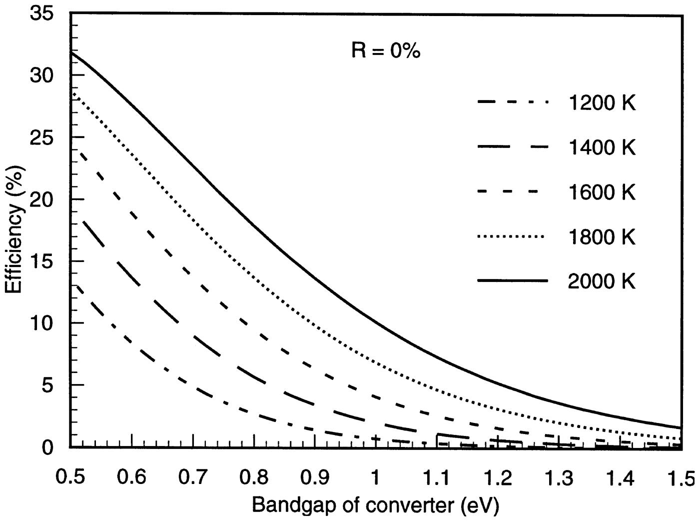

Fig. 7. Modeled variation of efficiency with bandgap of the converter. The radiator temperature is treated parametrically. No sub-bandgap photons are returned to the radiator. Reproduced by permission of the American Institute of Physics.

of the electrons is reduced to extract them to the external circuit). c and h are the speed of light and Planck's constant, respectively. R is the reflectance of useful (meaning convertible) radiation from the cell, and F is the view factor. E_g is the bandgap of the converter, E_L is the lower-pass energy of the filter and E_H is the high-pass energy. T_{emit} and T_{cell} are the temperatures of the radiator and the cell, respectively.

Equation (11) assumes that the radiation from the cell is neglected, as is the incidence of additional radiation from other cells. The last equation may be treated numerically to determine the voltage at the maximum power point and, hence, the maximum output power density. Hence, the efficiency may also be calculated. The value of this approach in the present context is that various types of filters may be considered, including a band-pass (which may be taken as equivalent to a selective radiator) or an edge-filter (able to transmit high-energy photons and to reflect those with energies less than the bandgap of the converter). Although it does not influence the power-density output, the efficiency of the reflecting filter can also be treated parametrically. Figures 7–11 summarize the modeling of efficiencies performed by Gray et al. [45]. In these, view-factor F has been taken as unity, the parasitic reflectance as zero, the cell temperature as 300 K, and the radiator temperature is treated parametrically. The fraction of sub-bandgap photons successfully returned to the radiator is shown inset in the figures. Figure 12 shows the power-density output for the same range of temperatures. This quantity is unaffected by the effectiveness of the sub-bandgap reflectance. Figures 13 and 14 show the efficiency and power-density output, respectively, for a device with a band-pass filter restricting the range of energies reaching it.

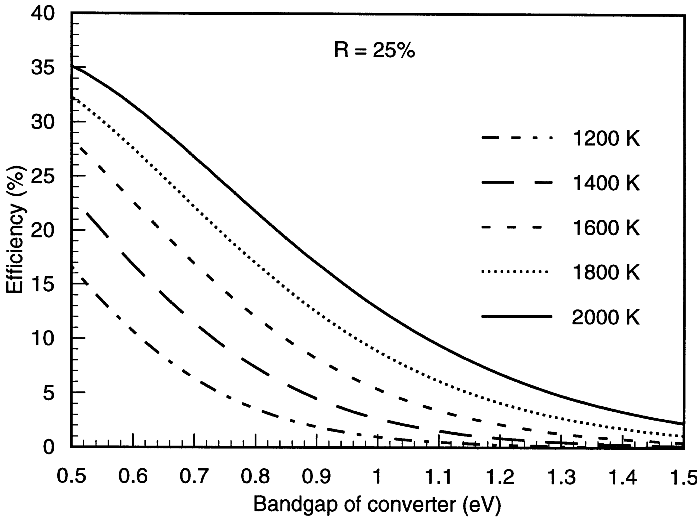

Fig. 8. Variation of efficiency with bandgap of the converter. The radiator temperature is treated parametrically. Twenty-five percent of the sub-bandgap photons are returned to the radiator.

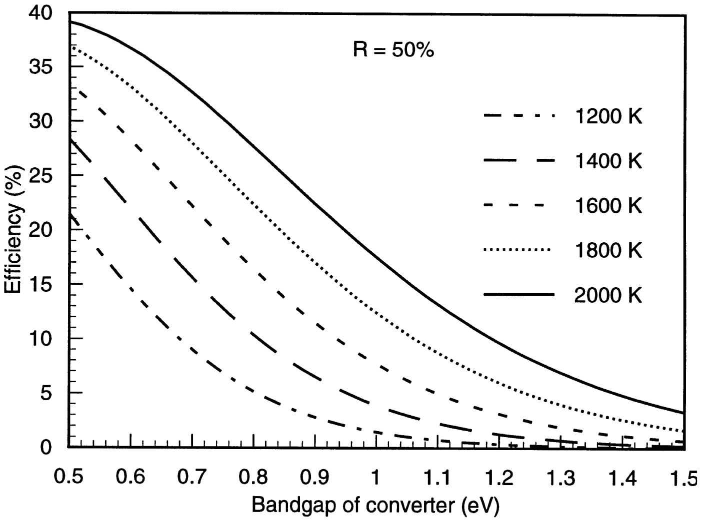

Fig. 9. Variation of efficiency with bandgap of the converter. The radiator temperature is treated parametrically. Fifty percent of the sub-bandgap photons are returned to the radiator.

In Figs 13 and 14, the efficiency of recirculation of sub-bandgap photons is unity. An edge-filter simulates the behavior of a selective radiator. As can be seen, the output is lower, although the efficiency is several percent larger than in the broad-band case.

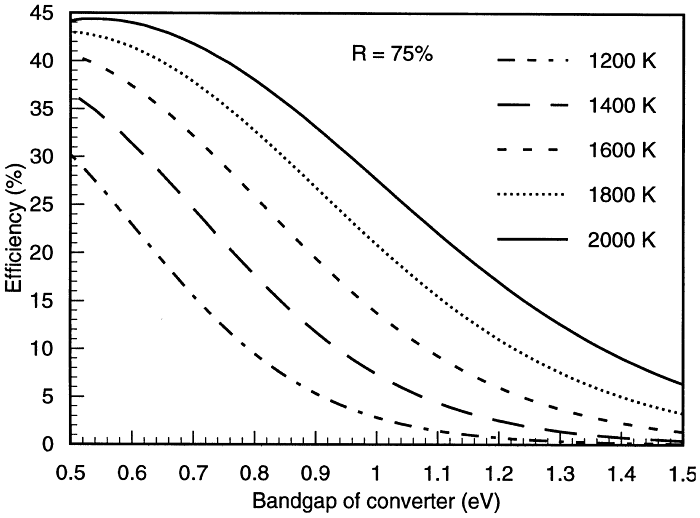

Fig. 10. Variation of efficiency with bandgap of the converter. The radiator temperature is treated parametrically. Seventy-five percent of the sub-bandgap photons are returned to the radiator.

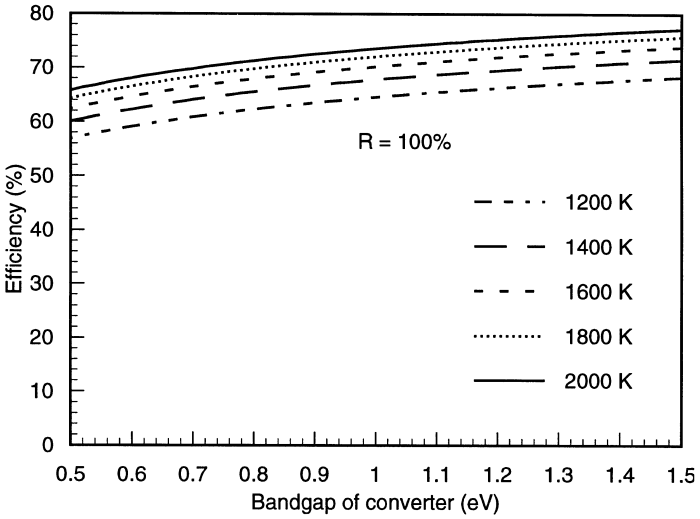

Fig. 11. Variation of efficiency with bandgap of the converter. The radiator temperature is treated parametrically. One hundred percent of the sub-bandgap photons are returned to the radiator.

3.4. Empirical modeling [46]

This approach considered only broad-band radiators. The emissivity was taken as unity and the quantum efficiency of the device as some number less than unity. In the

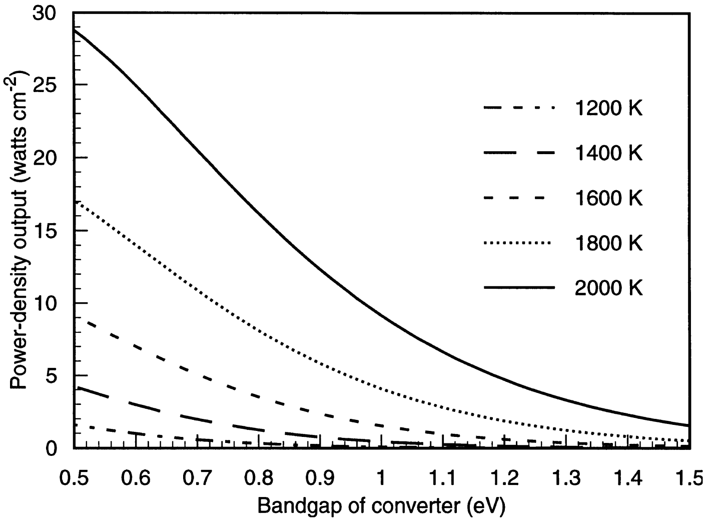

Fig. 12. Power-density output as a function of converter bandgap, with the radiator temperature being treated parametrically. The power output is unaffected by the recirculation efficiency.

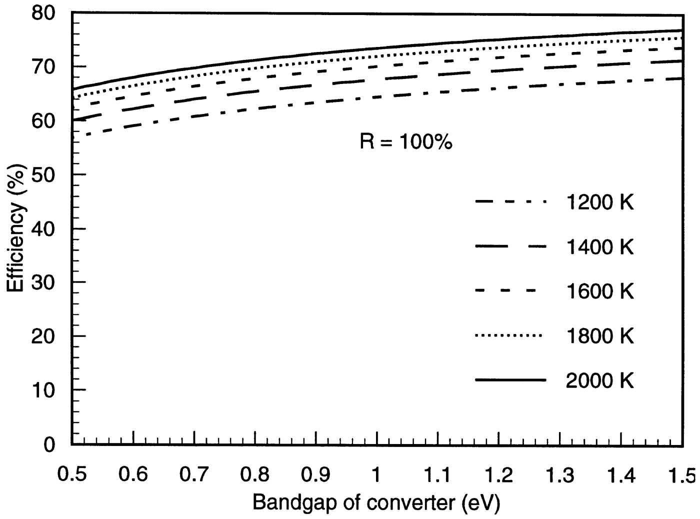

Fig. 13. Variation of efficiency with the bandgap of the converter for a band-pass filter. The incident radiation is limited to the range $E_g < E < E_g + 0.1$ eV. The device temperature was 300 K, the view factor was unity, and the spurious reflectance was zero.

modeling presented here, it is taken as 0.95. Although this is unreasonable across the entire response spectrum of the device, it again provides an upperlimit. For some devices, to be discussed later, external quantum efficiencies are as high as this in limited wavelength ranges.

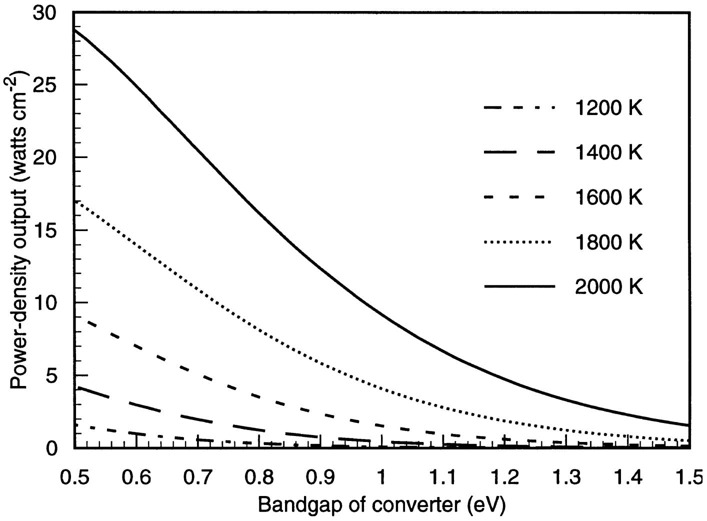

Fig. 14. Variation of power-density output with the bandgap of the converter, for a band-pass filter. The incident radiation is limited to the range $E_g < E < E_g+0.1$ eV. The device temperature was 300 K, the view factor was unity, and the spurious reflectance was zero. The power density is unaffected by the efficiency of the photon recirculation process.

Modeling of TPV converters performed to date has been highly idealized and has typically made a number of assumptions that are practically unrealistic. For example, most modeling has assumed that all sub-bandgap photons can be returned to the radiator, that there are no parasitic losses due to series resistance or optical reflectance, and that there is no heating of the cell beyond perhaps 350 K. More realistic modeling needs to be performed. It has generally been assumed that the short-circuit density can be obtained simply by assuming that every photon with energy greater than that of the bandgap generates an electron/hole pair, which is collected and delivered to the external circuit. Most modeling, and certainly that considered here, has been concerned with broad-band radiators, which are either black or gray. Thus, the short-circuit current density may be expressed as:

$$J_{sc} = e \sum_{E=E_g}^{\infty} Q(T_{cell}, E)F(T_{emit}, E) \tag{12}$$

where $Q(T_{cell}, E)$ is the quantum efficiency as a function of the temperature of the cell and the photon energy, and where $F(T_{emit}, E)$ is the photon flux as a function of the radiator temperature and the photon energy, given by:

$$F(T_{emit}, E) = \left(\frac{2\pi e^3}{h^3 c^2}\right) E^2 \left[\exp\left(\frac{eE}{kT_{emit}}\right) - 1\right]^{-1}. \tag{13}$$

The reverse saturation current density has been obtained using an approximation originally devised by Fan et al. [52] and subsequently used by Nell et al. [53] to model the performance of GaAs solar cells, and by Wanlass et al. [46], who fitted the values of J_0 for a wide range of semiconductors to the empirical equation discussed below. Having obtained the short-circuit current density and the reverse saturation current density, it is then possible to obtain the open-circuit voltage. The empirical equation for the reverse saturation current density is:

$$J_0 = \beta(E_g)T_{\text{cell}}^3 \exp\left(-\frac{E_g}{kT_{\text{cell}}}\right), \tag{14}$$

in which the fitting parameter $\beta(E_g)$ was shown [46] to be given by:

$$\beta(E_g) = 3.165 \times 10^{-4} \exp(2.912E_g). \tag{15}$$

The open-circuit voltage of the cell is given by the well-known expression that results from the diode equation as:

$$V_{\text{oc}} = \frac{nkT_{\text{cell}}}{e} \ln\left(\frac{J_{\text{sc}}}{J_0}\right), \tag{16}$$

where n is the ideality factor of the cell, J_{sc} is the short-circuit density of the cell, J_0 is the reverse saturation current density.

The fill factor of the cell was calculated using an approximation originally devised by Green [54] that appears to be accurate to within one percent, down to bandgaps of approximately 0.3 eV. Consequently, the modeling has made successful use of this because the semiconductors involved all have bandgaps greater than 0.3 eV. This has also been tested by numerical differentiation of the curve of power vs voltage. The empirical expression for the fill factor is:

$$FF = \frac{v_{\text{oc}} - \ln(v_{\text{oc}} + 0.72)}{v_{\text{oc}} + 1}, \tag{17}$$

with:

$$v_{\text{oc}} = \left(\frac{eV_{\text{oc}}}{kT_{\text{cell}}}\right). \tag{18}$$

Thus, with expressions for the short-circuit current density, the open-circuit voltage, and the fill factor, it is straightforward to obtain the efficiency and the maximum power-density output.

Figure 15 shows the log of the reverse saturation current density and the short-circuit current density as functions of bandgap, with the radiator temperature being treated parametrically. Radiator temperatures in the range of 1200–2000 K are considered in the model and, as can be seen, the current densities are very high. For a radiator temperature of 1500 K, the theoretical value approaches 20 amps cm^{-2} for a bandgap of 0.5 eV.

Figure 16 shows the variation of the fill factor and the open-circuit voltage with converter bandgap, the radiator temperature being treated parametrically. As indicated, these are devices of relatively low voltage, although the fill factors still approach

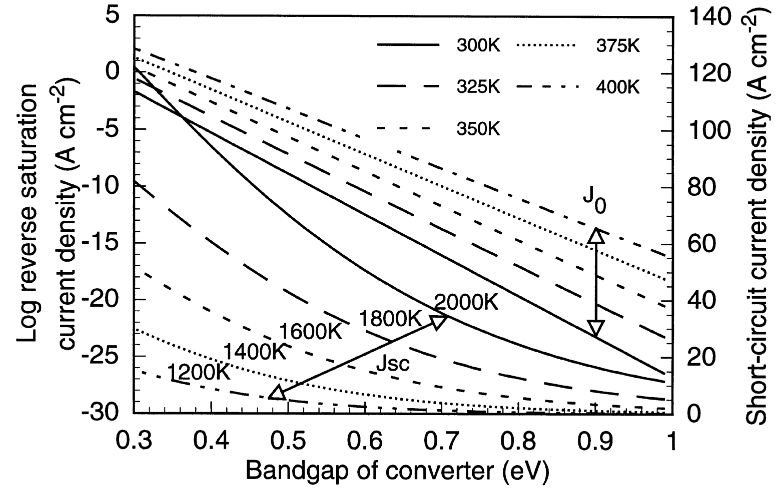

Fig. 15. Variation of the logarithm of the reverse saturation current density and the short-circuit current density as functions of converter bandgap. The converter temperature is treated parametrically in the former case, and the radiator temperature is treated parametrically in the latter.

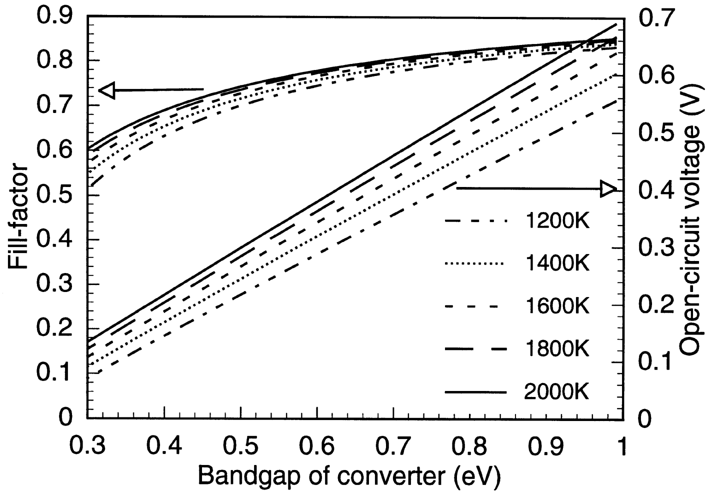

Fig. 16. Variation of fill factor and open-circuit voltage with converter bandgap. The radiator temperature is treated parametrically.

those of solar cells. Finally, Figure 17 shows the efficiency and power-density output as functions of converter bandgap, with the radiator temperature again being treated parametrically. This model assumes that all sub-bandgap photons are returned to the radiator. Although this does not influence the power-density output, it makes a large difference to the system efficiency and makes the point that a means of photon

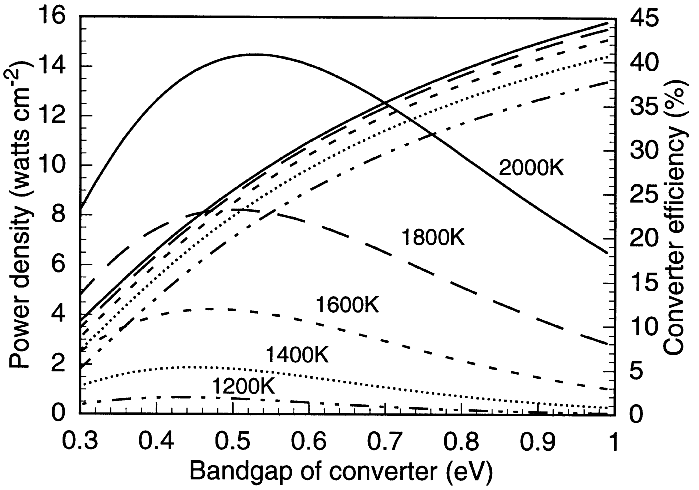

Fig. 17. Variation of the converter efficiency and the power-density output as a function of the converter bandgap. The radiator temperature is treated parametrically, and 100%-efficient recirculation of sub-bandgap photons is assumed.

recirculation is essential in broad-band-based systems. It is the photon recirculation that causes the power-density output to pass through a maximum. Without it, the efficiency would do so, but the peak would only be about 8–10% for a radiator temperature of 1500 K.

For the intermediate range of 1600 K, power-density outputs of almost 6 W cm^{-2} are predicted. If one assumes that this is a factor of 2–3 times too optimistic, then we would speculate that outputs of 2–3 W cm^{-2} seem possible. These calculations assume that the converter temperature is 300 K. The bandgap at which the power density reaches its maximum is relatively independent of radiator temperature and lies between 0.45–0.55 eV. If the converter temperature is assumed to rise to perhaps 350 K, then the optimum bandgap also increases somewhat, but not by more than 0.05 eV. If series resistance is also taken into account, there is also a significant increase in the optimum bandgap. The ideal bandgap predicted on the basis of the semi-empirical model is thus significantly higher than that predicted by Cody and by Gray, using the more idealized model based on the principle of detailed balance.

3.5. Summary of the two modeling approaches

In the empirical approach, experience of a wide range of semiconductors is used to estimate the reverse saturation current density, without attempting to assign the mechanism responsible. The short-circuit current density is then calculated from the nature of the irradiation. With these two currents, and an approximation to the fill factor, the efficiency and the power-density output of the converter are calculated. In Cody's model, no effort was made to account for the effects of photon recirculation, although this was remedied by Gray et al. [45]. Nothing is said of reverse saturation current density in either case. The principle of detailed balance proceeds by gradually reducing the chemical potential of the electrons until the product of their number and potential is maximized. Thus, the efficiency is effectively determined by numerical differentiation of the current/voltage characteristic, without any of the algebraic approximations involved in the empirical model.

The Shockley/Cody/Gray approaches predict a lower value of the optimum bandgap of the converter than does the empirical approach, and they do not take into account régimes in which the methodology fails. For example, in the empirical approach, nothing is said about the nature of the reverse saturation current. It may well be that at low bandgaps, there is an additional contribution from Auger recombination, which could not have been predicted on the basis of experience with wider-bandgap materials. If so, and allowing for the potentially higher device operating temperatures, higher values of about 0.5–0.6 eV may be more appropriate. Because the detailed-balance model merely assumes that the converter and the radiator are in equilibrium, it seems likely that this indeed provides an upper limit on the performance. The longer-term view ought to be that the empirical approach gives an idea of what might reasonably be expected from the materials and devices of today, whereas the detailed-balance approach gives the upper limit (in just the same way as does the Carnot efficiency of a heat-engine) toward which progress may be made. The original point made by Cody et al. was that the performance of the best research solar cells of today exceeds that predicted on the basis of semi-empirical models developed in the early years of PV R&D. If the same were true of TPV cells, then the increased performance could open additional applications and markets not accessible if the predictions of the empirical model are correct. To test this, a well-funded and sustained National Program in TPV is needed.

3.6. Potentially suitable materials

At this early stage, it is clear from the arguments above that a semiconductor with a bandgap in the range of 0.5–0.6 eV is required with which to fabricate the device. This range of bandgaps does not correspond to any of the commonly available binary substrate materials (such as InP or GaAs, for example). Consequently, it is necessary to consider the possibilities carefully. At the time of writing, none of the materials investigated appears to have a commanding advantage in actual devices.

Figure 18 shows the well-known diagram of energy gap vs lattice constant for some of the III–V binary and ternary compounds and alloys. This indicates that to obtain the required bandgap semiconductors, relatively unfamiliar materials must be used. Wanlass et al. [55] and Wilt et al. [37] grew $In_xGa_{1-x}As$ lattice-mismatched on an InP substrate [6] by making their material In-rich. This configuration means that the layer is in biaxial compression and, when the concentration of indium is sufficiently large, dislocations form to relieve the strain. These can impair the performance of the device, and Wanlass et al. [55] pointed out that when the bandgap is decreased to 0.5 eV, the

---

[6] $In_xGa_{1-x}As$ is lattice matched to an InP substrate for a value of $x = 0.53$.

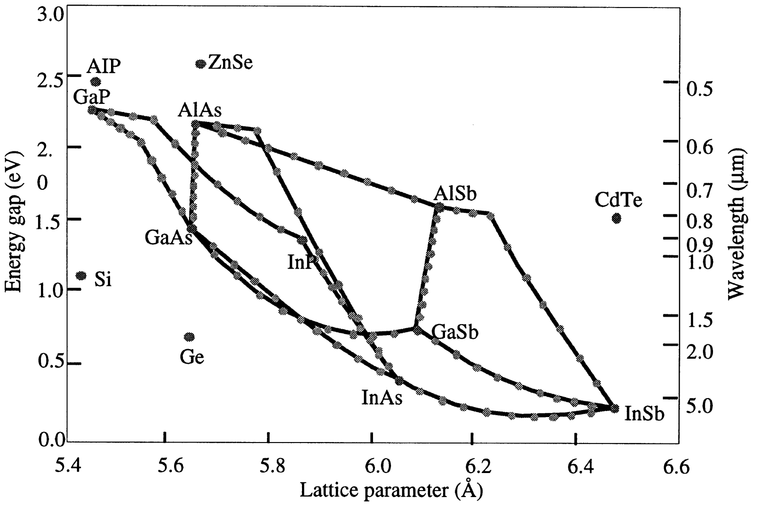

Fig. 18. Diagram of the bandgap of various compound and alloy semiconductors from the III–V family.

device performance deteriorates severely. At 0.5 eV, however, the performance was excellent, as will be discussed later.

Martinelli et al. [56] and Wang et al. [57] fabricated diodes from the quaternary alloy $Ga_xIn_{1-x}As_ySb_{1-y}$. This can be grown lattice-matched on either a GaSb or an InAs substrate with the desired bandgap. In the former case, the values of x and y are 0.198 and 0.444, respectively, for a bandgap of approximately 0.5 eV, lattice-matched to the GaSb substrate. The main attraction is that the GaSb substrate is transparent to the sub-bandgap radiation (at least to the extent that it does not exhibit radiative transitions) and back-surface reflection should be feasible. However, the devices to date have not exhibited sufficiently improved performance over the lattice-mismatched devices to justify the additional complication of a fourth element. Devices based on the quaternary alloy are discussed later in this section. It may be that it is not possible to fabricate GaSb in a semi-insulating form. Other options are possible, including alloys from the II–VI family, as illustrated in Fig. 19. More will be said below about GaSb- and InGaAs-based devices.

Thin-film options have been discussed by several authors including Contreras [17], Dhere [18], and Biter [19]. Figure 19 shows the diagram of bandgap vs lattice-constant for the II–VI compounds and alloys, from which it is clear that there are many other compounds and alloys that could be considered. To date, the only polycrystalline thin-film converter that has been used was based on copper indium selenide [19]. None of the other semiconductors in the II–VI family has been used. Although polycrystalline semiconductors are unlikely to perform as well as single crystals at the relatively low fluxes experienced by flat-plate solar cells, at high fluxes there is evidence [58] that their performance may improve disproportionately, possibly because of the saturation of recombination centers.

In the rest of this section, a detailed review of the papers on GaSb- and InGaAs-

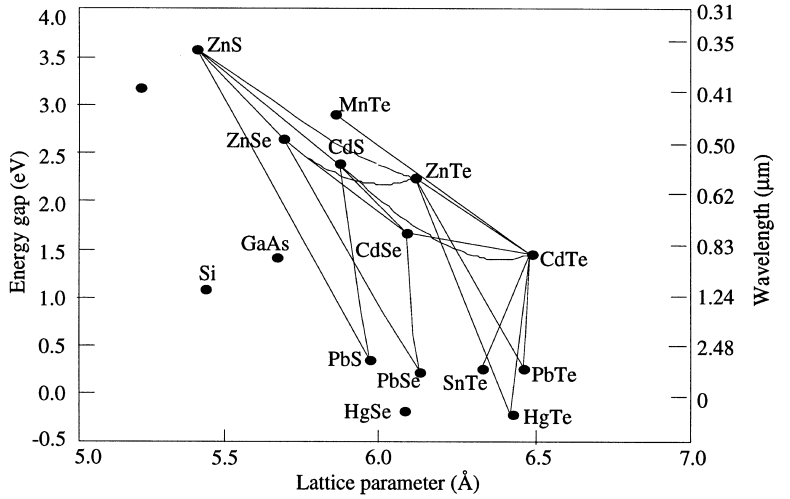

Fig. 19. Diagram of the bandgap of various compound and alloy semiconductors from the II–VI family.

related materials and devices will be given. This review is based on the papers that were presented at the Third NREL Conference. They represent an excellent collection of papers on the subject and give a review of the state of the art of the converter part of this technology.

3.7. *TPV converter fabrication and characterization*

In this section, we shall discuss the growth of the semiconductor layers that are used as the TPV converters, their fabrication into diodes, and the assembly of these into monolithic integrated modules. We shall concentrate on devices based on the III–V semiconductors $In_xGa_{1-x}As$ and GaSb, but shall omit silicon devices in the belief that these involve a far-better-known technology, even if they are less familiar in the context of TPV. Work on emerging materials, such as $Ga_xIn_{1-x}As_ySb_{1-y}$, is far less advanced, and very little work has yet been performed on TPV devices, much less on submodules. On the other hand, this family of materials has been quite widely used for the construction of medium-wavelength lasers. The small amount of work on the ternary and quaternary alloys will be reviewed.

3.7.1. *TPV converters based on GaSb*

Fraas et al. [59] pointed to that it will inevitably be difficult for a typical solar cell to generate significant amounts of electricity. It was argued that a 10%, 1-cm^2, one-sun cell would take 50 years to produce 1 kw-h of electricity. On the other hand, concentrator solar cells could produce the same amount of energy in only 100 days. However, in geographically low insolation areas, solar cells are not a viable alternative. In such areas, thermophotovoltaics, particularly those used in a cogeneration mode, may be attractive.

The approach of Ferguson et al. [32], for the efficient operation of TPV converters, was to use GaSb cells coupled to a ceramic radiator of $MgAl_2O_4$. The latter material may be doped with cobalt so that it radiates across a wider wavelength than the strongly selective rare-earth oxide radiators, but a range that corresponds well to the response of the GaSb cells. This device was the basis of the first quasi-production TPV generator to undergo beta testing. Some interesting economic arguments were made [32] to demonstrate that the GaSb cells used were not the cost-limiting factor in the TPV system. The basis of the argument was that the actual costs of the materials of a single-crystal semiconductor are trivial compared to the cost of processing the raw materials into the single crystal. The GaSb cells may be fabricated by diffusion of an *n*-type dopant into single-crystal *p*-type wafers. It was argued that epitaxial processes are inevitably expensive because of costs associated with safety and low wafter throughput. However, it should be noted that modern vapor-phase epitaxy (VPE) reactors are commercially available for metal-organic chemical vapor deposition (MOCVD), which, although capital intensive, are not severely limited in throughput.

One 3-inch-diameter GaSb crystal, which can be grown in one day, can be sliced to produce 110 3-inch-diameter wafers. Assuming that the crystal-growth equipment operates on a single-shift basis for 52 weeks a year and that wafers are produced with 90% yield, 25,000 wafers per year could be produced. A single wafer can be cut into 20 individual cells of 1 cm^2, each of which would produce 2 W. Hence, the output from a single crystal puller could generate the equivalent of 1 MW per year, A summary of all the costs associated with the manufacture of these cells gave an electricity cost of $1.97 per W at a 1-MW volume. Further analysis showed that losses in rounding and slicing led to substantial losses of materials. These could be greatly reduced by using 4- or 6-inch wafers. However, it must be noted that the cost of the associated crystal growers would be considerably greater than that of the original 3-inch diameter puller. In addition, the use of a wire saw rather than an internal-diameter saw would also reduce kerf losses.

Market research suggested that there maybe as many as 20,000 potential customers per year purchasing solar panels for remote locations. It is believed that these customers would also consider TPV generators as a viable alternative. The company's economic analysis was supported by a study on self-powered gas furnaces. Northeastern United States and eastern Canada experience electricity outages of greater than four hours in duration each year, and many customers would be prepared to pay a premium of as much as $500 extra for a self-powered furnace. In these, the electricity for the forced-air blower and the water pump for radiator heating would be supplied by a 200-W TPV array coupled to an infrared radiator heated by the gas itself. Consequently, in a time of electricity outages, the furnace would not be incapacitated. This appears to be a potential market of significant volume.

Despite these superficially convincing economic arguments, given that they were provided by the company itself, the conclusions can hardly be taken as surprising. Although they are not necessarily incorrect, it would be reassuring to have an independent economic study conducted. The dismissal of the cost of the converter and the assignment of the bulk of the system cost to the balance-of-system components seems intuitively questionable and requires independent ratification.

Dutta et al. [60] argued that the synthesis and growth of bulk GaSb is simpler than that of several other compound semiconductors of the III–V family of binary compounds. In particular, it has a relatively low vapor pressure and is less toxic than either arsenic or phosphorus, meaning that high-pressure growth is unnecessary. Also, the growth temperature is much lower than the other compounds. The focus of the work was obtaining GaSb and $Ga_{1-x}In_xSb$ single crystals of high structural quality. However, GaSb and its related alloys typically have a high concentration of electrically and optically active native defects, and the objective of these authors was to reduce this concentration.

A multi-zone furnace with computer control over the temperature profile was used in the work, together with the vertical Bridgman technique, which typically results in lower defect densities than Czochralski growth. However, the formation of a Ga_2O_3 scum on the melt tended to cause problems. Liquid encapsulation of the growing boule with low-melting-point salts was used to relieve stress from the walls during growth. In addition, a baffle was used to facilitate uniformity of the melt during growth.

Both undoped (*p*) and tellurium-doped (*n*) GaSb crystals were grown in silica crucibles, and the liquid encapsulants were LiCl : KCl, B_2O_3, and Sb_2O_3. The growth of InGaSb crystals was done without a seed, in flat-bottom crystal silica crucibles. Great care was taken to ensure the cleanliness and dryness of the charge and of the various components of the growth systems. This minimized the formation of the problematic surface scum that led to sticking of the charge to the walls of the ampoule. To ensure that the liquid encapsulant was free of moisture, it was subjected to a high-temperature baking cycle in vacuum before growth. This was done for a period of 10–12 h. After baking, the furnace was back-filled with one atmosphere of argon and heated to slightly above the melting temperature of the GaSb. The pre-synthesis baking step was vital for good-quality crystals, and without this, the encapsulant stuck to the charge and to the crucible and was difficult to remove. However, with baking, the encapsulant could be removed with hot water or methanol. The GaSb crystals were typically 30–50 mm in diameter and 70–80 mm in length. The lowest concentrations of dislocations was found when a temperature gradient of 10–15°C cm^{-1} near the solid–liquid interface was used. However, these crystals still exhibited twins, the mechanism of formation of which was not well understood. These twins reduced the yield of crystals, which were otherwise of high-quality single-crystal grains. Various changes in the design of the ampoule reduced twinning, and the best crystals were relatively free of twins in certain regions of the ampoule. These also had relatively low dislocation densities between 500 and 1000 cm^{-2}. Both undoped (*p*) and tellurium-doped (*n*) crystals were grown, and their electrical properties were measured. The undoped crystals typically had mobilities of about 500 and 1500 cm^2 V^{-1} s^{-1} at 300 K and 77 K, respectively. At the same temperatures, the mobilities of the *n*-type crystals were 1876 and 6281 cm^2 V^{-1} s^{-1}, respectively, the carrier concentration being about 6×10^{18} cm^{-3}.

The InGaSb crystals were grown in flat-bottom crucibles. The preferential rejection of InSb at the solid–liquid interface during growth is typical in the growth of InGaSb crystals, and it leads to a non-uniform profile of In in the axial direction of the boule.

The initial concentration of In was 3 at .%, but the final concentration in the crystals depended on the specific growth conditions. The crystals had imperfections caused by cracking, a problem which must be solved for the growth of higher-quality crystals.

Work performed by Bett et al. [2] concerned the formation of *p*/*n* junctions on single-crystal Te-doped, *n*-type GaSb. *P*-type doping of the emitter was achieved via diffusion of zinc, either from the vapor phase in a pseudo-closed-box system, or by diffusion from a liquid melt containing zinc. The single-crystal substrates were (100)-oriented and had an initial electron concentration of 3×10^{17} cm^{-3}. A variety of diffusion times and temperatures was used, and the Zn profile was measured using several techniques. Figure 20 shows the profile of the concentration profile of Zn as a function of the depth for three different diffusion temperatures, after one hour. Notice that the surface concentration reached about 10^{20} cm^{-3} after one hour, independent of the diffusion temperature. These profiles were measured using secondary-ion mass spectroscopy (SIMS). The hole concentration was measured using Raman spectroscopy and electrochemical C/V profiling. The agreement between SIMS and Raman spectroscopy indicated that almost all the diffused Zn atoms were electrically active. Figure 21 shows the time dependence of the surface concentration of Zn and the thickness of the *p*-type layer as functions of the square root of the diffusion time, whereas Fig. 22 shows the concentration of free holes and electrons (measured by Raman spectroscopy) as well as that of Zn atoms, measured by SIMS. As can be seen, the agreement between the hole concentration and the Zn atom concentration is excellent. A similar result was found when comparing capacitance/voltage profiling and SIMS. In this case, the diffusion source consisted of Zn and Sb vapor sources.

Diffusion from the liquid phase was performed into similar substrates, using a Ga–

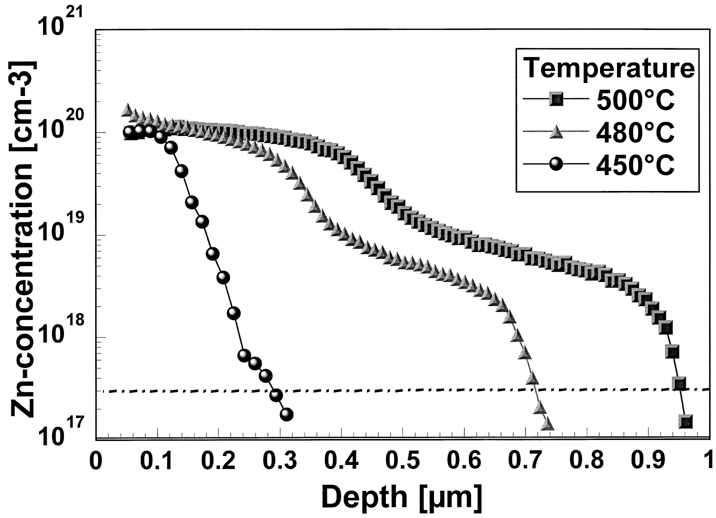

Fig. 20. Profile of the concentration profile of Zn as a function of the depth, for three different diffusion temperatures, after one hour. Reproduced by permission of the American Institute of Physics, and the author(s) [2].

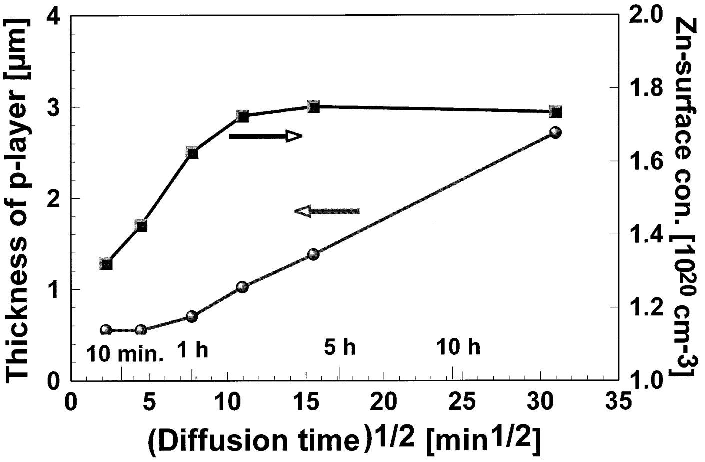

Fig. 21. Dependence of the surface concentration of Zn and the thickness of the *p*-type layer as functions of the square root of the diffusion time. Reproduced by permission of the American Institute of Physics, and the author(s) [2].

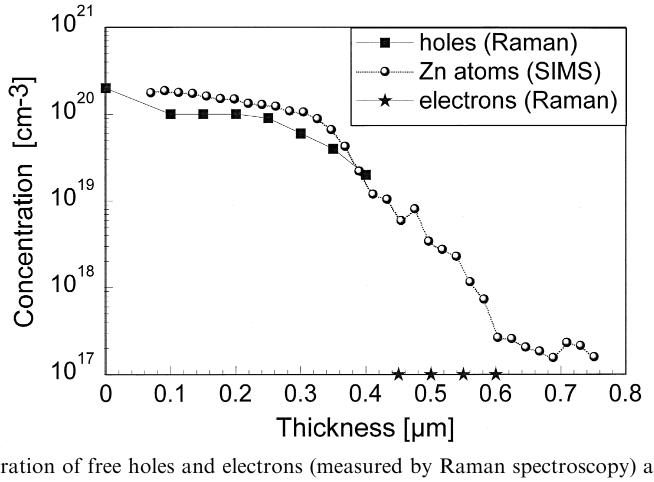

Fig. 22. Concentration of free holes and electrons (measured by Raman spectroscopy) and of Zn atoms, measured by SIMS. Reproduced by permission of the American Institute of Physics, and the author(s) [2].

Sb–Zn melt. To achieve wetting of the substrate by the melt, it was necessary to bake it at 600°C for one hour, prior to the diffusion process. This eliminated native oxides and helped dissolve the Ga–Sb–Zn melt homogeneously. More problems were found with liquid-phase than with vapor-phase diffusion, and the reproducibility was poor, as well as the surface concentration being lower.

In the case of vapor-phase diffusion, the *p*-type layers were thinned using anodic oxidation to reduce the thickness of the emitter to ~0.5 μm. This was maintained constant for all devices. Figure 23 shows the measured external quantum efficiency of a GaSb cell, with a single-layer Si_3N_4 antireflection coating. The dotted line shows the external quantum efficiency and the solid line shows the reflectance. The variation of open-circuit voltage (V_{oc}) as a function of short-circuit current density (J_{sc}) was also measured. In addition, a variety of cell areas and grid designs was used to establish their effect on the short-circuit current density. Under the assumption that 60% of the blackbody radiation reached the cell, it was calculated that the efficiency for radiant sources in the range 1250–1750 K was between 20 and 25%. Figure 24 shows variation of efficiency with the blackbody temperature. The upper curve is the calculated efficiency based on only wavelengths up to 1800 nm, whereas the lower curve includes the whole of the blackbody spectrum. The implication is that very effective longwave photon recirculation is required to obtain maximum efficiencies. The output power and efficiency for several blackbody temperatures are summarized in Table 2.

Overall, the work by Bett et al. [2] is very supportive of the elementary device performance modeling discussed earlier and demonstrates that GaSb can be used effectively, even though its bandgap may be somewhat larger than ideal. Even this is untrue if the temperature of the converters rises to only 80°C.

Ehsani et al. [61] investigated the growth and characterization of $In_{0.2}Ga_{0.8}Sb$ device structures grown on GaSb substrates using metal–organic vapor-phase epitaxy (MOVPE). The layers were doped with Te, and the paper was mainly concerned with the structural characterization of the epilayers. These were tilted with respect to the substrates, the tilt increasing with epilayer thickness.

The ternary layers were grown on (100)-oriented GaSb and on semi-insulating GaAs substrates. Growth was performed in a low-pressure, rf-heated, horizontal MOVPE reactor. The GaSb substrates were low-resistivity *p*-type at room tempera-

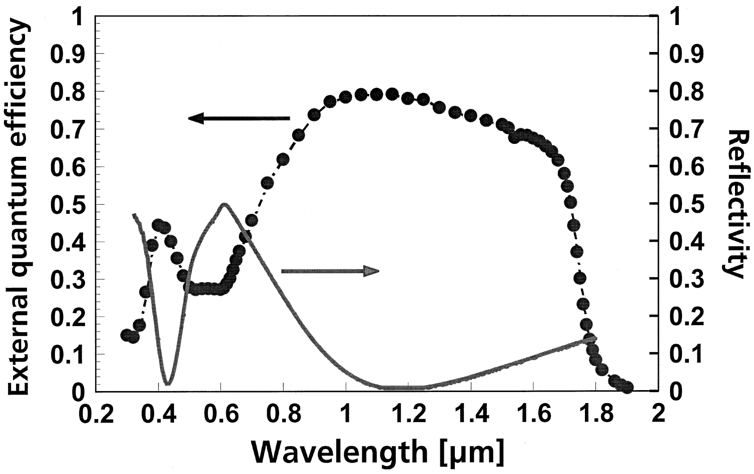

Fig. 23. Measured external quantum efficiency of a GaSb with a single-layer Si_3N_4 anti-reflection coating. Reproduced by permission of the American Institute of Physics, and the author(s) [2].

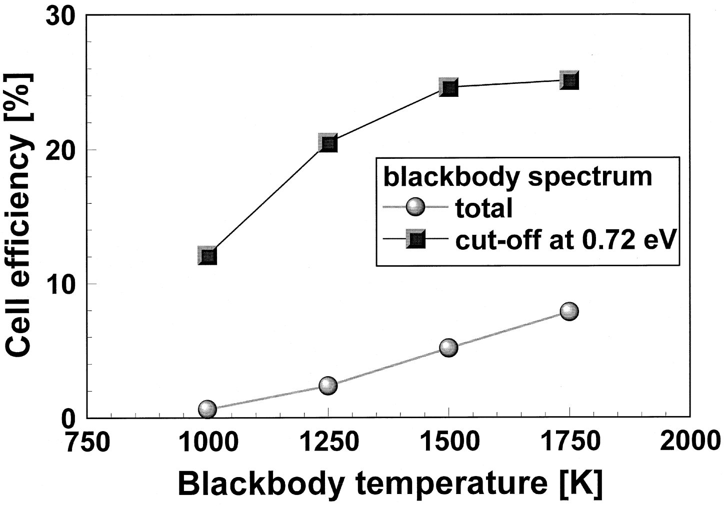

Fig. 24. Variation of efficiency with the blackbody temperature. Reproduced by permission of the American Institute of Physics, and the author(s) [2].

Table 2
Variation of the power density output and efficiency of diffused-junction GaSb TPV converters for various radiator temperatures [2]

Radiator temperature (K)	Power density output (m Watts cm^{-2})	Efficiency (%)
1000	27	12.1
1250	328	20.5
1500	1443	24.6
1750	4083	25.1

ture, but were high resistivity at 77 K, thus enabling the hole mobilities of the epilayers to be measured. Double crystal X-ray diffraction was used to determine layer tilt, the quality of the layers, their composition, and the lattice relaxation. The separation between the X-ray peaks of the epilayers and the substrates was used to assess the lattice mismatch and the epilayer tilt. The *n*-type dopant source was diethyl tellurium, and SIMS measurements indicated that only 2–3% of the incorporated Te atoms were active for a Te concentration of $\sim 2 \times 10^{19}$ cm^{-3}. A dilute Te source was also used and delivered via a second gas delivery line. This yielded a higher activation of Te. At 77 K, the mobility of electrons in the GaInSb epilayers grown on GaSb substrates was 6000–8000 cm^2 V^{-1} s^{-1}.

Several device structures were grown using two-step grading techniques. The first grading scheme consisted of a layer of 15 steps and 0.3 μm thick, grown on the GaSb substrate. The grading finished with the $In_{0.2}Ga_{0.8}Sb$ active layer. The second scheme consisted of an initial buffer layer of $In_{0.14}Ga_{0.86}Sb$, 0.15 μm in thickness, grown on the GaSb substrate. This was followed by a 5-step grading layer, 0.3 μm in thickness, and finishing with the same composition active layer. High-resolution cross-sectional microscopy showed that the upper layers in the step-grading structures bent threading dislocations away from the interface with the active layers so that the latter were relatively free of damaging dislocations. The X-ray studies indicated that the tilt of the layers increased monotonically with film thickness. Interestingly, the full width at half maximum (FWHM) of the step-grading layers initially increased to a film thickness of 0.6 μm, after which it decreased between 0.6 and 2.5 μm, due to annihilation of defects. The latter is a significant result for device fabrication, and the result is shown in Fig. 25.

Sundaram et al. [62] fabricated diffused-junction devices using diffusion into GaInSb and GaInAsSb substrates. Zinc was diffused into (100)-oriented, *n*-type GaInSb substrates, whereas the quaternary alloy was grown by liquid-phase epitaxy (LPE). This was used as the substrate for zinc diffusion. In general, GaSb and related materials are *p*-type as grown, but may be doped *n*-type with a group VI impurity. In this case, *n*-type substrates were used. Zn was diffused from a pseudo-closed-box, and the *p*-type and *n*-type contacts were made using titanium/platinum/gold and gold/tin/gold to the *p*-type regions, respectively. The grids occupied about 7% of the surface area, and an antireflection coating of Si_3N_4 was deposited. The cells were tested under a solar simulator equipped with a 1-kW Xenon-arc lamp. With concentration, the incident irradiance was 2.5 W cm^{-2}.

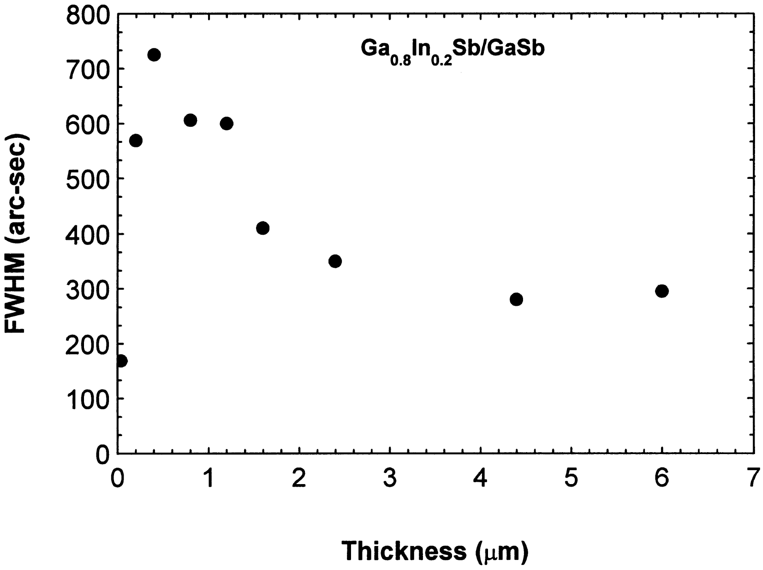

Fig. 25. Variation of FWHM of XRD peak of GaInSb with the thickness of the grading layer. Reproduced by permission of the American Institute of Physics, and the author(s) [61].

Current density vs voltage characteristics are shown in Fig. 26 for the binary, ternary, and quaternary devices. The authors stressed that, although not ideal, these characteristics are respectable, given the preliminary nature of their research. As expected, the fill factors and voltages decreased with reduction of the bandgap, as indicated by modeling discussed earlier. Plots of $\log J_{sc}$ vs V_{oc} indicated an ideality factor of 2 for the quaternary cells, whereas the ternary and binary devices exhibited diffusion-limited reverse saturation current (i.e. $n \sim 1$). The internal quantum efficiency of the three devices is shown in Fig. 27. This indicates excellent performance for the binary and ternary alloys, but with a significant decrease of performance for the quaternary alloy.

These devices were used in conjunction with a resonant antenna array band-pass filter (discussed in more detail in Section 4), the characteristics of which are shown in Fig. 28. Calculations indicated that the quaternary device had an efficiency of about 19% for a bandgap of about 0.58 eV, with a power-density output of ~0.4 W cm^{-2}. Variation of the efficiency and the power-density output are shown in Fig. 29, which confirms that the ideal bandgap for a compromise between these two quantities is ~0.58 eV.

Although bulk diffusion is an appealingly simple technique and lends itself well to mass production, it does not appear to yield the highest-performance devices. This is achieved using one of the conventional epitaxial growth techniques. Hitchcock et al. [63], for example, used MOVPE to grow layers of GaSb-related alloys and to measure the characteristics of devices based on these. The devices consisted of layers of GaInSb

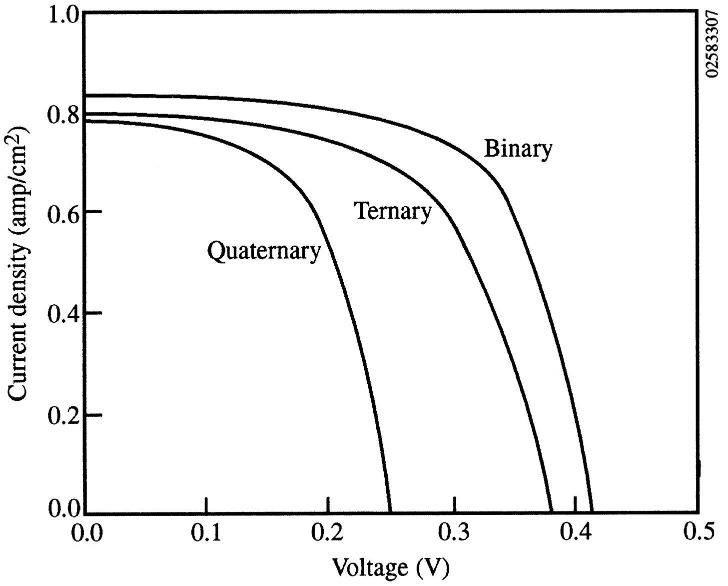

Fig. 26. Current density vs voltage characteristics for binary, ternary, and quaternary devices from the GaInAsSb family of alloys. Reproduced by permission of the American Institute of Physics, and the author(s) [62].

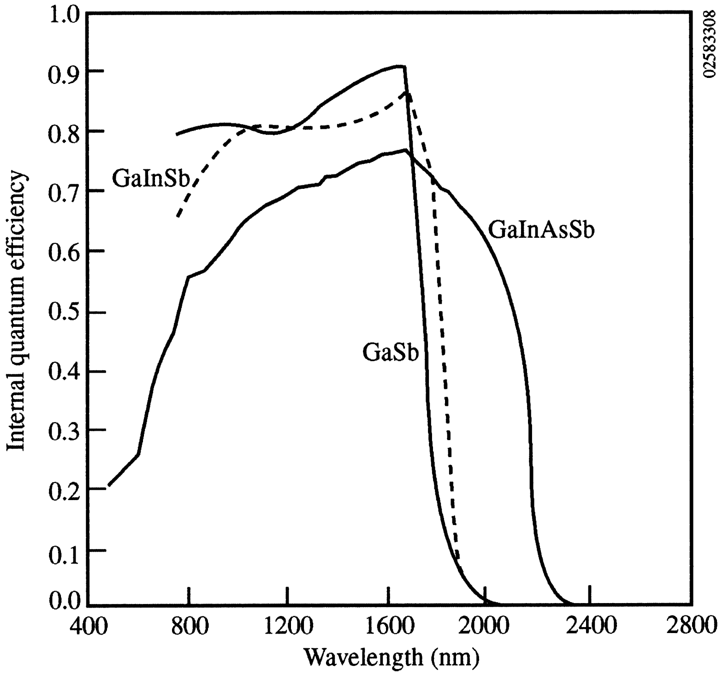

Fig. 27. Internal quantum efficiency of the three devices shown in Fig. 26. Reproduced by permission of the American Institute of Physics, and the author(s) [62].

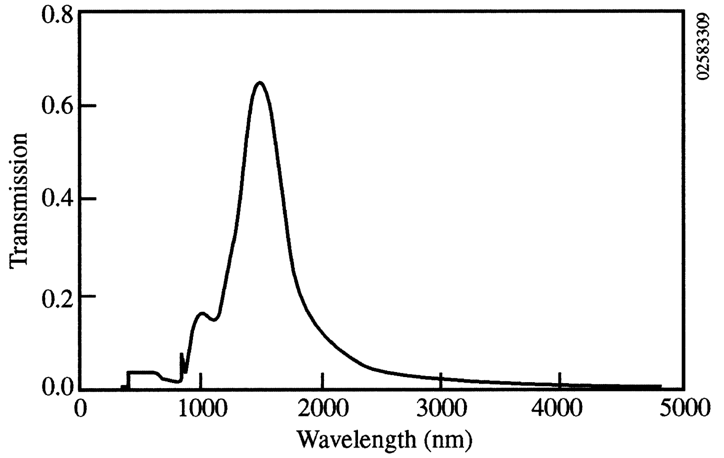

Fig. 28. Transmittance of a modeled resonant antenna array. Reproduced by permission of the American Institute of Physics, and the author(s) [62].

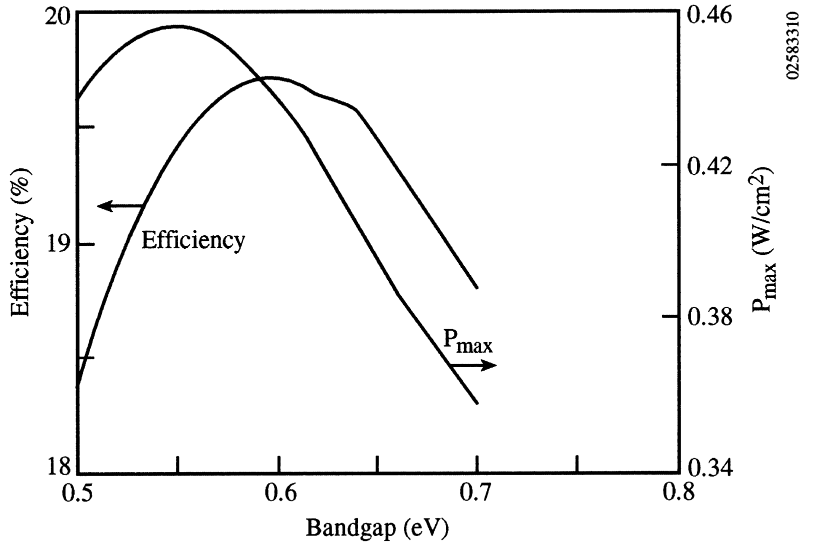

Fig. 29. Variation of the efficiency and the power-density output of a TPV device illuminated with an irradiance filtered by a resonant antenna array. Reproduced by permission of the American Institute of Physics, and the author(s) [62].

and GaInAsSb, and all the devices had bandgaps in the range 0.52–0.56 eV. The GaInSb was, of course, mismatched to the GaSb substrates, but the GaInAsSb was lattice-matched, as well as having the desired bandgap.

The GaInSb was grown by MOVPE, but the quaternary devices were grown by LPE. The GaInSb was grown using step-grading from GaSb at the substrate to $Ga_{0.8}In_{0.2}Sb$ for the device region. The quaternary devices were fabricated by LPE, with earlier devices depending on Ga anti-site defects for emitter doping, but with extrinsic doping by Ge for later devices. The composition of the quaternary layer was $Ga_{0.8}In_{0.2}As_{0.2}Sb_{0.8}$. In general, the substrates were *n*-type, and the back contacts were formed by evaporation of 100 Å of Sn followed by 2000 Å of Au. To achieve ohmicity, a post-deposition anneal was required. The back contacts were capped with 1–2 μm of Ag to permit probing, without damage to the substrate. *n*/*p* devices were also fabricated, but with these, the Au-based contacts shorted the device emitter. *p*-type contacts are trivial because the Fermi level is pinned near the valence band, and the formation of ohmic contacts is thus straightforward. For these, 2000 Å of a film of Au : 8% zinc was used. When these contacts were annealed, the specific contact resistance was found to be 10^{-5} Ω cm^2. In general, however, annealing was not used, to avoid shorting the emitter.

After front-contact deposition, the device area was defined using photolithography. However, some devices were made using the contacts to define the sizes of the mesas. The advantage of this was that the optical area of the devices was well defined. Detailed electrical characterizations were performed, with the emphasis being placed on the underlying physics rather than on achieving high efficiencies. The photoresponse of the devices was poor in the region of the bandgap for the active layers. This was attributed to a poor diffusion length in the base, which may possibly be remedied by refining the growth process.

The focus of the work undertaken by Martinelli et al. [56] was to assess the minority electron diffusion lengths from the measured external and internal quantum efficiencies of 0.55-eV GaInAsSb *p*/*n* diodes. These were grown using solid-source molecular-beam epitaxy (MBE), and they were lattice-matched to GaSb substrates. It was indicated that, although InGaAs diodes are presently superior in performance, GaInAsSb has excellent minority-carrier transport properties, making it potentially ideal for TPV diodes. A cross-section of one of the devices studied is shown in Fig. 30, and the effects of both the emitter and base thicknesses on the transport properties were assessed. The *n*-type base was Te-doped to $\sim 2 \times 10^{18}$ cm^{-3}, and its thickness was varied in the range of 1–6 μm. The *p*-type emitter was Be-doped to 2–10^{17} cm^{-3}, and its thickness was varied from 1–8 μm. The 50-nm GaSb window layer and a top-surface GaSb buffer layer were provided to ensure minimal surface recombination of photogenerated carriers. The entire structure was grown on an *n*-type GaSb substrate, and a buffer layer of GaSb, with $n = 5 \times 10^{17}$ cm^{-3}, was initially grown. Consequently, the entire converter was a fully passivated double-heterostructure.

After growth, the epilayers were etched and isolated to form 500-μm-diameter mesas. The wafter was thinned to 150 μm, and its rear surface was metallized with Au/Ge/Ni/Au. Front contacts were made with Cr/Au. Mesa etching was performed using a bromine/methanol solution. The quantum efficiencies were measured in the wavelength range 1–2.5 μm and were converted to absolute values using a standardized

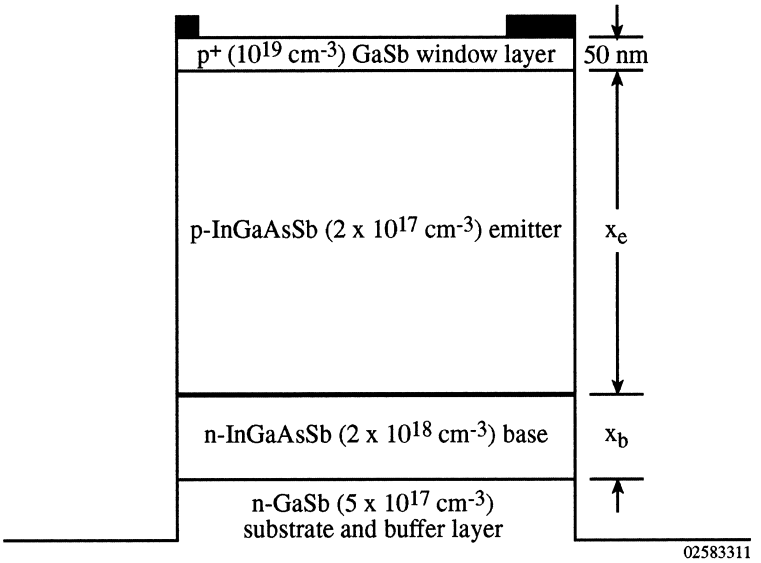

Fig. 30. Cross-section of a GaInAsSb device. Reproduced by permission of the American Institute of Physics, and the author(s) [56].

laser, with its output calibrated at 1.575 μm. External and internal QE data are shown in Fig. 31, indicating that the performance could be greatly improved with an anti-reflection coating. The QE data were fitted using the Hovel model, and values of the minority-electron and hole diffusion lengths were extracted. The electron diffusion length in the base appeared to be limited only by the base thickness, and it increased monotonically with this quantity. Estimates were also made of the hole diffusion length, and this was found to be about one tenth the value of the electron diffusion lengths. The latter were ~29 μm, whereas the former were less than 3 μm. This is presumably due to the larger effective mass of holes than electrons. The absolute internal quantum efficiency is greater than 80% over the entire spectrum measured and is greater than 90% between 1.4 and 2.1 μm. No comment was made about the reverse saturation current density, nor about the device efficiency and power-density output.

Wang et al. [57] grew $Ga_{1-x}In_xAs_ySb_{1-y}$ lattice-matched alloys grown on GaSb substrates using both organometallic vapor-phase epitaxy (OMVPE) and MBE. The authors commented that although InAs substrates could be used, GaSb was preferred because of thermodynamic, band structure, and mechanical stability issues. The electrical, optical, and structural properties of the alloys were measured, and *p*/*n* devices were grown and evaluated. the variables studied included the thicknesses of the base and emitter, and the use (or not) of a wide-bandgap AlGaAsSb window layer.

The OMPVPE layers were grown on (100)-oriented, Te-doped GaSb substrates

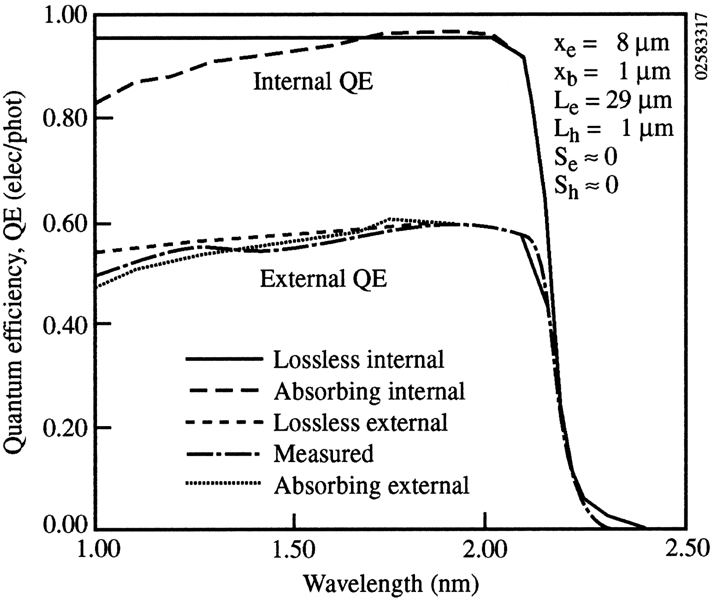

Fig. 31. External and internal quantum efficiency data of a GaInAsSb device. Reproduced by permission of the American Institute of Physics, and the author(s) [56].

and on semi-insulating GaAs substrates with slight misorientations in either the (110) or (111B) directions. For the deposition conditions and growth sources used, the growth rate was 2.7 μm per hour and the growth temperature ranged from 525–575°C. The alloys were grown by MBE from solid sources using conventional effusion cells, and the growth temperature was 500–510°C, resulting in a growth rate of 1 μm per hour. In the alloy $Ga_{1-x}In_xAs_ySb_{1-y}$, the bandgap depends on the concentrations of Ga and As, and it is given by:

$$E(x,y) = 0.726-0.961x-0.501y+0.08xy+0.451x^2+1.2y^2 +0.021x^2y+0.62xy^2. \quad (19)$$

If the alloy is to be lattice-matched to the GaSb substrate, then the As concentration is:

$$y(x) = \frac{0.867x}{(1-0.048x)}. \quad (20)$$

The alloy $Ga_{0.87}In_{0.13}As_{0.12}Sb_{0.88}$ has a bandgap of 0.57 eV, corresponding to a cut-off wavelength of 2.2 μm at 300 K. Various alloy compositions were investigated.

The carrier concentration and mobility of OMVPE-grown layers of this composition were 5–8 × 10^{15} cm^{-3} and 450–580 $cm^2\ V^{-1}\ s^{-1}$ for nominally undoped (p) material. Typically, majority electrons in n-type material had a mobility in the range 2000–5000 $cm^2\ V^{-1}\ s^{-1}$, depending on carrier concentration. The hole mobilities were about one-tenth of the values for electrons, due to higher effective masses.

Several device structures were made with the emitter thickness varying between 0.2 and 3 μm and the base thickness between 1 and 3 μm. All were grown on n-type GaSb substrates. Several of the devices had window layers of AlGaAsSb deposited that were 0.1 μm thick. In general, the doping of the p-GaInAsSb emitter was 2 × 10^{17} cm^{-3}. Mesa diodes of areas 0.5 and 1 cm^2 were fabricated using photolithography, and the collector grid was formed with a 1-μm-wide central bus-bar connected to 10-μm-wide grid lines on 100-μm centers. Ohmic contacts to p-type GaSb were formed from Te/Pt/Au and to n-type GaSb from Au/Sn/Ti/Pt/Au. The contacts were alloyed at 300°C. For these initial devices, no anti-reflection coating was used. The external quantum efficiency was ~40%, up to 2 μm wavelength. Devices with the AlGaAsSb window layer had considerably higher external quantum efficiencies, as shown in Fig. 32, an open-circuit voltage of ~300 mV and a short-circuit current density of ~1 amp cm^{-2}. Without the window layer, V_{oc} was 30–40% less. Figure 33 shows the room-temperature photoluminescence (PL) spectra of devices with and without the window layer. This emphasizes the effectiveness of the window layer. Calculations indicated that the enhancement of the PL spectrum was due to a reduction in the surface recombination velocity by more than one order of magnitude.

Although these results are very encouraging and indicate that the quaternary alloy GaInAsSb has great promise for the TPV converter, it is not yet at the stage where there is a convincing advantage over mismatched InGaAs, which will be discussed later.

Shellenbarger et al. [64] fabricated a variety of structures based on the quaternary

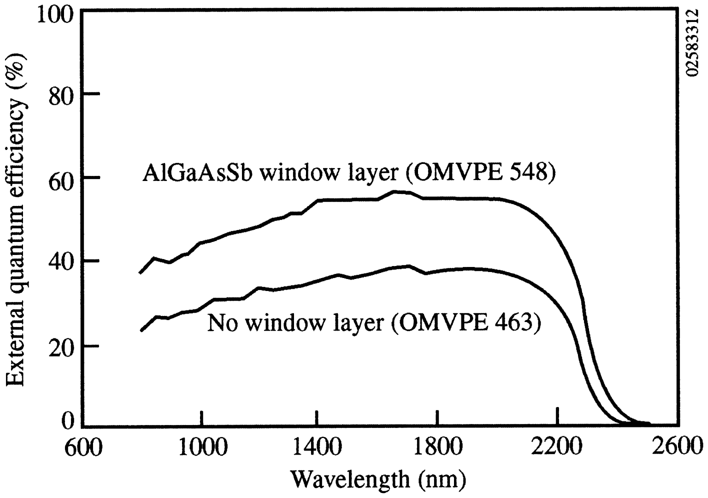

Fig. 32. Quantum efficiency of a GaInAsSb device with AlGaAsSb window layer [57].

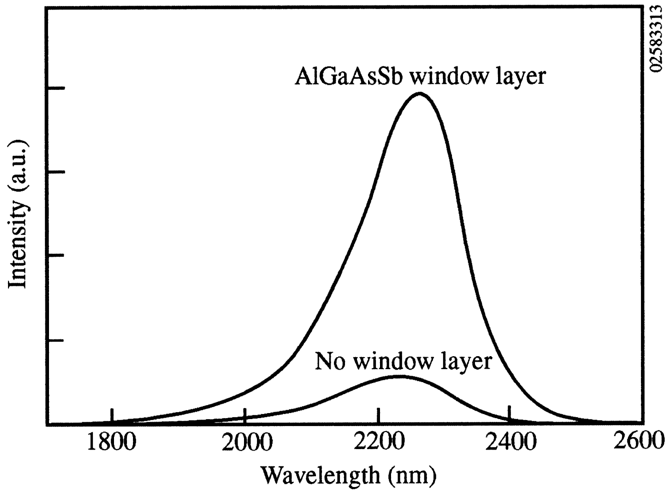

Fig. 33. Room-temperature photoluminescence spectra of GaInAsSb devices with and without a window layer. Reproduced by permission of the American Institute of Physics, and the author(s) [57].

alloy GaInAsSb grown by LPE on a GaSb substrate at a growth temperature of 515°C. The authors commented that the growth of the lattice-matched, ideal-bandgap, quaternary alloy is a simpler and more efficient approach to the fabrication of TPV converters than those based on mismatched ternary alloy layers. However, as seen in this lengthy section, there is little experimental justification to support this statement. The devices considered by Shellenbarger et al. [64] were quaternary alloy homojunctions, both with and without wide-bandgap passivating window layers, and heterostructures based on AlGaAsSb/GaInAsSb heterostructures. In addition, back-surface reflection of sub-bandgap photons was proposed by thinning the substrate after device fabrication.

The authors considered that LPE was attractive because of its excellent material quality and the long minority-carrier diffusion lengths usually achieved. In addition, they claimed that LPE is simpler, less expensive, and safer than MOCVD techniques. The substrates were *n*-type GaSb doped with Te to 3–5 × 10^{17} cm^{-3}. Prior to use, the melt was carefully baked in flowing hydrogen and doped with either Te or Ge to fabricate *n*-type and *p*-type alloys, respectively. The growth temperature was 515°C, and a 5-μm-thick *n*-type base of the quaternary alloy was grown first. This took only 2 min to grow, and it was followed by a 0.3-μm *p*-type GaInAsSb emitter. The composition of the wide-bandgap window layers was $\mathrm{Al_{0.3}Ga_{0.7}As_{0.02}Sb_{0.9}}$, which had a bandgap of ~1.2 eV. Ohmic contacts were formed by standard means, using either Sn : Au or Au : Zn : Au metallizations for *n*- and *p*-type regions, respectively. The front grid was thickened to 5 μm with electroplated gold. The devices themselves were patterned into 1 × 1-cm areas and isolated from adjacent services.

SIMS profiling confirmed that abruptness of the interface between the *p*- and *n*-type regions, although there was a discrepancy between the total concentration of Te and the electrical activity of Te, inferred from a comparison of SIMS and capacitance/voltage data. The grid shading was 18.2%: an unusually large proportion of the available surface area.

The internal and external quantum efficiencies and the current/voltage characteristics of homojunction devices were measured. With a thinned substrate (i.e., less than 100 μm), the reflectance of sub-bandgap photons was greater than 90%. Interestingly, the reverse saturation current density of an unpassivated device was ~1.5 × 10^{-4} A cm^{-2}, but this was decreased by more than one order of magnitude with the addition of a 1.3-eV-bandgap window layer. This layer also improved the voltage and fill factor of the devices, as was also observed by Martinelli et al. [56]. No advantage was found by using heterojunction devices. Although substrate thinning undoubtedly improved the sub-bandgap reflectance and the ability to operate the devices at minimally elevated temperatures, it is a complicated and possibly costly additional step in device fabrication. For larger-scale production, it seems questionable whether either LPE or substrate thinning could be cost-effective.

Mauk et al. [65] discussed various novel concepts for Sb-based alloys with a view to improving photon recycling, reducing cost, and providing SI substrates for development of monolithic interconnected module (MIM) devices. To achieve these objectives, several approaches were suggested. These included: (1) epitaxial lateral overgrowth on patterned substrates, (2) epitaxial film transfer using selective etching or lift-off, (3) heteroepitaxy on low-cost substrates, (4) the realization of semi-insulating GaSb, and (5) the use of steam-oxidation to provide insulating regions on GaSb substrates. The attraction of the approaches suggested is that they are well established for other semiconductors, such as GaAs.

The first concept proposed the use of buried mirrors to achieve sub-bandgap photon recirculation. For this, the use of a GaSb substrate with a mirror deposited on its front surface was proposed. The mirror may be a refractory metal, a metal nitride, a dielectric stack, or a semiconductor/dielectric combination. The mirror would provide electrical contact to the substrate and would be patterned with openings in it. The subsequent epitaxial layers would grow in the etched openings, directly on the GaSb substrate. The first layer could be, for example, an AlGaAsSb cladding layer to provide minority-carrier confinement.

With a buried mirror, patterned with strip-openings, the individual layers of the active devices would be grown on the strip-openings, and when their thickness exceeded that of the mirror, they would grow laterally, thus covering and burying the mirror. Mauk et al. [65] claimed to have obtained complete coverage of oxide-masked substrates with strip-openings separated by up to 100 μm.

As mentioned several times, the non-availability of a semi-insulating GaSb substrate is a disadvantage of GaSb-based converters compared with the $In_xGa_{1-x}As$-based converters. In the third concept, Mauk et al. [65] proposed doping the members of the GaSb-alloy family with transition metals such as Cr to move the Fermi level to the center of the bandgap, thus making the material semi-insulating, by analogy with GaAs.

The fourth concept involved the growth of GaSb-based epilayers directly on a GaSb substrate and the removal of this from the substrate using a superstrate and selective etching. This unfortunately, would inevitably be costly because of the etching step. However, after removal of the GaSb substrate, the active layers would be supported on the superstrate, which may be a semi-insulating material, thus permitting photon recirculation. The substrate may also be re-usable.

For the final concept, it was suggested that heteroepitaxy of films of either InAs or GaSb on Si could be used. This could then be used as a substrate for growth of the subsequent active layers. However, it is well known that there are severe problems in the growth of III–V semiconductors on Si. Although some of these have been solved for GaAs on Si, they have not yet been tackled for InAs or GaSb. However, these materials have advantages over heteroepitaxy of GaAs in that they have a lower growth-temperature, thus offering the potential for defect reduction. The lower growth temperature also implies that thermal stress and auto-doping would be less problematic. Finally, a wet thermal oxidation of a buried AlAsSb layer was described. This would provide a means of monolithic integration of epitaxial devices. These are all interesting suggestions that are worthy of further investigation.

3.7.2. TPV converters based on InGaAs

The monolithic integration of III–V devices was first used by Wojtczuk et al. [66] to fabricate power converters for laser-beaming experiments. Fatemi et al. [67] also described the fabrication of a monolithic interconnected module. In this approach, a single TPV cell is divided into several subcells, which are interconnected in series. This has the effect of reducing the current output of the single cell by a factor approximately equal to the number of subcells. The voltage output of the series string is increased by exactly the same factor. However, because of the reduction in Joule losses, the fill factor also increases (in principle). The net effect, therefore, is a gain in the power output. There are several key procedures that must be achieved in fabricating a successful MIM, and these were the subject of the paper by Fatemi et al. [68].

The MIM devices were fabricated by OMVPE deposition of the InGaAs layers on a semi-insulating (SI) InP substrate. Plan and cross-sectional views are shown in Fig. 34. The individual steps in fabricating the MIM are the etching of an isolation trench between the subcells; the deposition of a dielectric insulating layer; the deposition of a metal interconnect; the deposition of a back-surface reflector on the SI InP; and the deposition of an anti-reflection coating. Each of these aspects was investigated in the paper. Selective etchants were used to create the isolation trenches. HCl etches InP, but does not attack InGaAs, whereas phosphoric acid/hydrogen peroxide etches

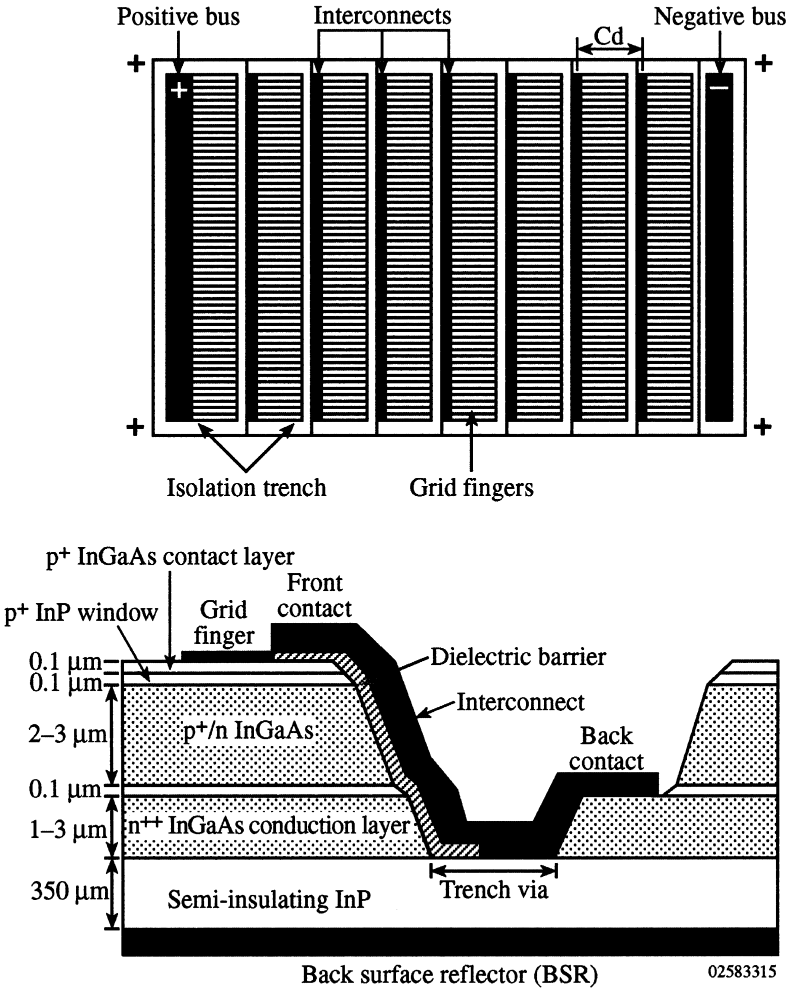

Fig. 34. Plan and cross-sectional views of an MIM device. Reproduced by permission of the American Institute of Physics, and the author(s) [67].

InGaAs but does not attack InP. Some undercutting is observed because of the chemical action of the etchants underneath the photoresist. The etching occurs on the (111) and (211) crystallographic planes, and it forms a V-shaped trench. This facilitates the deposition of the insulating layer and the metal interconnect. The width of the trenches was $\sim 12\ \mu$m. In later work, this was reduced to only 8 μm. However, the total width of the interconnect area was shown as 50 μm, which represents a significant fraction of the MIM area. A cross-sectional view of the etched structure is shown in Fig. 35.

Three different dielectric materials were investigated to provide electrical isolation between the metal interconnect and the side walls of the devices that were exposed in forming the interconnect trenches. These were spin-on glass, Si_3N_4, and Ta_2O_5. The Si_3N_4 showed excellent adhesion, isolation resistance, and dielectric breakdown strength. At the time of writing, this is the preferred insulator in the work performed by this group.

Various interconnect metals were tested, and both Cr and Ti, capped with Au, performed well. These were very adherent when deposited on the dielectric isolation layer. However, both Au–Ge–Au and Ag–Au contacts exhibited poor adhesion to the dielectric layer, thus presenting reliability problems. The specific contact resistance to heavily doped *n*- and *p*-type InGaAs was measured, using the transmission line method. CrAu and TiAu had adequately low contact resistances of less than $10^{-6}\ \Omega$-cm^2 on *n*-type InGaAs and about $10^{-5}\ \Omega$-cm^2 on *p*-type InGaAs. Contact resistances of this magnitude would not adversely impact the net power-density output from the MIMs. The reflectances of layers of both Ag and Au deposited directly on the back of the Si InP were excellent, with values greater than 95% being achieved. This could be improved by incorporating an intermediate layer of MgF_2, which, unfortunately, greatly worsened the adhesion. An adhesion layer of Ti or Cr overcame the adhesion problem, but reduced the reflectance excessively. The reflectance of Au-only and Ag-only layers is shown in Fig. 36. Thus, although there is still room for improvement, these values of reflectance would certainly not be a limiting factor in the device.

Anti-reflection coatings based on ZnS and MgF_2 were initially modeled over the wavelength range 1–2.4 μm. No indication of whether wavelength-dependent values of the optical constants were used for the ZnS, MgF_2, and 0.55-eV and 0.74-eV InGaAs. The calculated reflectances were less than 2% over the above wavelength range and agreed well with measurements. This paper is particularly useful and provided a thorough description of the individual steps that are used to fabricate the InGaAs-based MIM.

Wilt et al. [37] investigated the development of both lattice-matched and mismatched MIMs and argued strongly against the use of filters and other means of front-surface control of the sub-bandgap photons. On the other hand, the use of back-surface spectral control is potentially capable of giving much better results. The MIM consists of a series of device layers, grown on a SI InP substrate, processed into several series-connected subcells. An infrared reflector was deposited on the back of the SI substrate to reflect above-bandgap photons and to give them a second opportunity to be absorbed. In addition, sub-bandgap photons may be returned to the radiator from the back-surface reflector. However, very little appears to be known about re-absorption of sub-bandgap photons by radiators.

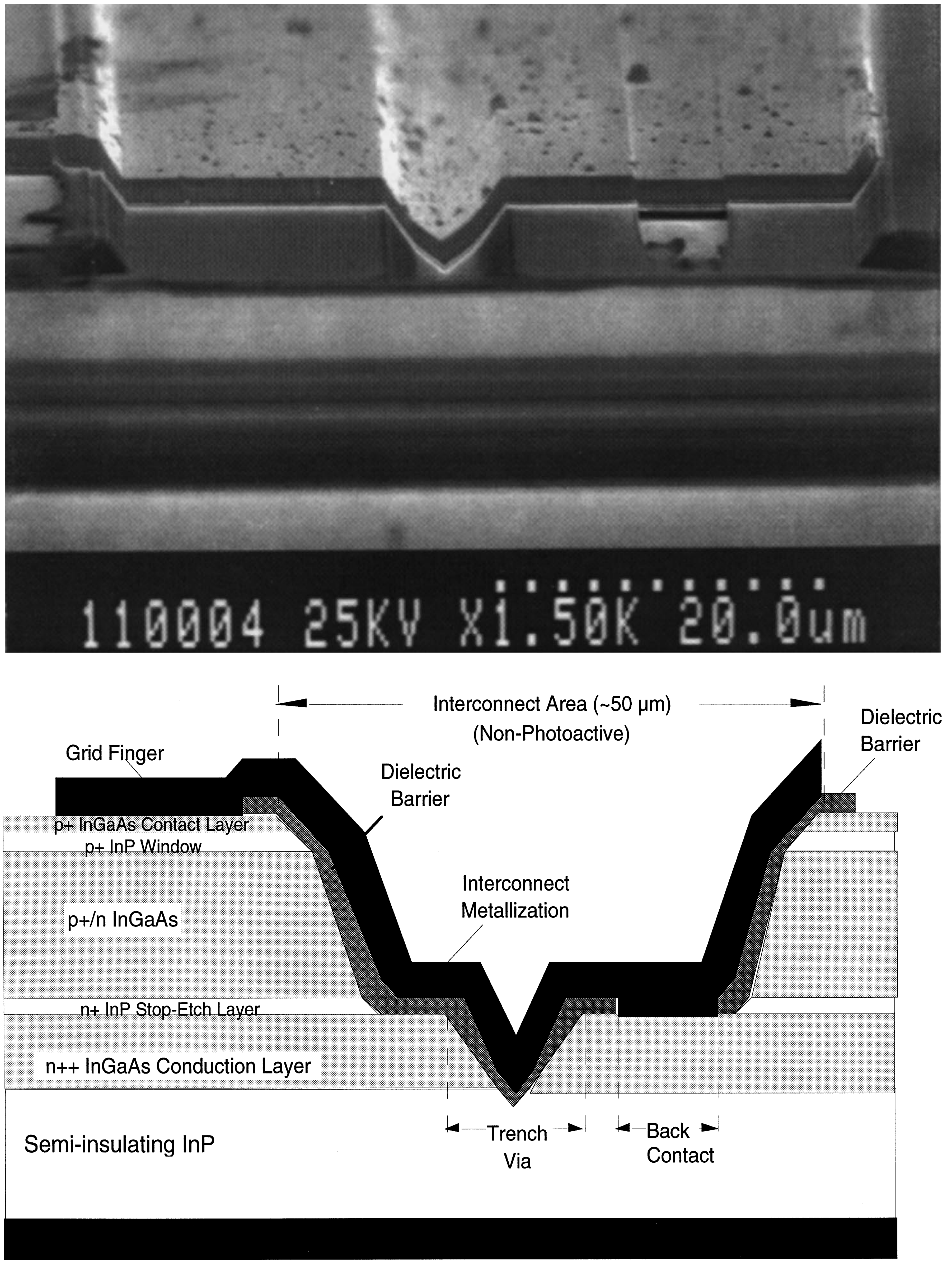

Fig. 35. Cross-sectional view of a complete MIM structure. Reproduced by permission of the American Institute of Physics, and the author(s) [67].

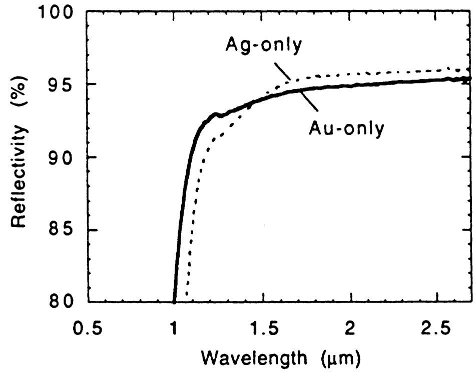

Fig. 36. Reflectance from an MIM with Au-only and Ag-only back-surface reflector. Reproduced by permission of the American Institute of Physics, and the author(s) [67].

Wilt et al. [37] pointed out that the MIM design has several potential advantages, including: reduced Joule losses, improved reliability, superior photon recirculation, improved thermal control, and increased absorption of above-bandgap photons.

The design of the cell allowed for free-carrier absorption in both the *n*- and *p*-type materials. The higher effective mass of holes causes the absorption in *p*-material to be 17 times greater than that in *n*-type material of comparable doping. Consequently, the device is likely to consist of a *p*-type emitter on an *n*-type base. The light electrons in *n*-type InGaAs, for heavily doped materials, cause a very large Burstein–Moss shift. Thus, the optical bandgap is shifted from its non-degenerate value of 0.73 to ~1.1 eV. This material may be used as a back-surface reflector and as an electrical conduction layer. Complete structures were developed for both 0.74 eV and 0.55 eV devices, and these consisted of n^{++}-InGaAs back-surface layers and p^{++}-top-surface contact layer. The top layer could be contacted without alloying. The contact layer was subsequently etched after metallization to remove the material between the grid fingers. The MIMS discussed consisted of eight subcells, which occupied an area of 1 cm^2. The grid collectors consisted of 7-μm-wide grid fingers on 100-μm centers, and the fingers were each 300 μm in length. More recently, mask sets have been developed to produce improved collectors.

Cells with thin bases and non-alloyed back contacts exhibited a higher internal quantum efficiency at the band-edge (1.66 eV) than predicted by theory. Cells with alloyed (optically diffuse) back contacts did not show this effect. The difference was possibly due to the non-alloyed contact acting as a specular back-surface reflector, Alloyed contacts form a strongly absorbing compound at the interface with the SI InP substrate and are not reflective, leading to a lower quantum efficiency. An eight-subcell MIM was tested under a flash-lamp spectrum, and it exhibited a $V_{oc} = 3.2$ V, $J_{sc} = 0$ 0.737 amp cm^{-2}, and a fill factor of 66%. The characteristic of a 0.74-eV MIM, tested under a flashlamp, is shown in Fig. 37. The external quantum efficiency of this device, shown in Fig. 38, peaked at around 65%, and the device is expected to produce 48.5 m amps when irradiated with blackbody radiation from a radiator at 1200 K.

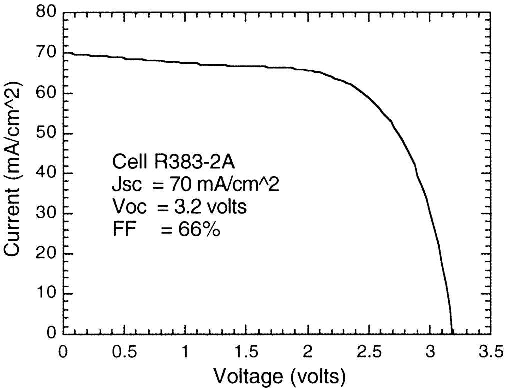

Fig. 37. Current/voltage characteristic from an MIM tested under a flash lamp. Reproduced by permission of the American Institute of Physics, and the author(s) [37].

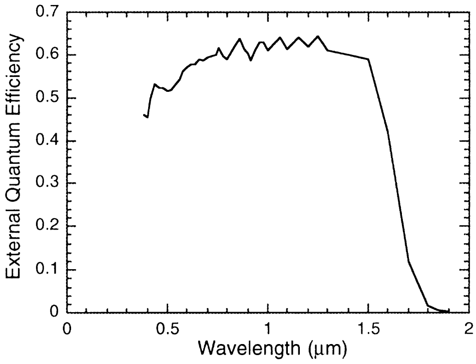

Fig. 38. External quantum efficiency of the device shown in Fig. 37. Reproduced by permission of the American Institute of Physics, and the author(s) [37].

Preliminary work was also performed on a more optimal 0.55-eV MIM. The current/voltage and external quantum efficiency data indicated reasonable performance, but showed that the device was limited by the quality of the dielectric isolation layer used to isolate the sidewalls of individual subcells. Since this time, greatly improved insulating layers of Si_3N_4 have been produced. Finally, it was stated that the longwave infrared reflectance from the back-surface reflector should be greater than 90%. This has been independently confirmed.

Wojtczuk [69] pointed out that although there is a reduction in the current density carried by a series-connected string of n subcells, for the Joule losses to be decreased, it is necessary for the total series resistance not to increase by more than n^2. It was assumed that the subcells were p^+/n and had a heavily doped n^+ back contact, that also served as the grading layer between the SI InP substrate and the devices. This configuration has the advantage that the back-contact layer is lower resistivity than an equivalent p^+ layer.

The current/voltage characteristics were measured of single-junction 0.55-eV cells and of a 0.74-eV (lattice-matched), 8-subcell MIM. The reverse saturation current density was estimated, from the diffusion regime of the single-junction characteristics, to be 2×10^{-5} amps cm^{-2}. This value was also assumed to be valid for p/n MIMs and for single-junction devices. It was then used to extract the series resistance from the diode equation. For a single-junction, 0.55 ev-cell, the series resistance was 0.03 Ω cm^2. For the 8-subcell MIM, it was 2.2 Ω. The ratio of the two series resistances was 73, whereas n^2 was only 64. Hence, it was believed that there would be no net benefit from the MIM design. Estimates were made of potential reductions in the two series resistances, which made the situation more favorable for the MIM; but the advantage was too small to justify the additional complexity of design. The additional resistance in the series-connected string is due to the current having to flow laterally in the heavily doped grading/back-contact layer.

The criticisms of Wojtczuk [69] of the series-interconnected MIM were answered in the paper by Ward et al. [70], who described a novel interconnect scheme that used the grid fingers themselves as the connections between the top of one subcell to the back of the adjacent subcell. Both electrical contacts are on the front surface of the MIM, which enables SI substrates to be used, thereby eliminating free-carrier absorption in the substrate. This approach also simplifies the assembly of arrays and the achievement of specific output voltages and currents through tailored series and parallel strings. The conventional MIM, described by Wilt et al. [37] and by Fatemi et al. [67] uses a front-surface grid and a heavily doped back-contact layer for transport to the back-contact metallization (See Fig. 35). The resistivity of this layer determines the magnitude of Joule and optical losses, and, therefore, the maximum permissible width of each subcell. For a fixed available area, it thus determines the maximum number of subcells per unit length and the output voltage. This greatly limits design flexibility. The design suggested and implemented by Ward et al. [70] provides for considerable flexibility in array design, and a schematic of the interconnection scheme is shown in Fig. 39.

The new interconnection scheme using the interdigitated front and back contacts still uses a heavily doped lateral conduction area, but this is grown on a SI substrate with a specular reflector on its back surface. Free-carrier absorption in the relatively thick substrate is eliminated because of the absence of free carriers. Joule losses can be minimized by selection of the spacing of the grid fingers and their sheet resistance. Thus, there are benefits to cell output flexibility, as well as reductions in both optical and electrical losses. The losses introduced by the spreading resistance of the lateral back-contact layer and by the grid fingers themselves are shown in Fig. 40. Clearly, the total losses due to these two sources are minimal.

The sequence of steps used to fabricate the MIM devices involves: etching the trenches for the back-contact grade; isolation of individual subcells by etching through the lateral conduction layer; deposition of SiO_2 and patterning; and finally, metallization. Although this sequence is similar to that described by Fatemi et al. [68], the end result is very different. In the interdigitated MIM design, current only needs to flow a maximum distance of half the spacing between the grid fingers, rather than the full length of the subcell. A scanning electron micrograph (SEM) of an isolation

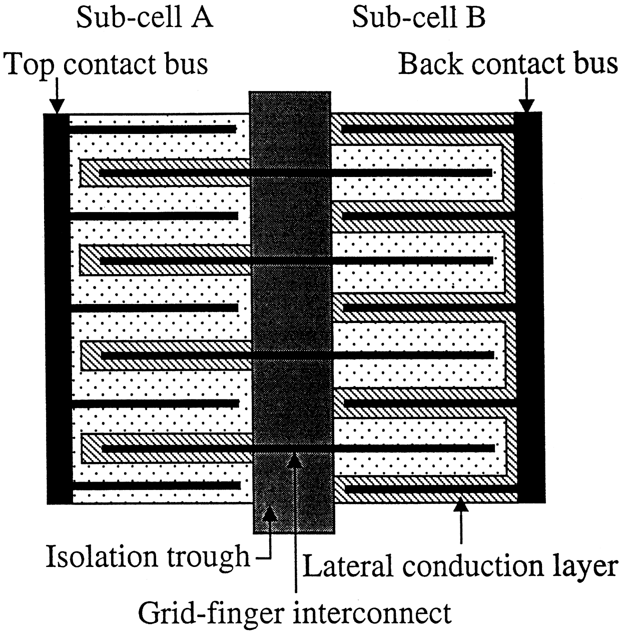

Fig. 39. Schematic of the MIM interconnection scheme used by Ward et al. Reproduced by permission of the American Institute of Physics, and the author(s) [70].

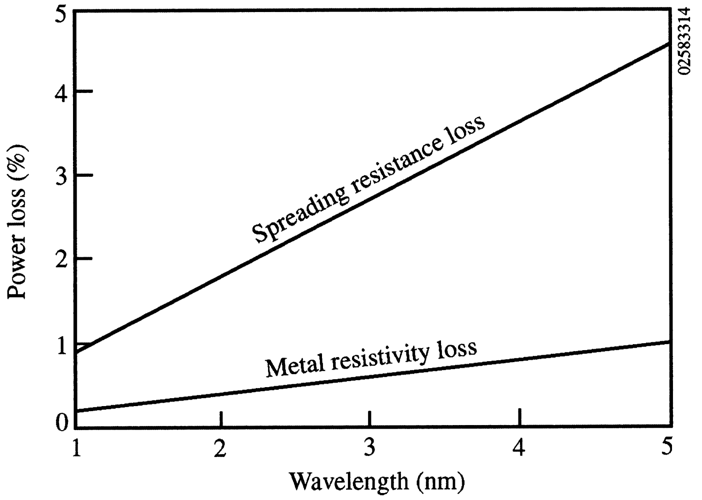

Fig. 40. Resistive losses introduced by the spreading resistance of the lateral back-contact layer and by the grid fingers. Reproduced by permission of the American Institute of Physics, and the author(s) [70].

trench, with a grid finger running from the back of one subcell to the top of the next subcell, is shown in Fig. 41. The prototype device was a 1-cm^2, 8-subcell MIM using

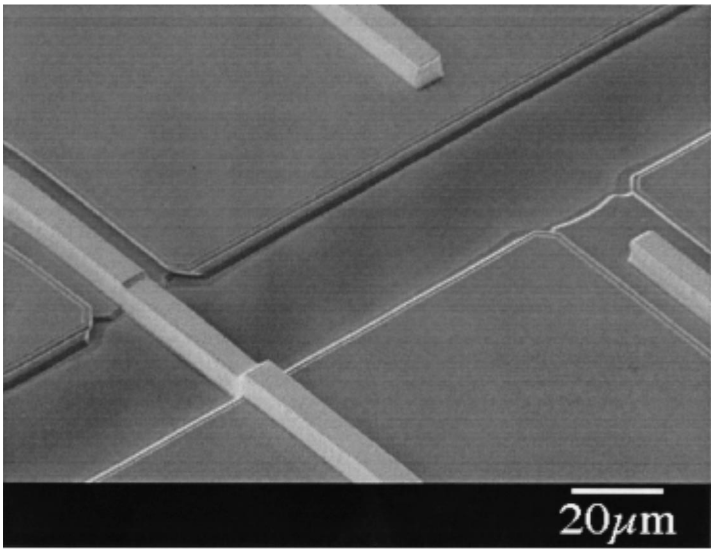

Fig. 41. SEM of an isolation trench and the grid fingers connecting the top of one subcell to the back of the next subcell. Reproduced by permission of the American Institute of Physics, and the author(s) [70].

0.74-eV InGaAs, lattice-matched to the SI InP substrate. It was found that the reliability of the grid-finger interconnects depended critically on being able to coat the sidewalls of the isolation trenches conformally. This required making the sidewalls in a V-shaped profile, as described earlier by Fatemi et al. [68]. If the trenches are etched perpendicularly to the major flat of the InP substrate wafers, then the sidewalls taper inward, causing cracks in the grid fingers and hence, reliability problems. When the trenches are etched parallel to the flat, the required V-shaped profile was obtained. The insulating layer was a 2000-Å-thick film of SiO_2, which had a breakdown strength greater than 10^7 V cm^{-1}. Pinholes presented a reliability problem, but this could be reduced or eliminated by ensuring that the deposition system was cleaned prior to deposition. The SiO_2 was deposited using low-pressure chemical-vapor deposition, and it coated the sidewalls of the GaInAs trench conformally.

In one test, an array of nine 1-cm^2 MIMS was connected in series. The string gave an open-circuit voltage of excess of 30 V, and the active area occupied by the grid fingers was less than 15%. Electrical performance of the lattice-matched MIMs was measured for various operating temperatures under a simulated 1000°C blackbody spectrum. The data are shown in Table 3. The results indicate that even for these developmental MIMS, and with a non-ideal bandgap for the radiator temperature, the power output approached 0.3 W cm^{-2}. In addition, the fill factors shown are considerably greater than those reported by Wilt et al. [37] and by Wojtczuk [69], indicating that the interdigitated grid-finger interconnect worked very effectively.

No anti-reflection coating was applied in the device discussed in Table 3, and an increase in power density of ~30% can be expected to result from the use of a well-designed anti-reflection coating. In principle, almost 1 W cm^{-2} is expected from the

Table 3
Parameters of an eight-subcell MIM, measured at various operating temperatures [70]

Operating temperature (°C)	V_{oc} (V)	J_{sc} (amps cm^{-2})	Fill-factor ($)	Power density (W cm^{-2})
16.9	3.62	0.907	72.04	0.292
32.6	3.47	0.948	70.40	0.284
60.6	3.32	0.991	67.07	0.257

cell when used with a blackbody spectrum from a 1000°C radiator; but given the losses associated with reflection, grid obscuration, and grid fingers, this initial result is most encouraging.

4. Photon recirculation

4.1. Introductory remarks

The need to return the sub-bandgap photons to the radiator to maximize the efficiency of the system was discussed in the last section. Without recirculation, efficiencies are low because the sub-bandgap photons simply cause heating of the system enclosure, the semiconductor, and the support structure. However, this does not necessarily exclude such systems from consideration because cogeneration of heat and electricity is attractive for some applications. In Sweden [1], for example, community heating schemes are in widespread use, and cogenerative TPV systems are being seriously considered, with both the electricity and the heat being useful products. Note that the power density is unaffected by the presence or absence of recirculation; the efficiency of the converter, however, is. One may view photon recirculation as offering the opportunity to use the same amount of fuel to heat the radiant surface to a higher temperature, or to use less fuel to heat the surface to the same temperature. As will be shown, photon recirculation is required for high overall system efficiencies, whether broad-band or selective radiators are used.

For a broad-band spectrum, the elementary modeling of the *p*/*n* converter, reviewed in the last section, showed that the ideal bandgap of the semiconductor (to a good approximation, irrespective of the radiator temperature) is likely to be about 0.4–0.6 eV, which corresponds to a wavelength of slightly more than 2.1 μm. The ideal optical device with which to achieve photon recirculation would therefore exhibit a sharp increase in reflectance from zero to unity at a wavelength of about 2.1 μm, as shown schematically in Fig. 42a. One may also consider filters that exhibit a transmittance pass-band spanning wavelengths just less than and just greater than the bandgap (Fig. 42b). In this way, high energy photons would also be reflected back to the radiator. Photons with energies much higher than the bandgap excite carriers high into the conduction band (assuming an *n*-type absorber), from which level they return to

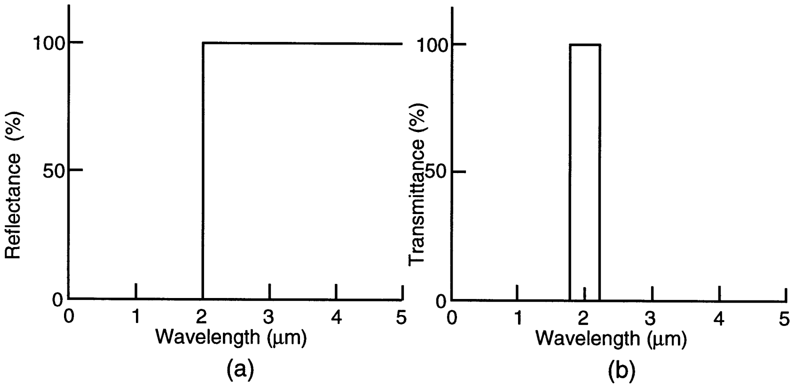

Fig. 42. (a) A modeled filter that transmits all radiation less than 2 μm wavelength and reflects all wavelengths greater than 2 μm back to the radiator. (b). A modeled filter that transmits only in a narrow band of wavelengths and reflects all other wavelengths.

equilibrium by thermalization. This heats the converter and causes a dramatic increase in the reverse saturation current, which reduces the output voltage severely. Band-pass filters based on dielectric stacks could remove this problem, although there are significant technical and economic difficulties in achieving this. As discussed in Section 3, most work on photon recirculation has concerned multi-layer filters based on dielectric stacks, plasma filters based on transparent conducting oxides (TCOs), resonant arrays (based on a pattern etched in a metallic thin film), and back-surface reflectors (based on the use of a specular back-surface metallic contact). We shall discuss each of these individually, although combinations of multi-layer and plasma filters have also been used successfully.

4.2. Dielectric thin-film stacks

Multi-layer stacks of thin-film dielectrics have been used to achieve a wide diversity of optical functions and have the attraction of being essentially non-absorbing, at least in the wavelength range of interest here. The technology is very well understood, and many complex products are commercially available. For a power-generating technology, there are, however, economic and technical problems. For the sake of illustration, and not implying that the approach used here is optimal or used by coating companies, we shall simply show that the necessary optical functions can be achieved and indicate the design complexity.

Various optical design software packages are available commercially, and we have chosen to use one of these (TFCalc^{TM}, supplied by Software Spectra of Portland, Oregon). For our purposes, it is sufficient to consider layers of two dielectrics: ZnS and MgF_2, with refractive indexes of approximately 2.4 and 1.4, respectively. To perform the modeling, it is necessary to know the refractive index and the extinction coefficient, as a function of wavelength, over the range covering the desired optical transition(s). This information is readily available for these materials [71, 72]. Figure

43 shows an example of a high-pass reflectance filter and Fig. 44 shows an example of a band-pass transmittance filter. Within the wavelength range considered, the performance is excellent, but this comes at a price. More than 70 layers of alternating high- and low-index films are required to achieve the performances of the filters shown. In addition, the thicknesses, porosity, indexes, and interfaces of all the films must be carefully controlled. For sophisticated optical applications, this is not only

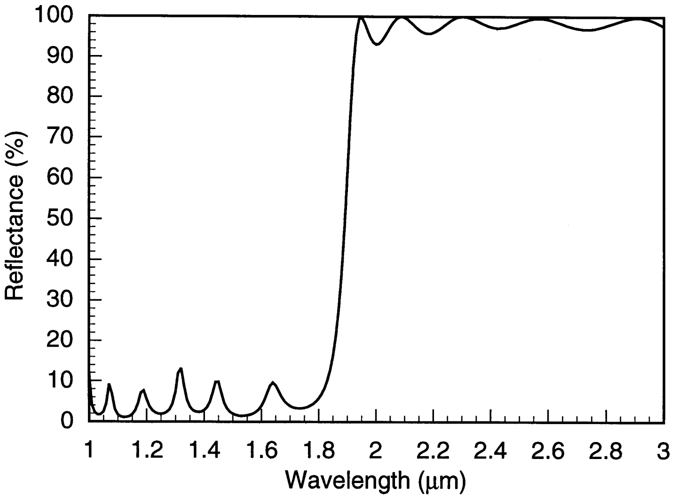

Fig. 43. Modeled reflectance of a designed multi-layer filter. Achieving this performance required more than 70 individual layers of MgF_2 and ZnS.

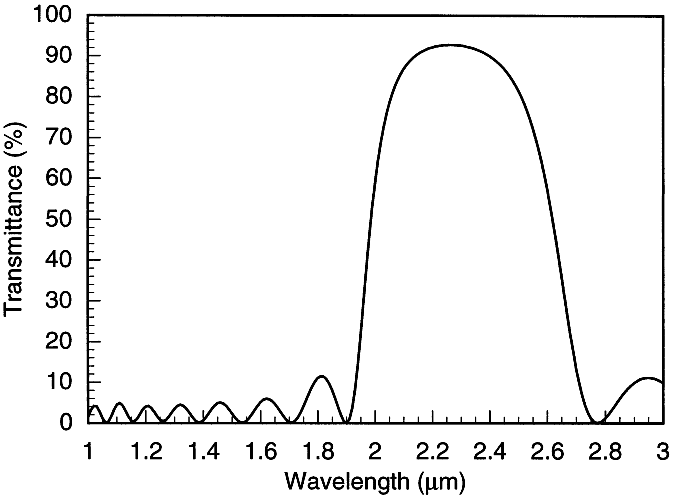

Fig. 44. Modeled transmittance of a designed band-pass filter. As with Fig. 42, more than 70 dielectric layers were required. Superior performance can be achieved with even more layers.

possible but is economically acceptable. However, for a large-area energy-generating technology, the cost is likely to be prohibitive.[7] The level of the control of the film thicknesses required is illustrated by Fig. 45. This shows the effects of allowing a variation of ±2% in the thickness of the layers on the performance of a band-pass filter. This plot was obtained by analyzing the stack one-hundred times with normally distributed random variations in the thickness of all the layers. The problem is worsened when one considers the more realistic variations that are likely to occur across large substrate areas. There is likely to be a significant variation in the angle of incidence of the radiation onto the optical filter from a large-area radiator. Figure 46 shows the effect of a relatively small variation on the band-pass filter. If one considered both thickness and angular variations, then the variation of performance would be much stronger.

Finally, Fig. 47 shows the variation of performance of the filter shown in Fig. 44, but across a wider range of wavelengths. This is specially noteworthy because the blackbody spectrum, at the radiator temperature of relevance to TPV, extends to at least 10 μm or more. Hence, the presence of side-bands, such as those evident in Fig. 47, is certain to be damaging to the system efficiency. With all these effects combined, it is simple to see that the use of multi-layer dielectric stacks to TPV conversion is questionable.

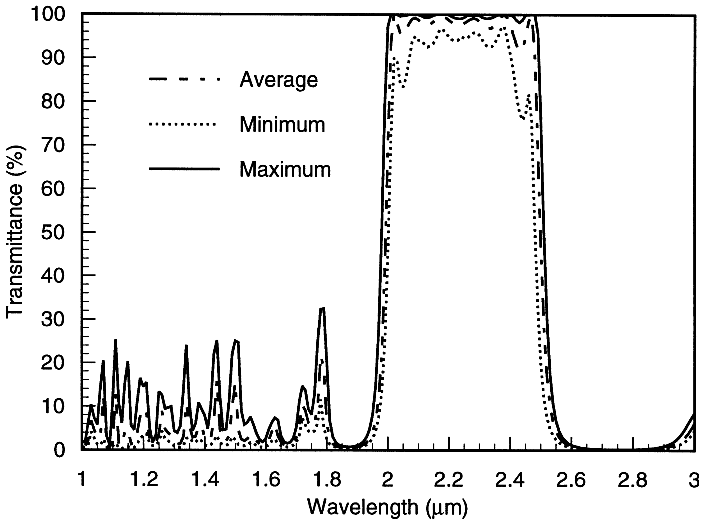

Fig. 45. Modeled performance of a band-pass filter with up to ±2% random uncertainty in the control of the thicknesses of the dielectric layers.

---

[7] In fairness, it should be admitted that this has not been established by discussion with relevant optical coating companies.

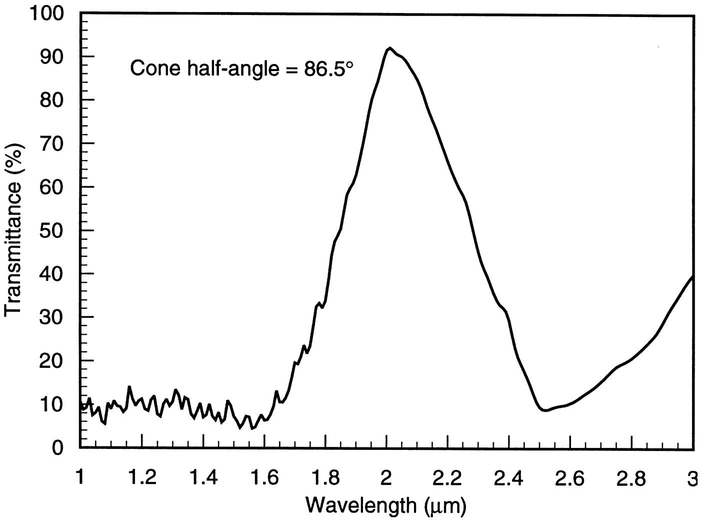

Fig. 46. Modeled effect of a variation in the angle of incidence on the performance of the filter shown in Fig. 44. Such variations would be expected across a large area.

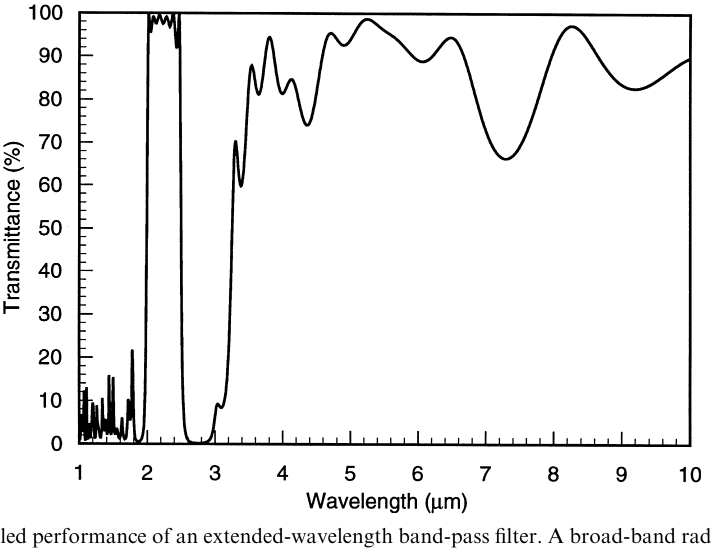

Fig. 47. Modeled performance of an extended-wavelength band-pass filter. A broad-band radiator still has 12% of its flux at 10 μm, and excellent reflectance to this wavelength would be required of a real filter.

4.3. Transparent conducting oxides

TCOs are an unusual class of materials in that they transmit light and conduct electricity relatively well. They do not transmit light as well as a dielectric does, but do so much better than a metal. Also, they do not conduct electricity as well as a metal does, but do so much better than a dielectric. They are wide-bandgap ($\gtrsim 3.2$ eV) semiconductors, which gives them their excellent optical transmittance, and they conduct by intrinsic defects and/or extrinsic impurities.

Materials belonging to the TCO family include indium oxide, tin oxide, indium tin oxide, zinc oxide, cadmium stannate, and many others presently under consideration [73]. TCOs are commonly used in flat-panel displays, architectural heat-reflecting coatings, photovoltaic panels, and many other large-volume applications. In recent years, there has been a systematic search for TCOs with improved properties, and some of this work has been relevant to TPV selective filters for photon recirculation.

The properties of TCOs can be remarkably well explained by the over-simplified Drude theory of free electrons. In this, the electrons are treated as simple harmonic oscillators: their vibration is driven by the electric-field component of the electromagnetic radiation (light). We shall outline the key steps in the development of the theory and relate their performance to the materials properties.

A full discussion of the following is given in Born and Wolf [74] and, as specifically applied to TCOs, in Coutts et al. [73] The model assumes that the carriers are forced harmonic oscillators that are damped by collisions. There is also, in general, a restoring force. The latter is usually neglected because the electrons are considered to be essentially free. Their equation of motion is:

$$m^*\ddot{\bar{x}} + \frac{m^*\dot{\bar{x}}}{\tau} = \bar{E}e. \tag{21}$$

The electric field is, of course, a vector, and it can be expressed by:

$$\bar{E} = \bar{E}_0 \exp - i\omega(t - x/\bar{v}(t)). \tag{22}$$

In these equations, m^* is the effective mass of the electrons (high-performance TCOs are always n-type), e is the electronic charge, ω is the angular frequency, τ is the relaxation time (i.e., the time between successive randomizing collisions of the electrons), t is time, and x is position. Solution of eqn (21), subject to the electric-field vector being given by eqn (22), leads to the time-dependent velocity, $\bar{v}(t)$. The current density is defined as:

$$J = ne\bar{v}(t), \tag{23}$$

and the a.c. conductivity (after some algebra) can be shown to be:

$$\sigma = \frac{\omega ne^2}{m^*}\left\{\frac{-i(\omega_0^2 - \omega^2) + \omega/\tau}{(\omega_0^2 - \omega^2)^2 + (\omega/\tau)^2}\right\}, \tag{24}$$

where n is the free-carrier concentration, and ω_0 is the natural frequency of the vibrating system. In addition to the above, Maxwell's equations lead to an expression for the complex dielectric permittivity:

$$\varepsilon^* = \varepsilon_\infty + \frac{\sigma}{\varepsilon_0\omega} i. \tag{25}$$

Substitution for the a.c. conductivity, which is a complex quantity, from eqn (24) gives the real and imaginary parts of the permittivity. From these, we may obtain the real and imaginary optical constants (the refractive index and the extinction coefficient). These quantities are both functions of the free-carrier density and the relaxation time, the latter being equivalent to the mobility. Thus, we may model the optical properties of a thin TCO film as a function of carrier concentration, mobility, effective mass, and permittivity to establish the critical parameters.

There are many assumptions in this approach, which are discussed more fully by Mulligan [75]. In particular, it is not necessarily correct to assume that the conductivity effective mass is the same as the density-of-states effective mass (obtained from transport measurements). Although they have been shown to be equal for cadmium stannate (the focus of Mulligan's work), within the limit of experimental accuracy, it is not, in general, correct. If the Drude approximation is valid, then it is possible to infer the effective mass and relaxation time from measurements of the transmittance and/or reflectance of a thin-film. However, very accurate measurements (better than about $\pm 0.5\%$) must be made to give any confidence in the data. Further detail is unwarranted here, but a full discussion is given by Coutts et al. [73].

Figure 48 shows the variation of modeled reflectance with wavelength, with the carrier concentration being treated parametrically. In this case, the mobility was taken as 50 cm^2 V^{-1} s^{-1} and the thickness as 0.5 μm. The effective mass was taken as $0.35m_e$, which is typical of other reports of TCOs [76]. The important feature is that the transition from high transmission to high reflectance occurs in the appropriate wavelength range for a carrier concentration of about 10^{20} cm^{-3}. The wavelength at which the transition occurs (the plasma wavelength) is relatively independent of the mobility, but the steepness of the transition is not. Figure 49 shows the modeled absorbance in a 0.5-μm-thick film for a carrier concentration of 10^{20} cm^{-3}, with the mobility being

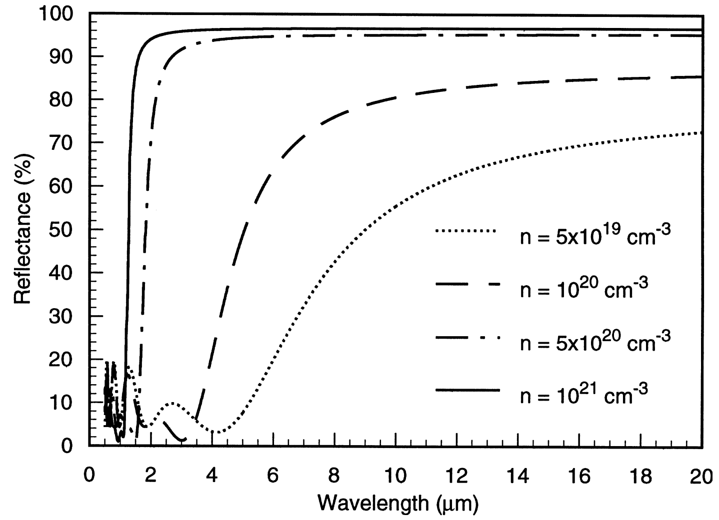

Fig. 48. Modeled variation of the reflectance of a plasma filter as a function of wavelength, with the carrier concentration being treated parametrically. The mobility was taken as 50 cm^2 V^{-1} s^{-1}.

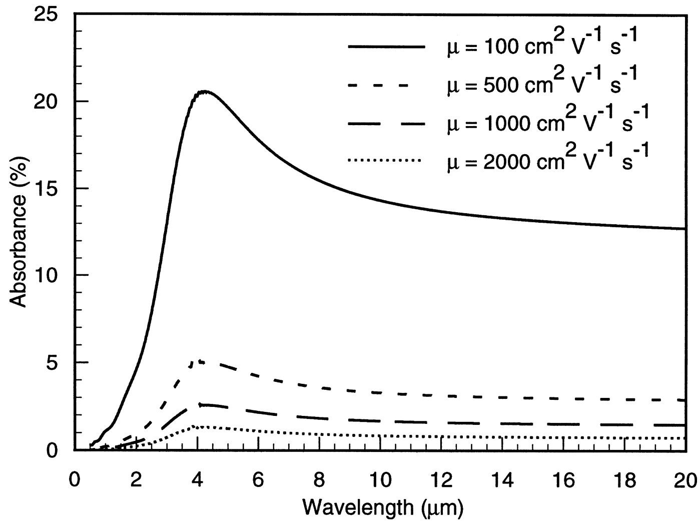

Fig. 49. Modeled variation of the absorbance of plasma filters as a function of wavelength, with the mobility being treated parametrically. The carrier concentration was 10^{20} cm^{-3}.

treated parametrically. The range of mobilities extends to an unrealistically high level for TCOs but not for single-crystal semiconductors, which is a point we shall return to below. The main point to note is that the free-carrier absorption occurs precisely where we wish to avoid losses. This is inevitable because the transition involves a resonance, rather than an interference, effect.

For the best-performing TCOs, the mobilities have reached 100 cm^2 V^{-1} [77], which is still too low to permit these materials to be used as single-element selective filters for photon recirculation. However, the combination of a plasma and an interference filter does seem to offer advantages. Whereas the latter exhibits side-bands at longer wavelengths, combining it with a plasma filter partially overcomes this. Nevertheless, the free-carrier absorption band of the plasma filter inevitably limits the performance of the combination filter.

The only possibility to use a plasma filter effectively may be to make the filter integral to the device structure and to make it from a high-mobility semiconductor such as InGaAs. *n*-type InGaAs retains a high mobility, even when it is very heavily doped, because the electrons are very light ($m^* \sim 0.05m_e$). The same comment could be made of InAs ($m^* \sim 0.01m_e$), although, in this case, a lattice-mismatch would need to be accommodated on typical low-bandgap materials such as GaSb and InGaAs. A layer of InGaAs doped to 10^{20} cm^{-3} could still have a mobility in excess of 1000 cm^2 V^{-1} s^{-1}, in which case its performance could be represented by the lowest absorption curve of Fig. 49. This high mobility is a possibility in such a heavily doped material because of the high crystalline perfection of the epitaxial material and that the effective mass is so low. The absorption would be significantly less than 10%, and the heavily doped integral filter would be simple to contact with metals, with an extremely low specific contact resistance. This concept is now being exploited in converter fabrication and has previously been discussed by Charache et al. [78].

4.4. Resonant antenna arrays

The functions of multi-layer band-pass filters can be made using resonant antenna arrays, originally developed for use with sub-millimeter waves [79, 80] and further developed by Horne et al. [81] for TPV conversion. The operation is based on a dense array of thin metal film antennae deposited on a dielectric substrate: the array consists of either metal crosses or of crosses etched in a metallic film. In fact, the array may be of many different possible configurations, but crosses appear to be used, presumably for ease of fabrication. An array of crosses etched in a continuous metal film behaves, electrically, like an inductive filter, whereas an array of metal crosses deposited on a dielectric substrate behave like a capacitive filter. The inductive array provides a band-pass function, whereas the capacitive array acts as a band-rejection filter. Currents are established by the interaction of the electromagnetic radiation with the antennae, and the array resonates when its dimensions are comparable with the wavelength of the radiation. The electric field at one side of the patterned feature will be different to that at the opposite side. In the inductive filter, this sets up oscillating currents in the metal film around the etched cross. This is why such a pattern behaves inductively. Recently, Ebbesen et al. [82] obtained interesting results for transmittance through gold films, a full explanation of which demanded a more sophisticated approach than that of an equivalent circuit. The magnitude of the transmittance is a function not only of the dimensions of the antennae, but also of their density on the substrate, the conductance of the metal film, and the dielectric and optical properties of the substrate. The dielectric substrate stores energy (analogous to a capacitor), whereas the metal film permits energy to circulate (analogous to an inductor). As Horne et al. [81] pointed out, changing the dielectric properties of the substrate is analogous to changing the spring constant of a mechanical vibrating system and, as such, it also changes the resonant wavelength, which is given by:

$$\lambda = 2L[(n_1^2+n_2^2)/2]^{/2}, \tag{26}$$

where n_1 and n_2 are the reactive indexes of the media above and below the metal film (i.e., air and the substrate) and L is the length of the antennae ‘arms’. The array is designed to be used with a semiconductor of 0.6 eV bandgap, corresponding to an optimum wavelength of about 2 μm. If we take the substrate index as glass with $n_2 = 1.5$ and the surrounding medium as air, then the dimension (i.e., the length of the arms of the etched areas) of the antenna must be on the order of 1 μm. However, their width must obviously be much less than this, which may present a problem in large-volume production.

The antennae array may be treated using an equivalent circuit consisting of a resistor, connected in series with a parallel coupled inductor, and capacitor. Although this is a gross approximation, it enables us to grasp the magnitude of the individual components. In reality, the orientation of the electric-field vector of the radiation to the arms of the crosses, their mutual inductance and capacitance, and the self-inductance of the metal film are all complicating factors, ignored in the approach described here. The subject was discussed by, for example, Whitbourn et al. [83], who showed that the transmittance of the inductive array is given by:

$$T = \frac{4n_1 n_2[(R_0/Z_s)^2 + (X/Z_s)^2]}{[1+(n_2+n_1)R_0/Z_s]^2 + (n_2+n_1)^2(X/Z_s)^2}, \tag{27}$$

where R_0 is the sheet resistance of the metal film, Z_s is the impedance of free space, and X is the reactance of the mesh. For an inductive mesh, the reactance, X_1, is given by:

$$\frac{X_l}{Z_s} = -\left(\omega_0' \log \csc\left(\frac{\pi a}{g}\right)\right)\left(\frac{\omega_0}{\omega_0'} - \frac{\omega_0}{\omega}\right)^{-1}, \tag{28}$$

where g is the periodicity of the mesh, and a is twice the size of the mesh features. ω_0' is given by:

$$\omega_0' = \omega_0\sqrt{\frac{2}{n_1^2+n_2^2}}, \tag{29}$$

with ω_0 being the resonant frequency of the mesh in free space (i.e., without a substrate). The frequencies in these formulae have been normalized by putting:

$$\omega = g/\lambda, \tag{30}$$

so that eqn (28) is dimensionless. Hence, we see that the inductance and capacitance are likely to be on the order of 10^{-14} henrys and 10^{-17} farads, respectively, for a dimension of about 1 μm. As mentioned above, this places the resonance at about 2 μm. Figure 50 shows the response of a resonant array filter with $L = 5 \times 10^{-18}$ henrys, $C = 2.5 \times 10^{-13}$ farads, and $R_0 = 0.2\ \Omega/\square$.

Originally, the dense arrays were made by direct-write electron-beam lithography (DEBL). However, this was very time-consuming and expensive. More recently, the arrays have been made using a silicon stencil, fabricated using masked ion-beam lithography (MIBL). The stencil may be used many times as a mask over a gold film in which the array of micron-sized antennae is etched using a proton beam. With this approach, it is claimed that the arrays can be made for less than \$1 cm^{-2}. Typical transmittance characteristics are shown in Fig. 50. The key point to note is that the modeled performance is essentially as good as that of the multi-layer stack, band-pass filter, shown in Fig. 42b. So far as the author is aware, a comparative economic study has not been conducted. Representatives of EDTEK, Inc., are confident that economically viable production will not be a major issue, and prototype systems are under development. In terms of performance, one supposes that the output energy density must be significantly less than that of systems based on back-surface reflection (to be discussed next) because higher-than-bandgap photons are reflected to the radiator. To compensate this, there will be much less heating due to thermalization of minority charge that has been excited to high energy levels. Data on the power

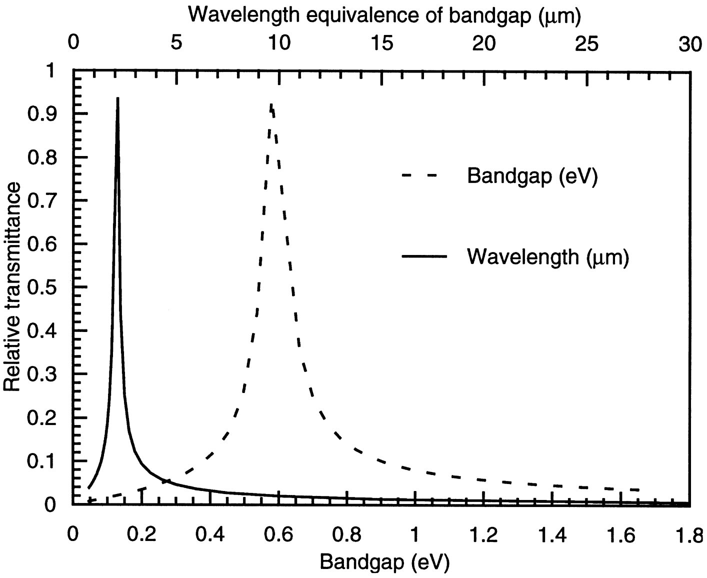

Fig. 50. Modeled performance of a resonant array filter. The characteristic dimension of the array metallization is on the order of 1 μm. The equivalent inductance and capacitance are given in the text.

density from TPV arrays with resonant array antennae do not appear to have been published.

4.5. Back-surface reflection

The most successful design developed to date uses a concept known as back-surface reflection (BSR). This was discussed in greater detail by Ward et al. [70] in the last section. The principle is that the sub-bandgap photons pass through the device layers with only minimal absorption, through the substrate to the back contact, by which they are reflected back along the same path to the radiator. A typical structure might consist of an InGaAs device, with a bandgap of about 0.6 eV, grown mismatched on an InP substrate. If the latter is relatively lightly doped, then free-carrier absorption is minimal. However, making an ohmic contact to a lightly doped substrate is generally difficult. This can be overcome by incorporating a very thin, heavily doped contacting layer. If the effective mass of the carriers in the substrate is known, both optical and electrical loss processes may be modeled, and the ideal doping level in the substrate may be calculated. The issue of forming low-resistance ohmic contacts is vital because the devices generate a large current density, and Joule losses could easily be excessive if the substrate is too lightly doped. On the other hand, the interdigitated contacts on the front of the device remove the need for the substrate to be electrically contacted at all.

Borrego et al. [84] pointed out that to use BSRs, several criteria must be met by the metal/semiconductor pair. These include:

(i) A highly reflective interface.
(ii) Minimal free-carrier absorption.
(iii) A low specific contact resistance.
(iv) Good adhesion.
(v) Good stability both chemically and thermally.

There are several contributions to the electrical losses: the spreading resistance in the *p*-type emitter, the bulk resistance of the substrate, and the back-surface contact resistance. For the substrates considered, the substrate contribution was negligible. It was also stated that the specific contact resistance must be less than $5 \times 10^{-5}\ \Omega\ \mathrm{cm}^2$. This was achieved for the three substates considered. The spreading resistance of the *p*-type emitter is a function of the carrier concentration and mobility and of the thickness of the emitter. If the thickness is large, the electrical problem is less severe, but excess carriers generated in the emitter are probably not collected because of heavy doping, which leads to a short minority-carrier lifetime. The model suggested that the contribution to the series resistance from this source could be kept below 2 mΩ for an emitter thickness of greater than about 0.2 μm, and a carrier concentration of $5 \times 10^{18}\ \mathrm{cm}^{-3}$. No indication of the optical losses in the emitter were given.

In the sub-bandgap range of wavelengths, the free-carrier absorption coefficient in GaSb substrates was found to obey the empirical relationship:

$$\alpha = 6 \times 10^{-17} n, \tag{31}$$

where n is the electron concentration. This relationship applies to *n*-type GaSb. For *p*-type material, the holes are relatively heavy and the free-carrier absorption is much larger. Borrego et al. [84] plotted the total free-carrier absorption loss in the substrate vs the product of the electron concentration and the thickness, and showed that this quantity must be less than $10^{15}\ \mathrm{cm}^{-2}$ for the loss to be less than 5%. The reflectance at the metal/semiconductor interface is a function of materials and fabrication issues. For GaSb, InAs, and InP substrates, the reflectance was in excess of 90% near the bandgap of the semiconductor, but decreased significantly at longer wavelengths. This is due to the increasing absorption by free carriers in this range of wavelengths. The long-wavelength tail of the blackbody spectrum extends to at least 10 μm, and the decrease in reflectance is a disadvantage.

It is important to ensure that the interface remains specular to obtain maximum reflectance. Unfortunately, formation of ohmic contacts (particularly to lightly doped material) generally requires alloying the metal and the semiconductor, which leads to a rough interface. Sn : Au was used to make contact to *n*-InP and *n*-GaSb, whereas Ti : Au was used with *n*-InAs. The group IV component in the contacting metal establishes an n^+-layer at the surface, thus narrowing the width of the potential barrier to tunneling electrons. Sn is often used for this purpose with *n*-type III–V semiconductors, but unfortunately it does not have a high reflectance. Consequently, novel schemes were developed to minimize the adverse optical effects of alloying and yet not compromise the contact resistance excessively.

With *n*-InAs, the problem is trivial because the Fermi level is pinned in the conduction band by surface band-bending effects. This is equivalent to a heavily doped layer at the surface. Consequently, most metals would form an adequate contact to *n*-InAs; Ti : Au was chosen by Borrego et al. [84] for InP and GaSb, the approach was to form alloyed regions (grids) occupying a small fraction of the semiconductor surface. The remaining area was covered with highly reflective, non-alloyed material. If the specific contact resistance is $5 \times 10^{-5}\ \Omega\ \text{cm}^2$, a 5% grid coverage would give a contribution to the series resistance of 1 mΩ. This is low enough not to impede device performance. A scheme involving Si_3N_4 dielectric spacers was used to avoid long-term reactions between the metal and the semiconductor.

As discussed earlier, Ward et al. [70] overcame some of the problems in photon recirculation by using a novel scheme that involved forming both contacts to the device on the front surface of the substrate. This permits the use of a semi-insulating (SI) substrate. The structure was developed for matched or mismatched InGaAs on an SI InP substrate, and it was discussed in much greater detail in Section 3. The importance in this section is that it was possible to form very high-quality optical layers on the back of the substrate. The substrates were first polished to a specular finish, and then a film of gold was deposited. The total thickness of the heavily doped device layers was only about 10 μm, and free-carrier absorption was minimal in them. In the substrate it was essentially nonexistent! The reflectance at wavelengths longer than that corresponding to the bandgap was greater than 90%, although it did decrease slightly with increasing wavelength due to free-carrier absorption in the active layers. Typical data are shown in Fig. 51, indicating that the reflectance remains high in the entire wavelength range of relevance, i.e., 3–10 μm. This is the most

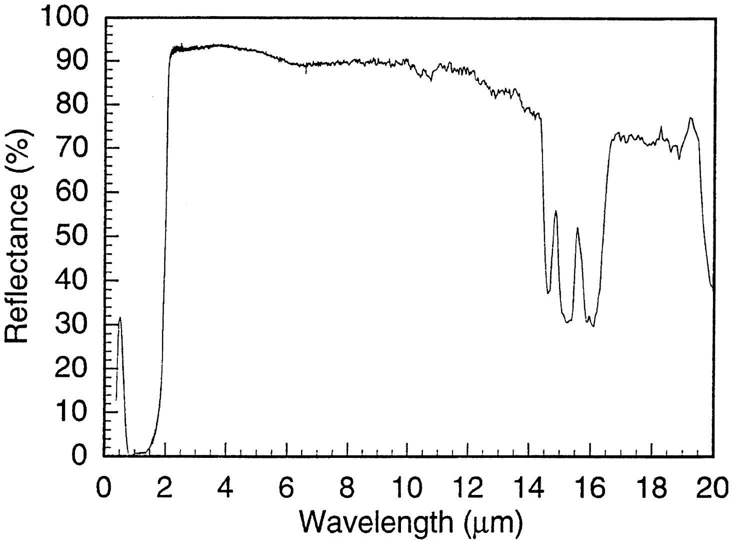

Fig. 51. Reflectance from an MIM structure. The reflectance in the sub-bandgap region of the infrared spectrum is greater than 98%.

successful approach to the recirculation of sub-bandgap photons, and it was the highest-performing device tested to date [85].

4.6. Summary

Although there are several potential approaches to recirculating the sub-bandgap photons, there are several disadvantages with all of them except for the back-surface reflector technique. Dielectric stacks require complicated control over thickness as well as over the properties of the materials and interfaces throughout the thickness of the stack. Over a wider range of wavelengths, as required for a broad-band radiator-based converter, the performance deteriorates severely. The sheer number of layers required will probably render this approach unacceptably expensive.

Plasma filters are promising but exhibit an inevitable absorbance band precisely in the part of the spectrum where minimal absorbance is required. Unless the mobility of these materials can be raised to much higher levels, then this will always be the case. Semiconductor integral filters appear to be very promising and are compatible with the method of growth used for the active layers of the device. In low-bandgap materials, such as InGaAs, the mobility can be exceptionally high, even for very heavy doping. With this approach, much of the sub-bandgap radiation would not be permitted to pass into the device and substrate, and free-carrier absorbance would therefore be minimal. Combining the front-surface integral filter with a back-surface reflector seems to be ideal because it is compatible with existing manufacturing methods, does not require complicated additional production steps, and is technologically promising.

5. Modeling, conceptual designs, and demonstration of TPV systems

5.1. Introduction

In this section, we shall discuss the modeling of complete systems. This will incorporate input from Sections 3 and 4 that dealt with performance of the converter and the means of photon recirculation. We shall also discuss several interesting conceptual designs based on a variety of fuel sources. There are very few systems with performance that have been validated under standard characterization conditions (which is one of the weaknesses of existing programs), but we shall comment on a sample of those that have been reduced to practice.

The conceptual designs include many different types of fuel, including (for example) nuclear radiation [86, 87], solar [88–90], biofuels (wood-powder) [1], natural gas [91], kerosene [92], the military fuel JP-8 [93], and others. The designs reflect the wide range of combinations of components and include multi-layer dielectric filters [94], resonant antenna arrays [89] and plasma filters [73], as well as both broad-band [95] and selective radiators [32, 35], narrow-bandgap converters [55, 96, 37, 97], and conventional silicon solar cells [23]. The range of applications considered is equally diverse. Most of the designs were developed in the last few years, although at least one was developed and demonstrated many years ago [22]. In this section, a small selection of some of the designs, models, and actual system demonstrations will be reviewed. The reviews in this section are based almost exclusively on the proceedings of the NREL TPV Conferences and, in particular, the Third Conference [5].

5.2. Modeling of TPV system performance

Since TPV was first conceived in the 1960s, many efforts have been made to model the performance of discrete TPV semiconductor converters, with much less effort having been devoted to modeling complete systems. The papers reviewed in this section all deal specifically with complete systems and take into account non-ideal performance of individual components. Most modeling has tended to assume ideal performance of the individual components, whereas in actual systems there are certain to be additional losses that are more difficult to take into account in analytical models. As discussed earlier, there are, for example, angle-of-incidence effects that make the performance of the optical system used for the recuperation of sub-bandgap photons non-optimal because they are designed for normal incidence, whereas, in reality, there must be a wide spread of angles of incidence. In fact, the larger the areas of the radiator and cells, the more this must be the case. If we regard the radiator/converter pair as an optical cavity, then there will also be loss of convertible photons from the edges of the cavity. Until recently, none of these had been taken into account in any system modeling.

Ballinger [98] discussed a powerful development in the statistical modeling of a TPV system. This work was also presented [40] at the Third NREL TPV Conference. The approach overcame a number of the historic limitations mentioned above.

The model used a Monte Carlo approach to simulate the history of millions of photons emitted by the radiator, finally to be absorbed by the TPV array or elsewhere in the cavity. The latter consisted of a radiator that was parallel to the TPV array, the cavity being completed by vertical, reflecting walls. Although the program was named RACER-X (presumably a contraction of ‘ray tracer’), it was the paths of photons that were considered. The key difference between this and other approaches to modeling systems was the recognition and incorporation of a temperature gradient across the surface of the radiator. The temperature profile was assumed to be parabolic, although at the time of this paper, this had not been confirmed. The program sampled the emission of photons from the radiator, and the properties sampled included their number, position, energy, state of polarization, and direction of emission. Because of the temperature gradient, it was necessary to restrict sampling of each of these quantities to a specific probability distribution to avoid violating Planckian considerations of numbers and energies.

The code provided an output of the fraction of photons that would be absorbed or not absorbed (energies greater or less than the bandgap) by the array. This was converted to an absolute heat flux by multiplying by the total numbers of photons, or the total energy radiated. The radiated heat flux was determined by the parabolic temperature profile. This was determined by the difference between the temperatures at the center and the corner of the array, and by the distance between these two extremes. For a square radiator, the heat flux, as a function of position, was obtained in a reasonably tractable form involving the temperature extremes and the size of the array.

The point of emission on the radiator was sampled according to a probability distribution of the numbers of radiated photons. This, again, was dictated by the position-dependent temperature. The determination was done by generating two random numbers. The first of these was multiplied by the distance from the center to the corner of the array. The second was used to establish whether or not this position actually lay on the surface of the radiator (the diagonal of the square radiator is larger than any other dimension of the array, and the location could be outside the boundary of the radiator). Having generated the birth-point of the photon as a distance from the center of the radiator, this was converted to (x, y) coordinates after multiplying by a third random number, an angle, between 0–2π. Having determined the birth-point, it was then straightforward to calculate the energy distribution of the photons radiated at that point.

The direction of emission of the photons depended on the nature of the radiator. It was assumed that the surface was diffuse and followed a Lambertian probability, i.e., a cosine distribution. The 'scattering angle' was defined as the angle of emission with respect to the vertical normal and the sampled directions were sampled according to the cosine distribution. The 'azimuthal angle' was defined as a direction in the plane of the radiator in which the photon was emitted. These two angles completely specified the direction of emission of individual photons and, therefore, the angle at which they were incident on the array. In the publication by Gethers et al. [40], the state of polarization was also taken into account, and it was also generated statistically. The energy, angle of incidence, and state of polarization of photons affects their reflectance at the various internal surfaces of the cavity.

The surfaces of the TPV cells were typically covered by grid lines to collect the photo-generated current, and by a filter used to reflect sub-bandgap photons back to the radiator. It was assumed that the grid lines were optically specular and occupied 10% of the array surface. On the other hand, the reflectance of the filter was computed using a separate code package named OptiLayer. The external quantum efficiencies (QEs) of individual cells were stored as library files and converted into internal QEs using the filter reflectance and the grid losses. This was done for the entire 4 × 4 array of cells used in the cavity experiments. Ideally, the QEs of all cells should be identical, but this was not the case in the set used in the experiment. Each time a photon of particular energy is absorbed by part of the TPV array, the equivalent QE for that energy was read. This was done for all photons and for all their properties mentioned above. The product of QE, the number of absorbed photons, and the electronic charge then gave the current produced by that particular cell in the array.

For simple infinite parallel-plate geometry, the heat flux could be calculated analytically and used as a test of RACER-X. The agreement was better than 3% for various radiator temperatures and cell reflectances. Comparisons were also made between the heat fluxes calculated for the 4 × 4 array of mismatched InGaAs cells ($E_g = 0.55$ eV) and those measured using calorimetry. The cells were 1 × 1 cm. This was done for multi-layer dielectric filters and for the tandem filters (dielectric stack/TCO combination) described in Section 4. A leakage path, between the array and the vertical walls, out of the cavity was also unavoidable. This permitted photons to escape, rather than being trapped indefinitely until absorption. In discussion, this emerged as a surprisingly important feature of cavity design. Table 4 shows the comparison between the measured and modeled heat fluxes for the two types of filter.

As can be seen, the differences were substantial and were cause for further investigation. Similar magnitude differences were also found for sand-blasted Al, a GaSb wafer of the same size as the array, and for a near-blackbody graphite plate. Modeling of the effect of arrays with and without grid lines showed that the latter reduced the modeled heat flux by 10%, in exact correspondence with their proportional area.

A series of sensitivity experiments was performed to assess the influence of the temperature profile across the radiator, the filter reflectance, and the reflectance of the vertical side walls of the cavity. A temperature difference between the measured and modeled heat flux of about 6.5% was found. This, however, probably underestimated the effect on the array of cells. Because of the different intensities on center and edge cells, they would generate different currents, which would lead to circulating currents and a decrease in array performance. The effect on voltage and fill factor was also neglected. The reflectance of the filter was modeled as a function of photon energy, angle of incidence, and state of polarization. The treatment included three permutations: the first variable alone; the first and second variables; and the first, second, and third variables. The angle reduced the modeled heat flux by only 2.5%. The inclusion of polarization, surprisingly, appeared to have no effect, at least to the first decimal place.

The effect of the reflectance of the vertical side walls of the cavity was also modeled by considering a spectral utilization factor (SUF). This was defined as the ratio of the useful radiation absorbed ($h\nu > E_g$) to the total energy absorbed by the array. The model revealed a large decrease in the SUF for modeled systems with and without a photon leakage path. The magnitude increased as the reflectance increased and, for a reflectance of 100%, the SUFs were about 70 and 45%, respectively. A leakage path of only 2 mils (~ 26 μm) in width was assumed. Clearly, the width of the leakage path must be minimized in practical systems. The magnitude of the effect is not intuitively to be expected, but can perhaps be understood by considering the multiple reflections

Table 4
Measured and modeled heat fluxes on a 4 × 4 array of cells. The first line shows the result for the single surface filter; the second shows the result for the tandem filter [98]

Center temperature (°F)	Edge temperature (°F)	Radiator heat flux (W cm^{-2})	RACER-X heat flux (W cm^{-2})	Measured heat flux (W cm^{-2})	% difference
22071	1957	18.67	5.345	7.66	30
2230	2130	25.42	5.246	7.7	32

of photons within the cavity. A photon will continue being reflected until it is absorbed. This may be by the radiator (ideally only sub-bandgap photons), by the array (ideally only above-bandgap photons), by some other surface of the system, or until it escapes through the gap.

In the paper by Gethers et al. [40], estimates were made of the efficiency of the array. Under the best circumstances, the efficiency was 13.2%. As with other modeled efficiencies, this is rather modest, but is probably realistic. It should also be noted that this does not include the combustion efficiency. However, the efficiency of the cells, the radiator, and the filter were included.

The properties and performance of the filter were modeled using the OptiLayer code. This included all three of these variables. This is a potential weakness of the work, because the actual and predicted performance of a filter are often significantly different due to non-ideal performance of the films comprising the filter, lack of control over the thicknesses of the films, and non-specular interfaces. A superior approach would be to measure the performance of a real filter over a wide range of photon energies and angles of incidence, and then to use these measurements as library files to be called, as required, by RACER-X.

In a recent communication by Ballinger [99], it was stated that the disagreements outlined above have been removed. As mentioned, preliminary heat-flux calculations for the 4 × 4 array of cells were substantially different than measured results. This prompted a series of tests designed to isolate the problem, which turned out to be a combination of poor temperature characterization of the radiator and a shortcoming in the Monte Carlo code. This series of diagnostic tests proved to be extremely valuable in advancing the understanding of cavity photonics. The tests used the aforementioned cavity with different sizes of square silicon targets. The leakage path out of the cavity was reduced as much as possible, while retaining thermal isolation between the top and bottom plates, and the cavity walls were coated with gold to increase reflectivity. The objective was to force the closed cavity to behave as if it were in an infinite parallel-plate geometry. Excellent agreement was achieved between the experiment and calculated results. Another set of tests was initiated to reduce the uncertainty in the measured heat flux. A copper pedestal (block) was thermally mounted to the back of the target material: a 2 × 2 array of 0.55 eV InGaAs cells. Thermocouples were placed at different locations separated by known linear distances along the axis of the copper block. The measured temperature difference and the known thermal conductivity of the copper were then used to calculate the heat absorbed in the target TPV cells. The cells were surrounded by a shield to eliminate direct heating of the copper block by radiant energy from the radiator. However, this shield was thermally isolated from the target/copper block by a gap so that a true measurement could be obtained for the heat absorbed in the target. This gap proved to be an important factor in the absorbed heat flux. The analytic predictions, which could only model parallel plates without a gap, are significantly lower than the measured heat fluxes. The Monte Carlo calculations, however, were in good agreement with the measured heat fluxes. Furthermore, RACER-X was used to determine the heat-flux sensitivity to gap spacing for a radiator temperature of 2000°F ($\sim$1100°C). The 'offsets' refer to the vertical displacement between the top of the TPV target and the top of the shield material. Surprisingly, the absorbed heat flux is predicted to increase by 0.3 W per mil of gap spacing, which is a useful result when setting up an experiment. Recently, the RACER-X code has been modified to support analysis of back-surface reflectors, so refraction and explicit absorption have been added to the code.

Schroeder et al. [100] also developed a sophisticated model based on ray-tracing and the calculation of view-factors based on the system geometry. Both flat-plate and cylindrical configurations were used, and the model can consider both infinite and finite arrays. The authors pointed out that most research in TPV has been conducted on specific components, and this has led to system configurations that depend on the components of interest to the particular researchers. Inevitably, the performance of individual components may be degraded in an actual system. The code could accept both system design and geometry as inputs. A database of fuels and their heat contents was also built into the program. Additional codes allowed users to compare and optimize various system configurations.

Previous estimates of the incident energy on the PV cells were generally too optimistic because they neglected losses of thermal radiation within the system. In a sense, they were more like infinite parallel-plate systems. In reality, multiple reflections of photons must occur, leading to parasitic absorptions, causing only a fraction of the emitted radiation actually to be incident on the PV cells. If reflectors are incorporated in this system, then this can increase the incident fraction and the effective view-factor. The model assumed that the radiator was diffuse and uniform in its radiative properties although, as has been discussed already, a finite temperature distribution across the surface of the radiator is almost inevitable.

The model involved defining:

1. The energy fraction reabsorbed by the radiator.
2. The energy fraction radiated by the radiator.
3. The energy fraction absorbed in the filter.
4. The energy fraction incident on the cell.

These were expressed in terms of the view-factors, the materials properties, and total incident power. These quantities were all assumed to be wavelength-dependent, and it was therefore necessary to integrate over all wavelengths to obtain the totals for each term. A cavity transfer coefficient was used to define the fraction of power incident on the cell relative to the total radiator power. A recovery factor was used as a multiplier to allow for re-absorption of energy by the radiator. The user may define the cell temperature, but it can also be calculated from the balance of power incident on the cell, the electrical power output, and a loss term used to allow for radiated or convected power. The cell temperature was used to calculate the open-circuit voltage and fill factor, although no allowance was made for the temperature dependence of the short-circuit current density. This latter calculation gave the efficiency of the PV cell, which was defined as the electrical power output divided by the incident optical power. The radiant transfer efficiency was defined as the electrical power output divided by the total power radiated.

The heat-source model considered the amount of heat available from a recuperative burner, which depends on the enthalpies of the various states of the system, including the inlet, air preheat, combustion, energy extraction, and exhaust ambient states. The heat-source model was incorporated as a subroutine of the entire code. One the temperature and enthalpy of the six states were defined, the energy available for radiation could be calculated to obtain the efficiency of the heat source as the ratio of the maximum available heat at the radiation temperature to the heat content of the fuel.

These individual efficiencies, when multiplied together, give the overall system efficiency. If the geometry is treated as infinite plates with a blackbody radiator at a temperature of 1800°C, GaSb cells, at a temperature of 25°C, then the system efficiencies were about 16.2% with power densities of 15.2 and 14.2 W cm^{-2} output for systems with and without recuperative filters, respectively. With a finite geometry (i.e., 5 × 5 cm plates) and a non-ideal fuel source, the efficiency decreased to about 0.2% and the power-density output to 1.9 W cm^{-2}. However, when reflectors were included in the model to prevent, or lessen, parasitic absorptions inside the system, then the efficiency increased to 5.4% and the power-density output to 43.7 W cm^{-2}. However, at this level, the incident photon flux on the cells would be extremely intense, and it would be necessary to remove a substantial amount of heat from the cells to maintain their temperature at 25°C.

Thus, this model allowed for a number of practical considerations, which more idealized models have neglected. It also permits an iterative procedure to be performed to calculate the optimum system design for specific geometries, materials, and operating conditions. Note that the system efficiencies were predicted to be rather modest.

Other authors performed modeling of conceptual systems and derived similar results to those described above. It is important to remember that the overall efficiency of a TPV system is the product of the efficiencies of five individual components in the system. Even if each of these was 90%, the system would have an efficiency of 54% (0.9^5). With more realistic component efficiencies, the system efficiency will necessarily be lower. Realistically, the maximum system efficiency for a system based on abroad-band radiator is 20%. Even this would take a sustained program of research and development. For a selective radiator, the efficiency could be higher, but the power density, unless the radiation characteristics were nearly ideal, would inevitably be lower. If the equipment were used as a cogenerator and the waste heat regarded as a primary product, then the system efficiency would be much higher. However, most applications of TPV systems seem likely to be for electricity generation, in which case recovery of waste heat is necessary and limits system efficiency.

5.3. Conceptual and demonstrated TPV systems

In this section, we shall consider several system designs. Some are only concepts but appear to have promise of being able to be put to practice. Others have been reduced to practice, at least to some level of sophistication. The proceedings of the three NREL conferences contain many more examples of systems developments, but it is hoped that those reviewed here are adequately representative.

5.3.1. Solar TPV

Stone et al. [101] developed a conceptual design of a solar-powered TPV system using the power-tower concept, developed in conjunction with solar-thermal power generation. The original work concerned the development of a central receiver system, funded by the U.S. Department of Energy, to power a 25-kW Stirling engine. The TPV cells were provided by Amonix, Inc., by the NASA Lewis Research Center and by the National Renewable Energy Laboratory. These were, respectively, high-efficiency silicon, lattice-matched $In_{0.53}Ga_{0.47}As$ and lattice-mismatched InGaAs. The bandgaps of the two latter types were 0.73 eV and approximately 0.58 eV, respectively. A schematic of the generation system is shown in Fig. 52, which illustrates the dish concentrator system and the power conversion unit (PCU).

In its original form, the power conditioning unit would have been the Stirling engine. On the right-hand-side of the schematic is the intended TPV power-conversion system. At the right-hand-side of the system, there is a non-imaging parabolic concentrator, which has the benefit of increasing the solar concentration ratio and reducing the optical demands on the primary concentrator system. The primary mirrors and the parabolic concentrator together could produce a concentration ratio in the range of 15,000–20,000 times. The receiver surface was hemispherical, so as to distribute the flux more uniformly to the storage medium behind it. Silicon was considered an attractive storage medium because of its physical properties. It has a melting point of 1608 K and a large heat of fusion. The melting point is high enough to satisfy the demands of many conceptual TPV systems. The large heat of fusion means that a relatively large quantity of heat may be stored and available for eventual radiation to the TPV semiconductor cells. Fifty kilowatt-hours of electrical energy could be stored by only 285 kg of silicon if the TPV array were 35% efficient. Shutters

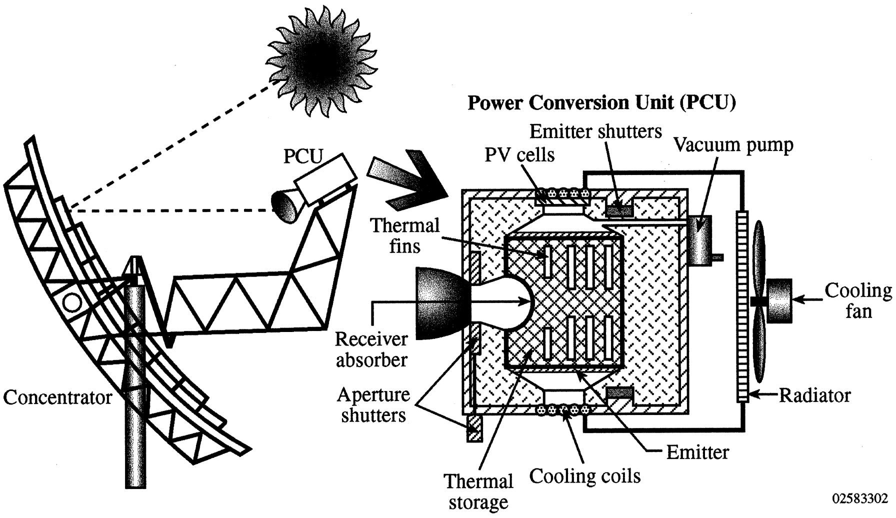

Fig. 52. Schematic of the solar-powered TPV system visualized by Stone et al. Reproduced by permission of the American Institute of Physics, and the author(s) [101].

were provided at the entrance to the cavity and immediately in front of the TPV cells (to be used eventually). The former would prevent loss of stored heat by radiation and convection, in the absence of any solar flux. The latter would have infrared reflectors on their inner surface to prevent the cells from overheating when the system is not being used. In a final system, the cells would be force-cooled, and the waste heat from the coolant would be discharged to the atmosphere. In a solar-powered TPV system, this is justifiable, because the fuel can be regarded as 'free'.

Tests were performed on erbium-doped yttrium aluminum garnet (YAG) and on silicon carbide. The former is highly selective, whereas the latter is broad-band with a high emissivity. The flux uniformity on both types of radiator was assessed, and the temperature distribution was measured. The flux was varied by adjusting the number of covered and uncovered mirrors in the primary concentrator. For example, in one test, it was found that the mean temperature of the radiator was about 100°C lower than that at the center. The temperatures were measured on the side on which the flux was incident, so the results imply that the temperature on the radiating side would probably have been about 200°C less than this. The temperature distribution across the radiant surface was less than 140°C, but this could have had a significant effect on the overall performance of the array. The flux incident on any point of the array is the sum of all the fluxes from all points on the radiant surface, taking into account all the factors considered by Gethers et al. [40]. With the broad-band system, this could have the effect of broadening the wavelength range of the radiator and would invalidate efficiency predictions. With the selective Y : YAG radiator, the effect might not be so significant, but would imply a reduced flux on the cells near the edges of the array. In turn, this could cause different outputs from individual cells, resulting in circulating currents and a considerable loss of performance. The maximum temperature of the radiator was 1350°C, and the radiators were generally stable, although some degradation was observed on one occasion. More than 300 h of on-sun testing was obtained.

Preliminary testing of cells was performed on a second test-bed, and their performance was found to be comparatively modest. With solar-powered TPV, one may ask, 'why is the sunlight itself not used?' Absorption onto a radiator and then re-radiating has the effect of decreasing the quality of the radiation by reducing its temperature and increasing the entropy of the system. If a similar concentration ratio were used on high-efficiency solar cells, the power-density output would be much greater. On the other hand, the TPV-based system would permit use during the night.

5.3.2. Biofueled TPV

Broman et al. [1] have argued that Sweden has an abundance of trees, despite the fact that the country has an annual tree-harvesting program. Many quads of excess energy are grown in the form of trees each year, and the authors proposed that the wood could provide the fuel for TPV systems. The key to the technique was to reduce the wood to very finely divided powder and then to burn this in a controlled manner. Provided that a sufficiently high temperature can be achieved, this could be the basis of a 'free-energy' TPV system. Naturally, it would still be important to obtain a sufficiently high temperature, although the level at which NO_x would be produced must not be exceeded. Temperatures of about 1300 K were achieved. The authors proposed using selective filters to recirculate the longwave, sub-bandgap photons.

5.3.3. Nuclear-fueled TPV

Schock et al. [102] developed a design for a TPV system fueled by a radioisotope general-purpose heat source (GPHS). This was designed for a space mission to Pluto, in the vicinity of which there is too little solar insolation to permit solar cells to be used. The GPHS has been flown in space previously and is safety qualified. The system was designed for use with GaSb cells and spectrally selective filters.

The GPHS has a maximum thermal power of 250 W and is fueled by four pellets of $^{238}PuO_2$. These are encapsulated in iridium, but the remainder of the components are graphitic. An exploded view of the proposed TPV system is shown in Fig. 53. The components fit inside the converter housing, and each of the canister faces radiates to an array of 8 × 8 GaSb cells, each of approximately 1 cm^2 in area. The cells are covered by a resonant array filter consisting of a patterned gold film, as described in Section 4. Only a narrow range of wavelengths (around the bandgap of the semiconductor) reaches the cells, which ensures efficient conversion and prevents the cells from overheating. The resonant array filter is deposited directly onto the cells. On each face of the canister are two parallel-connected strings of eight GaSb cells in series. The entire array is connected to form a 64 × 4 series-parallel network with an output of 28 V. The system was designed to generate 250 W of electrical power.

The entire system was designed with four fins to keep the cells reasonably cool. Figure 54 shows an exploded view of the entire generator and one radiator fin. Within the fins, there is an aluminum honeycomb with two heat pipes. There are two skins on the faces of the fins: an aluminum skin to provide structural strength and an outer skin consisting of a graphitized carbon-carbon composite to provide high thermal conductivity in the fiber direction. The fins are each 75 cm in length.

A detailed study was made of each of the components in the systems, including the effect of the thickness of the graphite skin on the cooling fins, the fin dimensions, the fin geometry, and the effect of the filter and cell performance. It was concluded that potential improvements in the filters would have a much greater benefit on the system performance than would improving the cell performance. It would also be interesting to study the system performance using MIM converters with minimal sub-bandgap absorption and incorporating a back-surface reflector. A resonant array filter could be used for the purposes of comparison, but a broad-band spectrum could be converted as effectively without penalty.

It was shown that the replacement of the radioisotope thermoelectric generator by the radioisotope-fueled TPV generator typically used on such missions wold reduce the fuel requirement by about three times and would triple the efficiency and specific power of the power-generating system. If the parabolic communications antenna were combined with the TPV generator, further gains would result.

5.3.4. Liquid-hydrocarbon-fueled TPV

Guazzoni et al. [103] developed a conceptual design for a multi-fuel liquid hydrocarbon generator. This was specifically aimed at military applications, and the Army

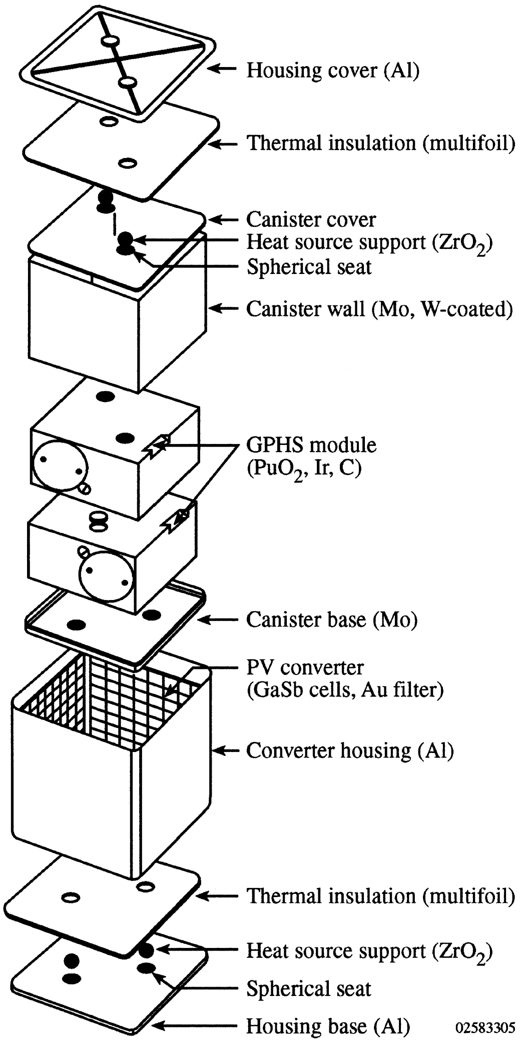

Fig. 53. Exploded view of the components of the radioisotope-fueled TPV generator proposed by Shock et al. Reproduced by permission of the American Institute of Physics, and the author(s) [102].

in particular. One of the attractions of TPV to the Army is its scalability. This system was man-portable, with a capacity of a few hundred watts to 2–3 kW output, with the applications ranging from battery chargers to multi-fuel generators. There is a strong military emphasis on diesel fuel in the field because of the ground network already in place for distribution to vehicles using diesel. Attractive features of diesel include its low flash point, low vapor pressure, and low flame speed, all of which are attractive from the point of view of safety. The system under development uses a

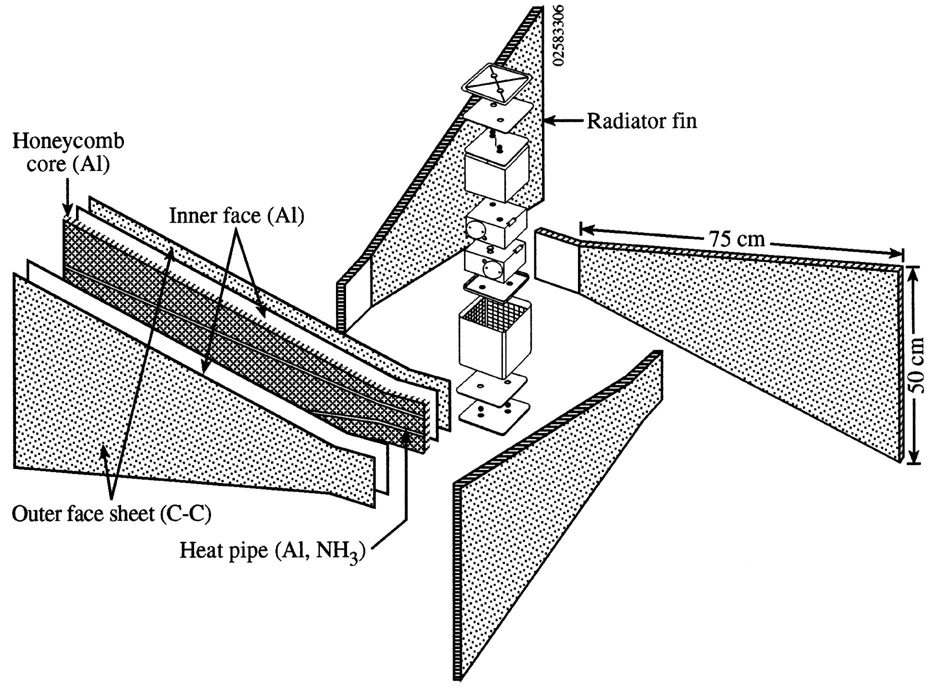

Fig. 54. Exploded view of the radioisotope-fueled TPV generator and of one of the cooling fins. Reproduced by permission of the American Institute of Physics, and the author(s) [111].

Babington atomizer in which a continuous liquid film, covering a convex surface, is broken by a jet of compressed air. The jet takes with it a dispersion of liquid particles: smaller in diameter than those produced by conventional nozzles. Smaller droplets enable start up of equipment at lower temperature.

Figure 55 shows a schematic of the first-generation design. The radiator is an open-ended cylindrical structure of Hexalloy silicon carbide, and it encloses a closed-end cylindrical mantle made of Hastelloy, the surface of which was 1 cm away from the surface of the radiator. The burner tube fed directly into the cylindrical mantle and had perforations covering its entire surface. The perforations were distributed to ensure equal energy distribution on the surface of the radiator. The combustion products would move along the annular space between the mantle and the radiator and leave the combustion chamber, where they pass through a heat exchanger that preheats the input primary air for combustion. The Hastelloy mantle can only be operated up to 1350°C, which leads to the outer surface of the silicon carbide radiator stabilizing at ~1000°C. The next-generation design, however, will use a higher-temperature Hexalloy radiator that can be operated up to 1650°C. TPV cells will be mounted on the inside surface of a water-cooled cylinder facing the radiator along its entire length. The support structure will be water cooled, and the cells will be 2.5 cm

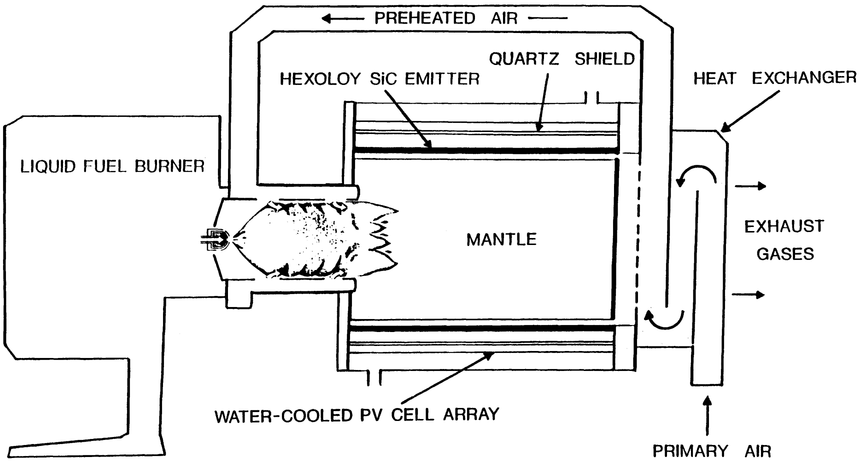

Fig. 55. Schematic of the diesel-fueled TPV generator proposed by Guazzoni et al. Reproduced by permission of the American Institute of Physics, and the author(s) [103].

away from the radiator. Preliminary tests with the heat exchanger indicate that it can preheat the primary air to between 500–550°C.

For the broad-band radiator considered in this study and the radiator temperatures intended, either GaSb or GaInAs cells may be considered. The radiant properties of the Hastelloy silicon carbide radiator are well known over wavelength and varying temperatures up to 8 μm and 1500°C, respectively. The radiated energy from the Hastelloy radiator, operating at 1000°C, was calculated to be about 12 W cm^{-2}. Of this, about 1 W cm^{-2}, or 8.2%, is in the convertible region below 1.7 μm. About 52% lies in the range of 1.7–4 μm, and about 40% lies in the range of 4 μm to infinity. The approach taken by Guazzoni et al. [103] assumed that the radiator would be coated with a selective coating to ensure that it would be fully reflective and non-absorbing (i.e., non-emissive for wavelengths > 1.7 μm). At shorter wavelengths, the coating would be totally transparent to permit the silicon carbide radiation to pass unimpeded. Various combinations of coatings were used and were reported as having been tested up to 1000°C without problem. For higher-temperature operation, the authors suggest using coatings of tantalum pentoxide and silicon.

Allowing for the directionality of the radiator, the authors calculated that the total convertible power from the radiator would be approximately 962 W for their geometry. Figure 55 shows a schematic of the complete first-generation design, and Fig. 56 shows the reflectance of the coated silicon-carbide surface. The latter shows that only wavelengths between the points corresponding to 4 and 8 are convertible by the cells, and the two reflectance edges indicate that all wavelengths, both shorter and longer, are reflected back in the general direction of the radiator, which will recover some of this unusable energy.

The authors assumed that the cell packing factor on the inside of the support structure is 80%, giving a total cell area of 1116 cm^2. They further assumed a 4% loss

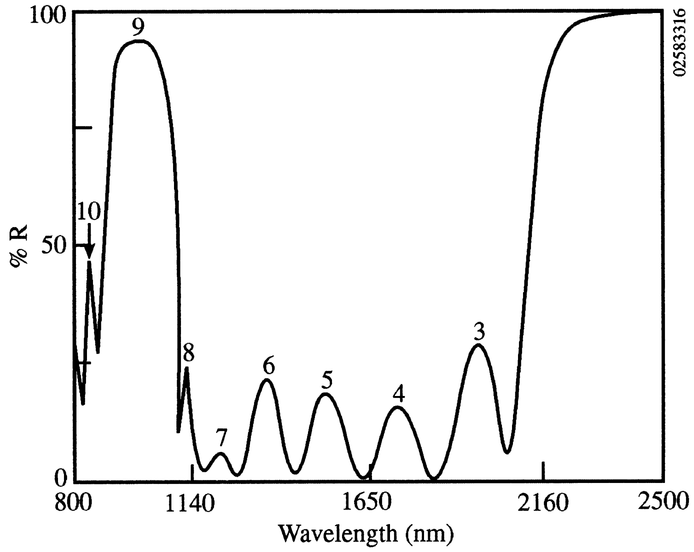

Fig. 56. Reflectance of a coated silicon-carbide surface. The latter was coated to ensure that only above-bandgap radiation reaches the TPV cells. Reproduced by permission of the American Institute of Physics, and the author(s) [103].

leading to a net usable incident radiation of about 740 W. Of the incident energy, they calculated that 15% would be reflected by the cell grids, and nearly 50% would merely heat the cell because the photons have energy in excess of the bandgap. With a cell efficiency of 39%, the 1000°C radiator would provide an electrical output of 288 W. Auxiliary power is needed for the burner and for the water cooling system and would amount to a further 80 W reduction, the net output being 208 W. The authors then estimated that the efficiency of such a system would be about 4.1%. They further showed that by placing a quartz shield between the radiator and the cells, the demands on longwave photon recirculation would be reduced and would lead to an efficiency of 4.8% for a radiator operating at 1000°C. Assuming that the temperature of the radiator could be increased to 1300°C, then the same configuration would have a system efficiency of 9%.

The authors concluded that their design study, based on the silicon carbide radiator and the low-bandgap converters, would yield system power densities substantially higher than those based on selective ytterbia radiators coupled with silicon cells.

5.3.5. Diesel-fueled TPV system

Becker et al. [104] developed a 150-watt portable TPV generator designed for a liquid fuel. Rather than optimizing individual components, these workers focused on optimizing the collective performance of all the components to maximize the system efficiency. The system was based on the fibrous ytterbia selective radiator principle developed by Nelson [34], matched to high-efficiency silicon cells. A dielectric filter was used for photon recirculation and a ceramic recuperator for thermal recirculation. The prototype system was operated with air, pre-heated to a temperature of 1350 K.

As discussed earlier, there are many applications for TPV systems in the range of 100–500 W generating capacity, including man-portable power supplies for communications and various military purposes. These applications are presently powered by either diesel generators or batteries. The former are noisy, polluting, and have limited life, whereas the latter have a low power density, a limited shelf-life, high cost, and problems of disposal. The development of a man-portable TPV system in the required power range is, therefore, seen as important. As discussed earlier, TPV generation appears to be capable of overcoming the shortcoming described above. The radiator was based on the design developed by Nelson [34] with continuous fibers of ytterbia woven into a ceramic support structure. The radiator can be made in the form of tiles up to 15 cm × 15 cm without losing their robustness, enabling large-area systems to be developed. Becker et al. [104] also commented that the radiator could be based on fibers of erbia, which is well-matched to GaSb converters.

The fuel was mixed with input air immediately above the substrate surface, thus ensuring that the ytterbia filaments were exposed to the maximum flame temperature. After combustion, the hot waste products were passed through the ceramic recuperator to heat the incoming combustion air to 1350 K. The PV cells were separated from the combustion gases by two quartz windows, coated with dielectric filters to reflect the unusable long-wavelength photons, and cold air was directed between the filters to maintain relatively low temperatures. The PV array itself was initially mounted on a forced-convection-cooled heat sink, although a water-cooled heat sink is intended to be used with more-advanced prototypes.

The design specifications of the current and advanced prototype generators are shown in Table 5. As can be seen, the efficiency of the PV cell was assumed to be

Table 5
Design specifications for the existing and advanced prototype TPV generators [104]

Parameter	Current prototype	Advanced prototype
Radiator temperature (K)	2000	2100
Air preheat temperature (K)	1350	1650
Average radiated power (W cm^{-2})	3.50	5.00
Average radiator view-factor	0.80	0.80
Average incident power on Si cells (W cm^{-2})	2.80	4.00
Radiator area (cm^2)	291	291
Cell area (cm^2)	288	288
Cell efficiency (%)	38	38
PV array uniformity factor	80	85
Gross power output (W)	245	372
Ancillary power (W)	75	57
Net power (W)	170	315
Gross efficiency (%)	6.5	8.8
Net efficiency (%)	4.5	7.5

38%, which would lead to a net system efficiency of 4.5 and 7.5% for the current and advanced prototypes, respectively. The existing prototype was designed to operate at a radiator temperature of 2000 K and an air preheat temperature of 1350 K. However, the advanced prototype is intended to operate with a radiator temperature of 2100 K and a preheat temperature of 1650 K. The gross power output is reduced from 245–170 W because of the need to provide 75 W for the ancillary equipment (including cooling air, combustion air, and water recirculation). In the advanced prototype system, it is expected that the net output power would increase from 170–315 W. The net system efficiency would then increase from 4.5–7.5%. The existing prototype system was tested with a radiator temperature of 2000 K for many hours with a total radiated power density of 3.7 W cm^{-2}.

Figure 57 shows the output power from the array (presumably not from the completed system) as a function of the convertible power from the radiator. As can be seen, this increased to 150 W for the existing system, although it is expected that this would increase to 228 W when a system with improved silicon cells is used.

5.3.6. *Propane-fueled TPV system*

Fraas et al. [105] are among the only workers to be near manufacture of TPV systems. A schematic of their devices is shown in Fig. 58, with an actual photograph in Fig. 59. The unit is about 15 cm in diameter and about 60 cm tall. The unit is not designed to maximize recuperation of longwave photons, but instead, is intended for cogeneration of electricity and heat. The authors estimated that the unit (which they

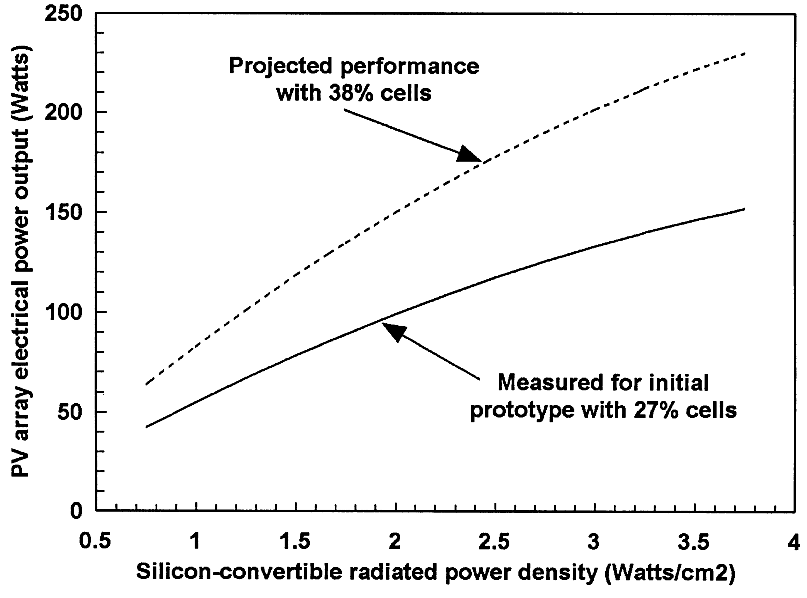

Fig. 57. Performance of the existing and advanced-prototype TPV generators developed by Becker et al. Reproduced by permission of the American Institute of Physics, and the author(s) [104].

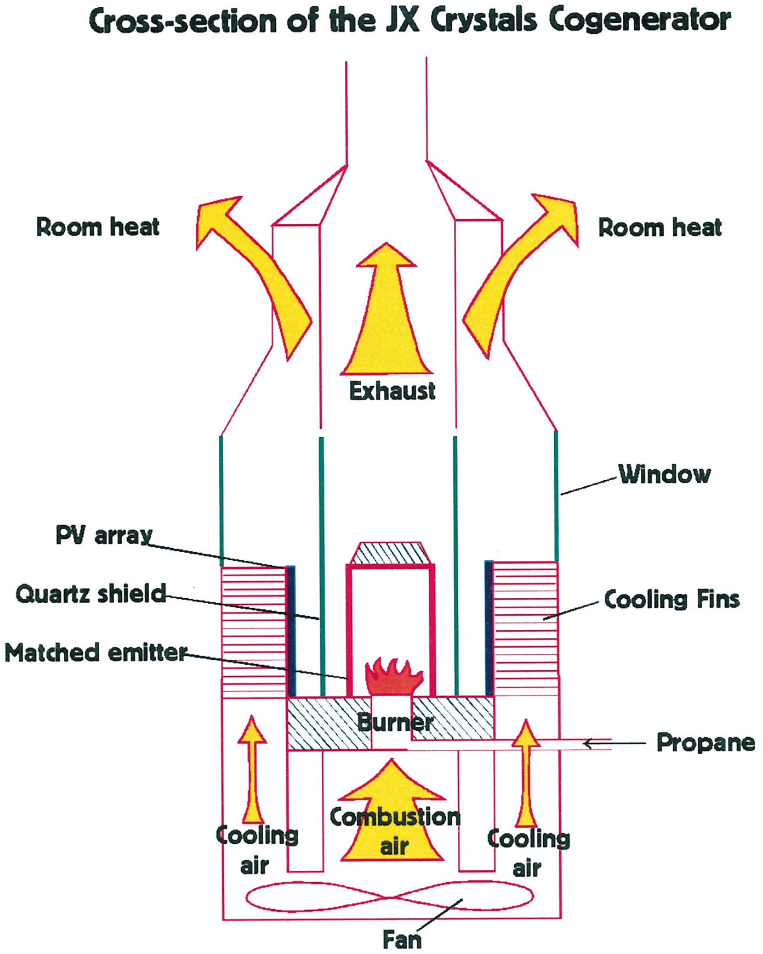

Fig. 58. Schematic of the TPV generator developed by Fraas et al. Reproduced by permission of the American Institute of Physics, and the author(s) [105].

referred to as the Midnight Sun®) is capable of generating 500 W-h of electricity per day and pointed out that this is equivalent to the daily output of a 200-W flat-panel photovoltaic system in the northern states of the United States. The authors also believed that there is a substantial market for their devices for applications such as mountain cabins, pleasure boats, and recreational vehicles.

The system schematic shows that it consists of a tube for mixing the fuel and air, a combustion chamber, a proprietary matched infrared emitter, a TPV array of 48 cells of GaSb connected in series, and cooling fins. The fuel source is propane and the radiator temperature is about 1200–1400°C. The fan, shown in the lower part of Fig. 59, is used to provide air for cooling the TPV cells and for providing the means of

Fig. 59. Photograph of the JX Crystals TPV generator developed by Fraas et al. Reproduced by permission of the American Institute of Physics, and the author(s) [105].

combustion. A deep-cycle marine 12-V battery is used for energy storage. The system is designed such that the propane is automatically shut off if the flame is extinguished. At its intended operating temperature, the array delivers about 15 V at its maximum power point, at which the current is about 1.6 amps. The current/voltage characteristic of the PV array is shown in Fig. 60, which indicates that the fill factor is rather low. The fill factor of typical GaSb cells is about 75%, which indicates that there is room for improvement. According to company representatives, at the time of writing (December 1997), the system is undergoing beta testing and the company hopes to offer the unit for sale in 1998. Efforts are also under way to manufacture arrays and systems of much larger array output. Figure 61 shows the output of an array of nominally 400 W. This was tested at the University of Western Washington and was measured using a radiant surface at a temperature of about 1700 K. More recently, the output has been increased to 600 W.

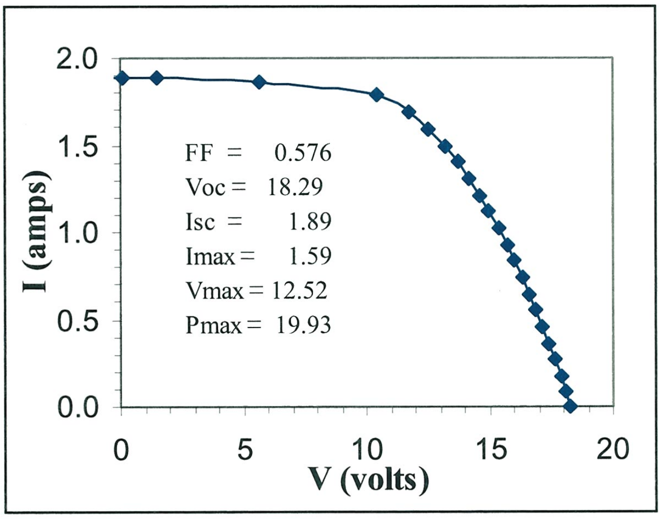

Fig. 60. Typical current/voltage characteristic of the GaSb-based TPV generator developed by Fraas et al. Reproduced by permission of the American Institute of Physics, and the author(s) [105].

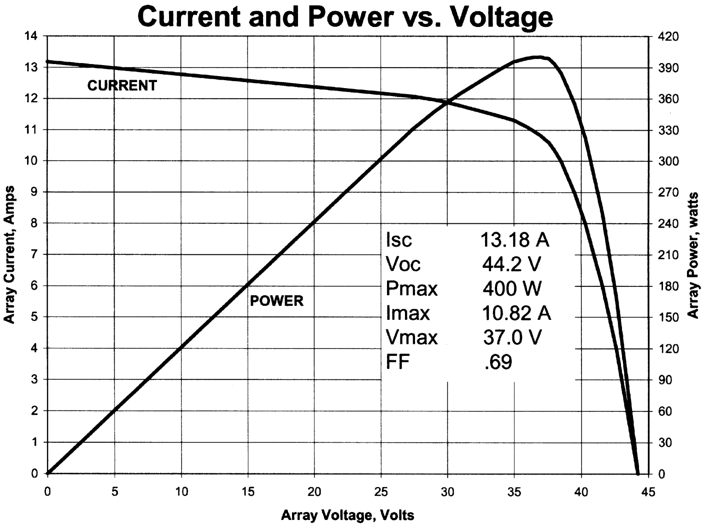

Fig. 61. Electrical power output and the current/voltage characteristic of an array of 48 GaSb cells connected in series. Reproduced by permission of the American Institute of Physics, and the author(s) [105].

Adair et al. [38] also demonstrated a prototype system using propane/air fuel and composite selective radiators. They attempted to determine the efficiencies of individual components contributing to the system efficiency. They concentrated firstly on the heat source and pointed out that in real systems, there are losses of the chemical energy of the fuel due to heating of surfaces other than that of the radiator, incomplete combustion, and poor coupling of the flame to the radiator surface. They commented that the thermal efficiency (fuel to radiated flux) decreased at about 0.05% per Kelvin increase in radiator temperature [106], and that the typical thermal efficiency without recuperation is 30% for a radiator temperature of 1475 K. This number increases substantially with waste-heat recuperation. After 2075 K, the thermal efficiency of the system with recuperation is as high as 70%.

The radiator efficiency may be defined as the fraction of the in-band radiation (the radiation that is convertible by the PV semiconductor converter) to the total radiant energy. However, this quantity also depends on the bandgap of the semiconductor.

The conversion efficiency of the TPV cells again depends on many factors, as discussed earlier, but an efficiency of 16.2% for lattice-matched $In_{0.53}Ga_{0.47}As$ illuminated by a rare-earth-oxide radiator was reported [107]. There is considerable room for improvement using the MIM devices discussed earlier [70].

The fuel in the research prototype was a mixture of propane and air, and the relative flow rates of each could be measured independently. Figure 62 shows a schematic of

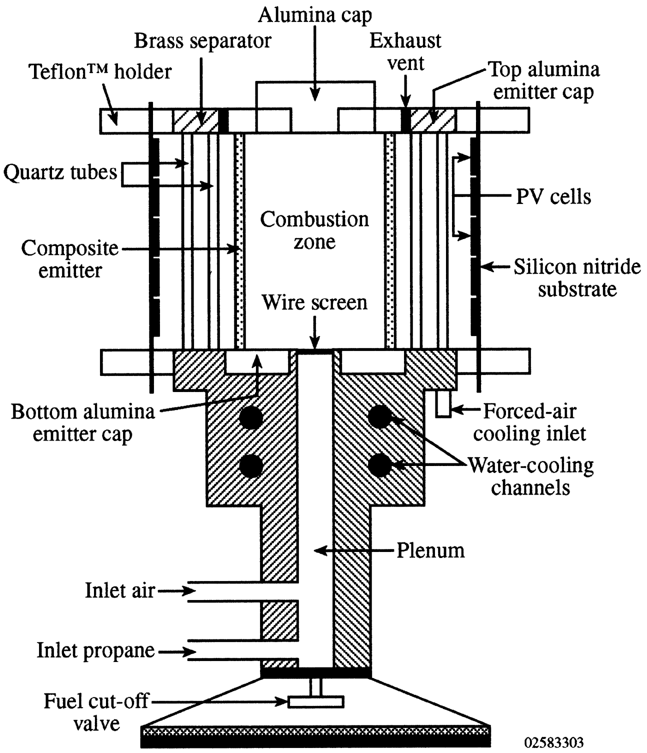

Fig. 62. The prototype TPV system developed by Adair et al. Reproduced by permission of the American Institute of Physics, and the author(s) [38].

the system in which the mixing chamber, wire screen, and combustion zone can be seen. The radiator was cylindrical, and between it and the PV cells were two quartz tubes to minimize heating of the cells and to contribute, to some extent, to sub-bandgap photon recirculation. The authors studied various radiator configurations and semiconductor bandgaps. Five photovoltaic cells were connected in series for the tests. The uniformity of the radiation from the best radiator candidates was investigated by scanning a thermopile sensor around the radiator as a function of azimuthal angle.

Experimentally, it was found that the ideal radiator-wall thickness was 1.5 mm, with smaller thicknesses leading to breakage and greater thicknesses to a decrease in performance. The thermal efficiency is shown in Table 6 for three different inputs of fuel energy to the system. This indicates that the thermal efficiency was about 16–17%.

It was also found that the alumina caps shown in Fig. 62, at either end of the combustion zone, became very hot and caused them to radiate a significant amount of energy. There was also significant convective heat loss from the disks. It appears that there is room for improvement of the end-disk design. Note that in the estimate of the above thermal efficiency measurements, the two quartz tubes shown in Fig. 62 were absent. In measuring the efficiency conversion of radiant energy to electrical power, the quartz tubes were replaced. This is important because all photons greater than 4.5 μm wavelength would have been absorbed by the tubes. Fifty percent of the heat is, therefore, radiated inwards to be re-absorbed by the radiator. Figure 63 shows the relative radiated intensity of an erbia radiator; however, the in-band radiation is also attenuated by the quartz tubes. The authors pointed out that the in-band radiation decreased by $\sim 10\%$, whereas the out-of-band radiation decreased by almost 45%. The radiant power density incident on the PV array is inevitably less than that radiated by the erbia because the view-factor is less than unity. Table 7 shows the incident power densities as a function of the input fuel powers corresponding to those shown in Table 6.

This indicates that the maximum incident power was 38.4 W. It was found that the output power from the PV array increased with the input fuel power, but the radiators tended to crack because of the higher temperatures. The end disks were also prone to cracking. Analysis of the current/voltage characteristics of the cells showed that the

Table 6

Thermal efficiency of erbia radiators. These data show that the efficiency of conversion of fuel to photons is approximately 16–17% [38]

Input fuel power (W)	Radiant power density (W cm^{-2})	Total radiated power (W)	Thermal conversion efficiency (%)
800	1.06	128	16.0
1070	1.48	179	16.7
1330	1.83	221	16.6

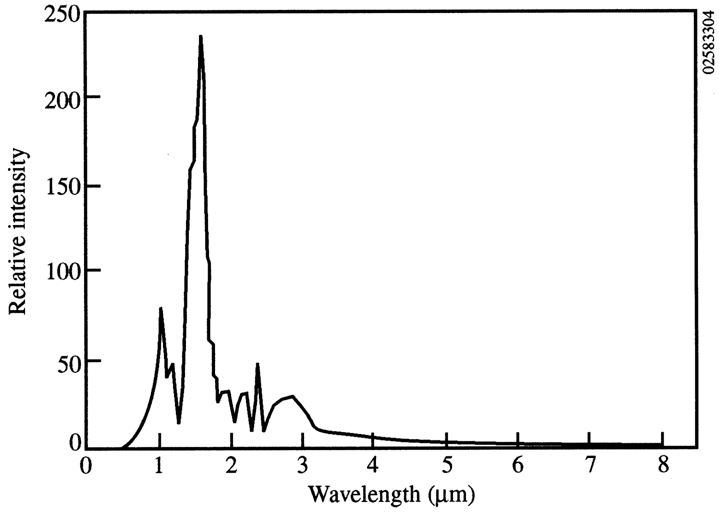

Fig. 63. Variation of the spectral exitance with wavelength for an erbia radiator. Reproduced by permission of the American Institute of Physics, and the author(s) [38].

Table 7
Variation of the incident optical power on the PV array as a function of the input fuel power [38]

Input fuel power (W)	Power density at PV array surface (W cm^{-2})	Total incident power (W)
800	0.121	18.2
1070	0.200	30.0
1330	0.256	38.4

projected cell conversion efficiency was between 25 and 26.5%. The product of the efficiencies of these three processes (thermal efficiency, radiator efficiency, and cell efficiency) led to a system efficiency of ~0.7%.

Various improvements could be made to the system, the most important of which is the recuperation of the longwave photons. This would reduce the amount of fuel and air for the same radiator temperature, and the thermal efficiency could, in principle, increase to 100%, with 100% effective recuperation. The two insulating disks at the end of the combustion chamber also need to be improved. As reported, 20% of the input power is lost radiatively and convectively from these disks. Better coupling between the combustion products and the radiator surface will also ensure higher thermal efficiencies. In addition, the TPV cells had no anti-reflection (AR), implying a large decrease in the electrical conversion efficiency. With an AR coating, the cell efficiencies could increase to as high as 30%. (Note that this is roughly in accordance with the calculations shown in Section 3.) With these system design improvements, the system efficiency and output power would improve to 6.3%. Although this is still modest, there is adequate room for further improvements. For example, the use of a plasma filter on the quartz tubes could greatly reduce the extent to which they heat and radiate in both the forward and backward directions. It would be relatively straightforward to prevent the quartz tubes from heating by placing the TCO plasma filters facing toward the combustion chamber. In addition, the design of the cells dictated that conducting substrates were used. As discussed in Section 3, Ward et al. [70] demonstrated a monolithically integrated, series-connected array of cells on a semi-insulating InP substrate. This largely eliminates free-carrier absorption, prevents cell heating, and leads to improvements in performance. There is thus considerable room for improvement of the system beyond the comments made by the above authors.

5.3.7. Natural-gas-fueled TPV system

Kushch et al. [108] also demonstrated a TPV cogeneration system for the production of hot water, hydronic space heating, and electric power generation. This was based on an ytterbia radiator, and the system was designed to have a nominal capacity of 80,000 BTUs per hour. It was fired with premixed natural gas and air. Conversion was achieved using single-crystal silicon cells and testing of the devices demonstrated an electrical power output from the array of 200 W. The overall system efficiency (inclusive of heating and electricity) was estimated to be $> 83\%$. The pollutants of both NO_x and CO were both within the California limits.

A schematic of a ‘possible’ system is shown in Fig. 64, with an illustration of the

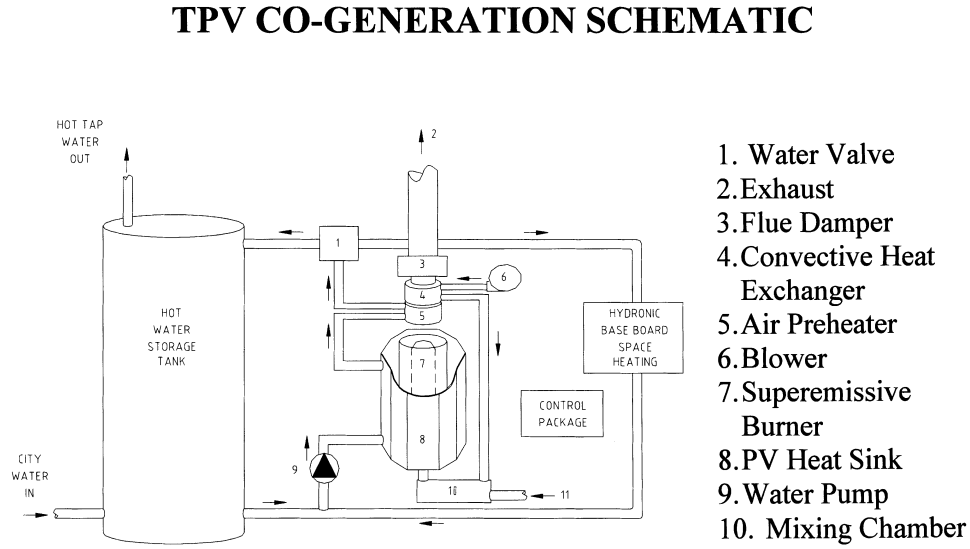

Fig. 64. Schematic of the hydronic/electric generator developed by Kushch et al. [108].

system in Fig. 65. Although recuperation is shown in the schematic, it was not incorporated in the proof-of-concept prototype. As with other designs, neither Pyrex nor quartz tubes were used to separate combustion products from the TPV cells to prevent overheating of the latter. Krist et al. [109] of the Gas Research Institute suggested that the advantages of a cogenerator would include:

—fewer system components and, therefore, greater reliability;
—reduced footprint;
—ease of installation;
—reduced installation cost;
—lower operating costs;

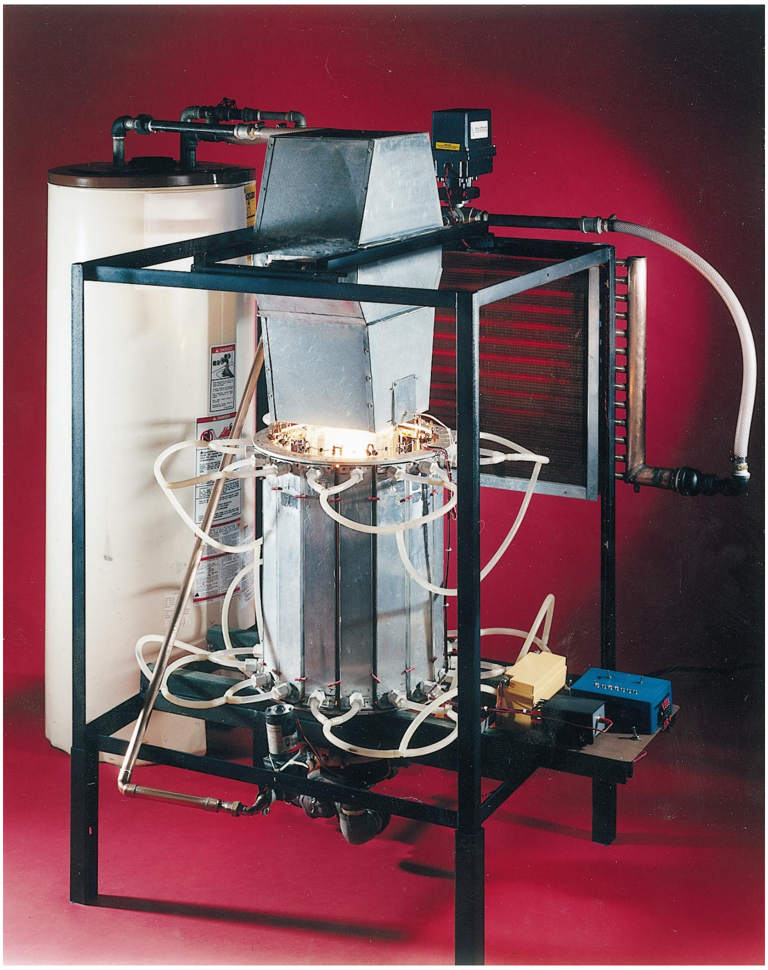

Fig. 65. Photograph of the Quantum Group, Inc., TPV hydronic/electronic TPV generator developed by Kushch et al. Reproduced by permission of the American Institute of Physics, and the author(s) [108].

—excellent reliability;
—excess electrical energy;
—greater fuel utilization;
—minimal emission of pollutants.

Single-crystal silicon PV cells, designed for operation under one-sun, were used in this project, and they had a conversion efficiency of 20.5% based on a reference solar spectrum. The cells were connected in series in arrays of twelve, and the arrays were then mounted circumferentially around the ytterbia radiator, as shown in Fig. 66. The electrical circuit produced ~18.5 volts, and the arrays were cooled. After cooling the cells, the water was directed to the conductive heat exchanger.

The system was tested under a variety of conditions, and the electrical output and the gaseous combustion products were monitored. Figure 67 shows the PV array output as a function of the excess air in the air/fuel mixture. This indicated that the system output peaked at about 200 W for the minimum excess air. Three fuel input rates were used, and the output appeared to be relatively independent of this. Figure 68 shows the concentration of carbon monoxide in the output from the flue. Under all conditions except the most fuel-rich, the output concentrations (measured in nanograms per Joule) were less than the upper limit for California. Similar data were obtained for other greenhouse gases. Figure 69 indicates that the flue losses are also minimal and the conclusion of the analysis was that the overall system efficiency was about 83% (inclusive of both electricity and heat).

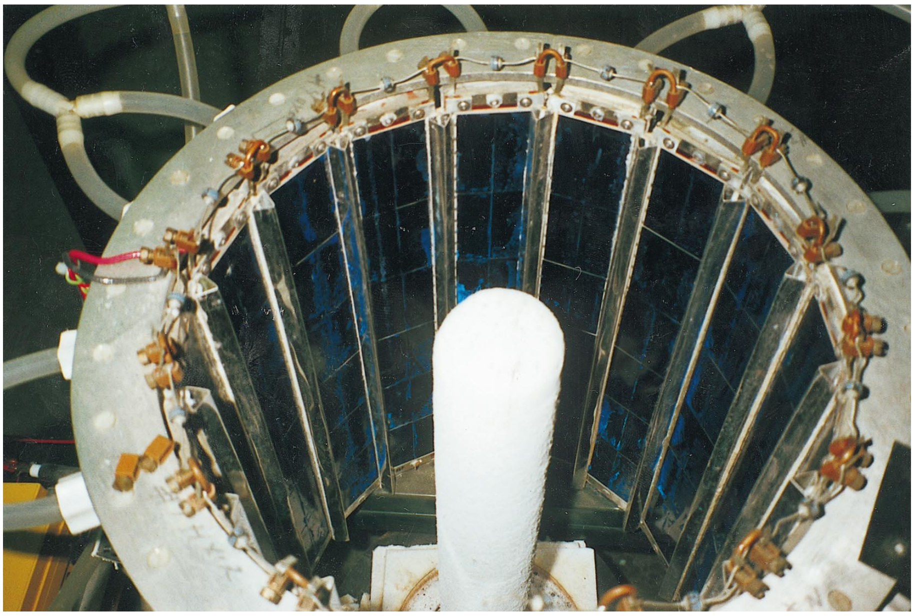

Fig. 66. Illustration of the PV cell array and the ytterbia radiator. The arrays are connected in circuits of 12 cells. Reproduced by permission of the American Institute of Physics, and the author(s) [108].

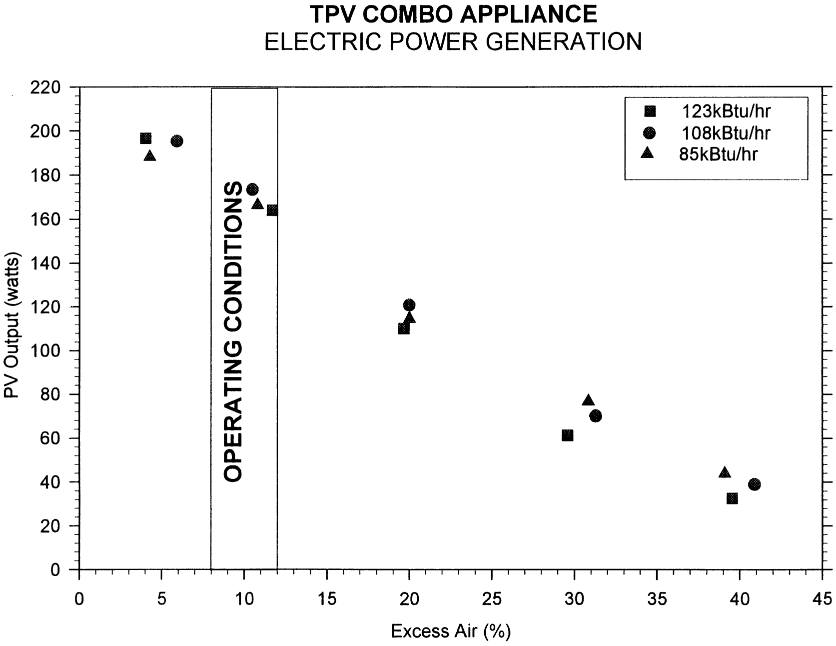

Fig. 67. Variation of the electric output power with the excess air in the fuel/air mixture, from the TPV generator developed by Kushch et al. Reproduced by permission of the American Institute of Physics, and the author(s) [108].

5.4. Summary

In this section, we have discussed a sample of the relatively small number of papers concerned with modeling systems. These indicate that more realistic predictions are now being made of performance than was the case some years ago. The two models discussed both take into account non-idealities in the various components in the systems and suggest that an upper limit of performance, in the near-term, of 20% may be an ambitious target. Several very interesting facts emerge from the modeling, and it appears that additional design studies would be valuable. The example of a temperature distribution across the radiator is instructive and clearly indicates that non-idealities in the array may result, even if the characteristics of the individual cells were identical. Further modeling would undoubtedly reveal other important facts about critical factors in system design.

There will inevitably be a compromise between power density and efficiency, and selective radiators may be advantageous if the latter is vital. If selective radiators can be developed that have near-ideal spectral performance, then they are likely to be the basis of the most efficient systems. On the other hand, there are likely to be severe difficulties in eliminating out-of-band radiation. With broad-band radiators, the key issue appears to be the need to achieve near-ideal sub-bandgap photon recirculation. Without this, the efficiency of broad-band systems will inevitably be low, even if their

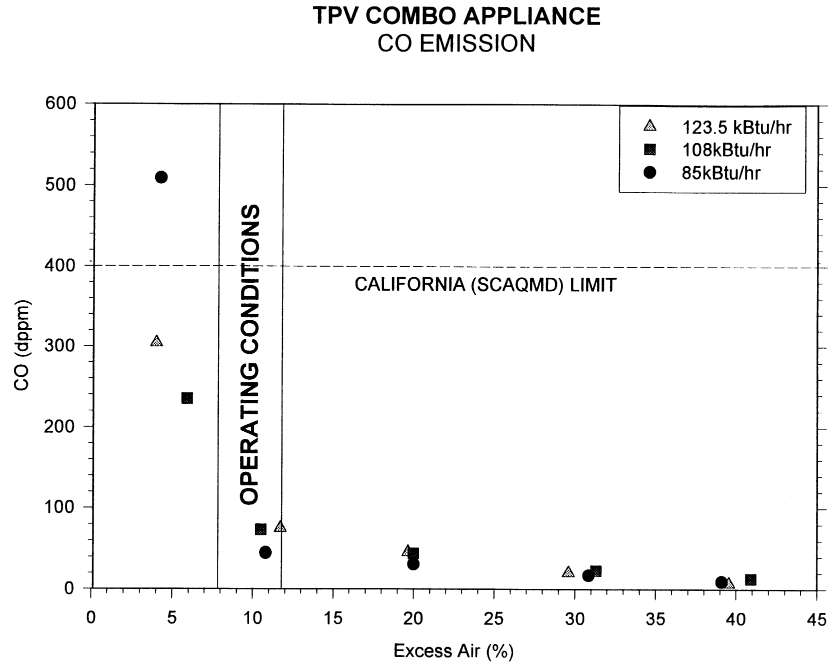

Fig. 68. Variation of carbon monoxide concentration with the concentration of excess air in the fuel/air mixture. Reproduced by permission of the American Institute of Physics, and the author(s) [108].

power-density output is relatively high. In both cases, photon recuperation will almost certainly be required.

Very few systems demonstrations have been performed, which is an omission in the technology. This may be because most research has been on specific components, rather than on entire systems. It is desirable to reduce some of the proposed designs to practice rather than speculating about their likely performance. Without the experience of testing and characterizing real systems, it is impossible to speculate realistically about their performance. The work of [110] provides the only evidence on a developed product, and this company is the first to sell first-generation systems. More system demonstration is vital for the further development of this technology, and this may lead to an acceleration of its widespread deployment.

Several designs have been discussed in this section, and these involve various combinations of components. The fuels considered are very diverse, and TPV generation offers great flexibility. Likewise, the potential applications considered vary from military (fueled by diesel) to space (fueled by a radioisotope). Relatively little work is presently being performed on non-military applications, and the military sponsors of the work tend to be the developers of the systems, rather than researchers, who seem to be mainly concerned with developing specific components. In general, systems research is rather limited, and it is unlikely that demands on systems being developed for military purposes would necessarily be useful for non-military appli-

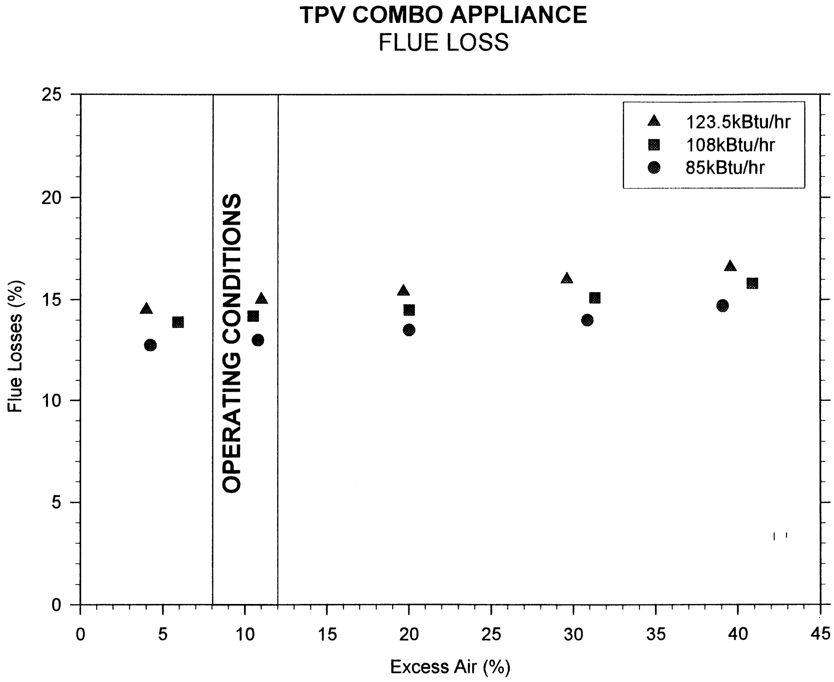

Fig. 69. Flue loss as a function of excess air in the air/fuel mixture. Three different fuel input rates are shown. Reproduced by permission of the American Institute of Physics, and the author(s) [108].

cations. One need only consider the issue of infrared thermal signature as an example. It is clearly vital to minimize any thermal signature from a man-portable TPV generator. This is a demand that would not be important to a non-military application.

In summary, TPV systems studies are in their infancy, and the field is sure to benefit as there are more demonstrations and modeling investigations. The entire field would benefit from more work of this sort.

6. Concluding remarks

This paper has focused on elementary principles of TPV and it has also reviewed developments in critical topics. The reviews have mainly been taken from the Third NREL TPV Conference and the objective has been to provide an introductory overview of TPV, rather than to provide a review for experts in the field. Each of the sections has been written so that it may stand alone, even though there are frequent references to the other sections. Each section has been summarized individually, rather than an overall summary having been provided at the end of the paper.

In Section 2, radiation was discussed and included both broad-band and selective radiators, as well as some revisionary thoughts on the background physics and chemistry. The majority of research to date (at least in this most recent phase of interest in TPV) has been on the development of high-quality semiconductor converters but, as should be clear, the other components in a TPV system are equally important. Indeed, many experts in the field now believe that the urgent need is for work on thermal management of the system as a whole, rather than on semiconductor physics. The techniques used to return sub-bandgap photons to the radiator (discussed in Section 4) are critical. Many options are worth considering but, of these, the back-surface reflector technique appears to have the best prospects. So far as the author is aware, no efforts have been devoted to the characterization of the absorption properties of the radiators at high-temperature. Although the emission characteristics of some radiator materials have been measured, the same is not true of the absorption characteristics. There may be differences in the absorption and emission properties of the same radiators, even though elementary considerations suggest otherwise. So, even though techniques for the recirculation of sub-bandgap photons have been shown to demonstrate the appropriate optical characteristics, the extent to which the recirculated photons actually do contribute to the system efficiency has not been firmly established.

In Section 3, the various efforts to model the behavior of the discrete devices were discussed. To a good approximation, the predicted efficiencies are similar unless one assumes that it will eventually be possible to approach the limit dictated by radiative recombination. The difference between the models of radiative recombination and the empirical method hinges on the approximation that is used for the reverse saturation current density. In the method of radiative recombination, the reverse saturation current density is not considered explicitly because the approach depends on the principle of detailed balance, whereby the flux is exactly balanced by recombination. The empirical method includes an approximation that was developed on the basis of experience with diodes of many different bandgaps. Even in this approach, nothing is said about the mechanism of recombination. If non-radiative processes can be essentially eliminated (as has been the case with silicon solar cells) then it may be possible that efficiencies of TPV devices eventually exceed the values presently being predicted by the approximate method. This has now been established for silicon solar cells, with efficiencies now exceeding predictions of approximate methods. Thus, the radiative recombination limit is useful in providing a long-term goal. It should also be noted that the optimum bandgap for a given radiator temperature, is less when predicted by the principle of detailed balance. This section also reviews the performance of existing devices. These are presently restricted to ternary and quaternary alloys from the III–V family of semiconductors. There does not yet appear to be convincing evidence that the performance of the lattice-matched quaternary alloys is superior to that of the ternary alloys, and the added complexity seems dubious at present. There are also many other options for converter development including polycrystalline thin films. It may be possible for such materials to capitalize on work done under the DoE's PV program in the same way as TPV has benefited from the High Efficiency III–V Program. Many new materials remain to be researched and it is important not to limit the scope of work on the basis of short-term demonstration needs. The economics remain, in the opinion of the author, inconclusive and an independent evaluation of the relative costs of the converter and the balance-of-systems needs to be made.

Of the methods of sub-bandgap photon recirculation discussed in Section 4, the interdigitated grid finger MIMBSR design seems to hold the greatest promise. This will become increasingly important as radiator temperatures, and current densities, increase. On the other hand, several other approaches work quite well and could eventually realize the objective. Modeling of multi-layer filters suggests that there are too many factors that can spoil their intended performance and these do not seem likely to provide long-term solutions. Likewise, it seems questionable that the mobility of electrons in TCOs could ever be increased to the values required to minimize free-carrier absorption. However, it is probably realistic to expect the performance of degenerate III–V semiconductors to perform well and these could offer very useful options. Several novel approaches have been suggested to improve photon recirculation but most of these have not, at the time of writing, been reduced to practice.

Section 5 is concerned with TPV systems and is somewhat parallel to Section 3: first discussing modeling and then reduction to practice. In relative terms, there have been very few demonstrations of systems and the field would benefit from more work in this area. The means by which a TPV system may be fueled is very versatile (one of the great strengths of the technology) and each organization that has developed a system, has had a specific reason for choosing a particular fuel. The predicted efficiencies lie in the 5–15% range. Although this may sound disappointing, it must be remembered that the power densities are large and, in any event, it is inevitable that the efficiency of a four- or five-component system is necessarily relatively low. For the future, we may expect to see that the efficiency targets are raised to more ambitious levels but, for the time, the present modeled efficiencies seem reasonable, and difficult to achieve!

At present, most funding for TPV is aimed at providing one or another military agency with a strategic advantage and the cost has not, thus far, been a pressing issue. The advantages offered to submarines, partially powered by TPV, or to soldiers with back-pack-sized TPV generators, seem to be considerable but will inevitably come at a price! In addition, these niche markets will eventually demand reductions in cost. Other non-military markets of relatively small volume will probably be consumer-related and an upper limit on tolerable cost will be established early on in their employment. Stand-alone gas furnaces, for example, are already expensive but prospective buyers will still be very watchful of incremental costs, despite the inconveniences of electricity outages and the experiences of recent years. Careful studies of market size, systems' costs, pay-back time, etc. are essential because the findings will guide future R&D.

Recent cursory studies by the author have shown that there is vast potential for TPV recovery of industrial waste heat: probably the largest consumer of energy in every industrialized nation. In turn, this is likely to benefit industrial competitiveness, energy efficiency, and may even reduce concerns about global climate change.

It is clear that political interest is growing at the time of writing, at least in the U.S.A., and this may be because of an increased awareness of the potential of TPV generation coupled with a balanced Federal budget. If these political influences enhance the probability that a non-military program in TPV will be initiated, this can only be to the National benefit.

Acknowledgements

Publication of this paper was supported by the US Department of Energy (Contract No. DE-AC36-98-GO10337). The author would like to acknowledge the help of Dr. Kannan Ramanathan and Scott Ward of NREL, and Dr. Jeffery Mazer of the US Department of Energy, for their critical reading of the paper thereby helping to improve it substantially.

References

[1] Broman L, Marks J. Co-generation of electricity and heat from combustion of wood powder utilizing thermophotovoltaic conversion. In: Coutts TJ, Benner JP, editors. The First NREL Conference on the Thermophotovoltaic Generation of Electricity. Am Inst Phys Conf Series. New York: American Institute of Physics 1994;321:133–8.

[2] Bett AW, Keser S, Stollwerck G, Sulima OV. Large-area GaSb photovoltaic cells. In: Coutts TJ, Allman CS, Benner J, editors. The Third NREL Conference on the Thermophotovoltaic Generation of Electricity. Am Inst Phys Conf Series. New York: American Institute of Physics 1997;401:41–53.

[3] Schubnell M, Gabler H, Broman L. Overview of European activities in thermophotovoltaics. In: Coutts TJ, Allman CS, Benner JP, editors. The Third NREL Conference on the Thermophotovoltaic Generation of Electricity. Am Inst Phys Conf Series. New York: American Institute of Physics 1997;401:3–22.

[4] Benner JP, Coutts TJ, Ginley DS. Proceedings of the Second NREL Conference on Thermophotovoltaic Generation of Electricity. Am Inst Phys Conf Series, vol. 358. New York: American Institute of Physics, 1995.

[5] Coutts TJ, Allman CS, Benner JP. Proceedings of the Third NREL Conference on Thermophotovoltaic Generation of Electricity. Am Inst Phys Conf Series, vol. 401. New York: American Institute of Physics, 1997.

[6] Coutts TJ, Benner JP. Proceedings of the First NREL Conference on Thermophotovoltaic Generation of Electricity. Am Inst Phys Conf Series, vol. 321. New York: American Institute of Physics, 1994.

[7] Rose MF. Prospector VIII: Thermophotovoltaics—An Update on DoD, Academic, and Commercial Research, vol. 1. Auburn University: Space Power Institute, 1996.

[8] Rosenfeld RL. An ARPA perspective on TPV. In: Coutts TJ, Benner JP, editors. The First NREL Conference on the Thermophotovoltaic Generation of Electricity. Am Inst Phys Conf Series. New York: American Institute of Physics 1994;321:301.

[9] Coutts TJ, Wanlass MW, Ward JS, Johnson S. A review of recent advances in thermophotovoltaics. In: The 25th IEEE Photovoltaic Specialists Conference. IEEE, 1996. pp. 25–30.

[10] Broman L. Thermophotovoltaics Bibliography. Final Report NREL/TP-412-6845, National Renewable Energy Laboratory, 1994.

[11] Avery JE, Fraas LM, Sundaram VS, Mansoori N, Yerkes JW, Brinker DJ, Curtis HB, O'Neill MJ. Lightweight concentrator module with 30% AMO efficient GaAs/GaSb tandem cells. In: The Twenty-First IEEE Photovoltaic Specialists Conference. Piscataway, NJ: IEEE, 1990. pp. 1277–81.

[12] Friedman DJ, Kurtz SR, Bertness KA, Kibbler AE, Kramer C, Olson JM, King DI, Hansen RR, Snyder JK. 30.2% efficient GaInP/GaAs monolithic two-terminal tandem concentrator cell. Progress in Photovoltaics: Research and Applications 1995;3:47–50.

[13] Goldstein MK, DeShazer LG, Kushch AS, Skinner SM. Superemissive light pipe for TPV applications. In: Coutts TJ, Allman CS, Benner JP, editors. The Third NREL Conference on the Thermophotovoltaic Generation of Electricity. Am Inst Phys Conf Series. New York: American Institute of Physics 1997;401:315–26.

[14] Nelson RE. Thermophotovoltaic technology. U.S.A. 5,057,162, 15 October 1991.

[15] Johnson S. TPV market analysis. Final RAK-5-15377, National Renewable Energy Laboratory, 1996.

[16] Fraas L. Low cost processing of III–V TPV cells. In: McConnel RD, editor. The First NREL Conference on the Future Generation Photovoltaic Technologies. Am Inst Phys Conf Series. New York: American Institute of Physics 1997;404:285–92.

[17] Contreras M, Wiesner H, Webb J. Thin-film polycrystalline $Ga_{1-x}In_xAs$ materials. In: Coutts TJ, Allman CS, Benner JP, editors. The Third NREL Conference on the Thermophotovoltaic Generation of Electricity. Am Inst Phys Conf Series. New York: American Institute of Physics 1997;401:403–10.

[18] Dhere NG. Polycrystalline-thin-film thermophotovoltaic cells. In: Benner JP, Coutts TJ, Ginley DS, editors. The Second NREL Conference on the Thermophotovoltaic Generation of Electricity. Am Inst Phys Conf Series. New York: American Institute of Physics 1995;358:409–22.

[19] Biter WJ, Georg KA, Phillips JE. A TPV system using a good filter with $CuInSe_2$ solar cells. In: Coutts TJ, Allman CS, Benner JP, editors. The Third NREL Conference on the Thermophotovoltaic Generation of Electricity. Am Inst Phys Conf Series. New York: American Institute of Physics 1997;401:443–59.

[20] Eisenhauer J, Donnelly P, McQueen S, Monis A, Pellegrino J, Julien J. Glass Technology Roadmap, Department of Energy Workshop Conf-9704153. Columbia, Maryland: Energetics Inc., 1997.

[21] Aigrain P. Thermophotovoltaic conversion of radiant energy; unpublished lecture series at MIT, 1956.

[22] Guazzoni G, Kittl E, Shapiro S. Rare earth radiators for thermophotovoltaic energy conversion. In: The Proceedings of the International Electron Devices Meeting. IEEE, 1968. pp. 130–2.

[23] Bracewell RN, Swanson RM. Silicon photovoltaic cells in TPV conversion, Interim EPRI ER-633, Electric Power Research Institute, 1978.

[24] Ruth R, Moyer JW. Power efficiency for the photovoltaic effect in a germanium grown junction. Physics Review 1954;95:562–4.

[25] Beck RW, Sayers EN. Study of germanium devices for use in a thermophotovoltaic converter, Progress Report No. 2 (final report) DA28-043-AMC-02543(E). General Motors Corporation, 1967.

[26] Venkatasubramanian R, Timmons ML, Pickett RT, Colpitts TS, Hills JS, Hutchby JS, Iles PA, Chu CL. Development of low-bandgap Ge and $Si_{0.07}Ge_{0.93}$ solar cells for monolithic and mechanically-stacked cascade applications. In: The Twenty First IEEE Photovoltaic Specialists Conference. IEEE 1990;1:73–8.

[27] Nelson RE. Thermophotovoltaic emitter development. In: Coutts TJ, Benner JP, editors. The First NREL Conference on the Thermophotovoltaic Generation of Electricity. Am Inst Phys Conf Series. New York: American Institute of Physics 1994;321:80–8.

[28] Hsu D. Chemicool Periodic Table, http://the-tech.mit.edu/Chemicool/U.S.A.: Massachusetts Institute of Technology, 1997. This site contains a complete periodic table and the user may click on any of the elements to access full data on that element. The reader is cautioned that the URLs of websites change frequently. If access is not possible using the URL shown here, it is suggested that a search be done using the name of the site.

[29] Verhoeven JW. Luminescent Lanthanides, http://orgwww.chem.uva.nl/lanthanides, The Netherlands: University of Amsterdam, 1996;1. The reader is cautioned that the URLs of websites change frequently. If access is not possible using the URL shown here, it is suggested that a search be done using the name of the site. This site is devoted to the lanthanide series of the periodic table. Many properties of the lanthanides are listed and a discussion of their importance to many modern technological applications is included.

[30] Winter M. WebElements, http://chemserv.bc.edu/web-elements/web-elements-home.html, U.K.: Sheffield University, 1996. This site gives a period table and one may click on any one of the elements to learn further information about it. The reader is cautioned that the URLs of websites change

frequently. If access is not possible using the URL shown here, it is suggested that a search be done using the name of the site.

[31] Auer von Welsbach C. Incandescent lighting substance, U.S.A. (7 July 1896) 1986;563,524.

[32] Ferguson L, Fraas L. Matched infrared emitters for use with GaSb TPV cells. In: Coutts TJ, Allman C., Benner JP, editors. The Third NREL Conference on the Thermophotovoltaic Generation of Electricity. Am Inst Phys Conf Series. New World:American Institute of Physics 1997;401:169–79.

[33] Parent CR, McFadden BP, Olow JFS. Emission Technology U.S.A. (11 August 1992) 1992;5:137,583.

[34] Nelson RE. Fibrous emissive burners: selective and broadband, Annual TR4527-044-92. Gas Research Institute, 1992.

[35] Nelson RE. Rare earth oxide TPV emitters. In: The 32nd International Power Sources Symposium 1986;95–110.

[36] Chubb DL, Lowe RA, Good BS. Emittance theory for thin film selective emitter. In: Coutts TJ, Benner JP, editors. The First NREL Conference on the Thermophotovoltaic Generation of Electricity. Am Inst Phys Conf Series. New York: American Institute of Physics 1994;321:229–44.

[37] Wilt DM, Fatemi NS, Jenkins PP, Weizer VG. Electrical and optical performance characteristics of 0.74 eV p/n InGaAs monolithic interconnected modules. In: Coutts, TJ, Allman CS, Benner JP, editors. The Third NREL Conference on the Thermophotovoltaic Generation of Electricity. Am Inst Phys Conf Series. New York: American Institute of Physics 1997;401:237–47.

[38] Adair PL, Chen Z, Rose ML. TPV power generation prototype using composite selective emitters. In: Coutts TJ, Allman CS, Benner JP, editors. The Third NREL Conference on the Thermophotovoltaic Generation of Electricity. Am Inst Phys Conf Series. New York: American Institute of Physics 1997;401:277–91.

[39] Chen Z, Adair PL, Rose ML. Multiple-dopant selective emitter. In: Coutts TJ, Allman CS, Benner JP, editors. The Third NREL Conference on the Thermophotovoltaic Generation of Electricity. Am Inst Phys Conf Series. New York: American Institute of Physics 1997;401:181–8.

[40] Gethers CK, Ballinger CT, Postlethwait MA, DePoy DM, Baldasaro PF. TPV efficiency predictions and measurements for a closed cavity geometry. In: Coutts TJ, Allman CS, Benner JP, editors. The Third NREL Conference on the Thermophotovoltaic Generation of Electricity. Am Inst Phys Conf Series. New York: American Institute of Physics 1997;401:471–86.

[41] Chubb DL, Good BS, Clark EB, Chen Z. Effect of temperature gradient on thick film selective emittance. In: Coutts TJ, Allman CS, Benner JP, editors. The Third NREL Conference on the Thermophotovoltaic Generation of Electricity. Am Inst Phys Conf Series. New York: American Institute of Physics 1997;401:293–313.

[42] Cody GD. Theoretical maximum efficiencies for thermophotovoltaic devices. In: Coutts TJ, Benner JP, Allman CS, editors. The Fourth NREL Conference on the Thermophotovoltaic Generation of Electricity. Am Inst Phys Conf Series. New York: American Institute of Physics 1998;460:58–67.

[43] van Roosbroeck W, Shockley W. Photon-radiative recombination of electrons and holes in germanium. Phys Rev 1954;94(6):1558–60.

[44] Shockley W, Queisser HJ. Detailed balance limit of efficiency of p-n junction solar cells. J Appl Phys 1961;32(3):510–19.

[45] Gray JL, El-Husseini A. A simple parametric study of TPV system efficiency and output power density including a comparison of several TPV materials. In: Benner JP, Coutts TJ, Ginley DS, editors. The Second NREL Conference on the Thermophotovoltaic Generation of Electricity. Am Inst Phys Conf Series. New York: American Institute of Physics 1995;358:3–15.

[46] Wanlass MW, Emery KA, Gessert TA, Horner GS, Osterwald CR, Coutts TJ. Practical considerations in tandem cell modeling. Solar Cells 1989;27:191–204.

[47] Prince MB. Silicon solar energy converters. J Appl Phys 1955;26(5):534–40.

[48] Loferski JJ. Theoretical considerations governing the choice of the optimum semiconductor for photovoltaic solar energy conversion. J Appl Phys 1956;27(7):777–84.

[49] Wolf M. Limitations and possibilities for improvement of photovoltaic solar energy converters—Part 1: Considerations for earth's surface operation. Proc IRE 1960;48:1246–63.

[50] Cody GD. Theoretical maximum efficiencies for thermophotovoltaic devices. In: Coutts TJ, Benner JP, Allman CS, editors. The Fourth NREL Conference on the Thermophotovoltaic Generation of Electricity. Am Inst Phys Conf Series. New York: American Institute of Physics 1998;460:58–67.

[51] DeVos A. Endoreversible Thermodynamics of Solar Energy Conversion. Oxford University Press, 1992.

[52] Fan JCC, Tsaur B-R, Palm BJ. Optimal design of high-efficiency tandem cells. In: The Proceedings of the 16th IEEE Photovoltaic Specialists Conference. IEEE, 1982. pp. 692–701.

[53] Nell ME, Barnett AM. The spectral p-n junction model for tandem solar-cell design. IEEE Trans Elec Dev 1987;ED-24(2):257–66.

[54] Green ME. Solar Cells: Operating Principles, Technology, and Systems Applications. University of New South Wales, 1986.

[55] Wanlass MW, Ward JS, Emery KA, Coutts TJ. $Ga_xIn_{1-x}As$ thermophotovoltaic converters. In: The Twenty-Fourth IEEE Photovoltaic Specialists Conference. Piscataway NJ: IEEE, 1994. pp. 1685–91.

[56] Martinelli RU, Garguzov DZ, Lee H, Morris N, Odubanjo T, Taylor GC, Connolly J. Minority-carrier transport in InGaAsSb thermophotovoltaic diodes. In: Coutts TJ, Allman CS, Benner JP, editors. The Third NREL Conference on the Thermophotovoltaic Generation of Electricity. Am Inst Phys Conf Series. New York: American Institute of Physics 1997;401:389–95.

[57] Wang CA, Choi HK, Turner GW, Spears DL, Manfra MJ, Charache GW. Lattice-matched epitaxial GaInAsSb/GaSb thermophotovoltaic devices. In: Coutts TJ, Allman CS, Benner JP, editors. The Third NREL Conference on the Thermophotovoltaic Generation of Electricity. Am Inst Phys Conf Series. New York: American Institute of Physics 1997;401:75–87.

[58] Wanlass MW, Coutts TJ, Ward JS, Emery KA. High-efficiency heteroepitaxial InP solar cells. In: The Twenty-Second IEEE Photovoltaic Specialists Conference. IEEE 1991;1:159–65.

[59] Fraas LM, Huang HX, Ye S-Z, Hui S, Avery J, Ballantyne R. Low cost high power GaSb photovoltaic cells. In: Coutts TJ, Allman CS, Benner JP, editors. The Third NREL Conference on the Thermophotovoltaic Generation of Electricity. Am Inst Phys Conf Series. New York: American Institute of Physics 1997;401:33–40.

[60] Dutta PS, Ostrogorsky AG, Gutmann RJ. Bulk growth of GaSb and $Ga_{1-x}In_xSb$. In: Coutts TJ, Allman CS, Benner JP, editors. The Third NREL Conference on the Thermophotovoltaic Generation of Electricity. Am Inst Phys Conf Series. New York: American Institute of Physics 1997;401:157–66.

[61] Ehsani H, Bhat I, Hitchcock C, Gutmann R. Growth and characterization of $In_{0.2}Ga_{0.8}Sb$ device structures using metalorganic vapor phase epitaxy. In: Coutts TJ, Allman CS, Benner JP, editors. The Third NREL Conference on the Thermophotovoltaic Generation of Electricity. Am Inst Phys Conf Series. New York: American Institute of Physics 1997;401:65–74.

[62] Sundaram VS, Saban SB, Morgan MD, Horne WE, Evans BD, Kettterl JR, Morosini MBZ, Patel NB, Field H. GaSb based ternary and quaternary diffused junction devices for TPV applications. In: Coutts TJ, Allman CS, Benner JP, editors. The Third NREL Conference on the Thermophotovoltaic Generation of Electricity. Am Inst Phys Conf Series. New York: American Institute of Physics 1997;401:105–15.

[63] Hitchcock C, Gutmann R, Borrego J, Ehsani H, Bhat I, Freeman M, Charache G. GaInSb and GaInAsSb thermophotovoltaic fabrication and characterization. In: Coutts TJ, Allman CS, Benner JP, editors. The Third NREL Conference on the Thermophotovoltaic Generation of Electricity. Am Inst Phys Conf Series. New York: American Institute of Physics 1997;401:89–103.

[64] Shellenbarger ZA, Mauk MG, Cox JA, Gottfried MI, Sims PE, Lesko JD, McNeely JB, DiNetta LC. Improvements in GaSb-based thermophotovoltaic cells. In: Coutts TJ, Allman CS, Benner JP, editors. The Third NREL Conference on the Thermophotovoltaic Generation of Electricity. Am Inst Phys Conf Series. New York: American Institute of Physics 1997;401:117–28.

[65] Mauk MG, Shellenbarger ZA, Gottfried MI, Cox JAW, Feycock B, McNeely JB, DiNetta LC. New concepts for III–V antimonide thermophotovoltaics. In: Coutts TJ, Allman CS, Benner JP, editors. The Third NREL Conference on the Thermophotovoltaic Generation of Electricity. Am Inst Phys Conf Series. New York: American Institute of Physics 1997;401:129–37.

[66] Wojtczuk S, Parados T, Walker G. P/N In(Al)GaAs multijunction laser power converters. In: The XIII Space Photovoltaic Research and Technology Conference. NASA Conference Publications 1994;3278:363–71.

[67] Fatemi NS, Wilt DM, Jenkins PP, Hoffman Jr. RW, Weizer VG, Murray CS, Riley D. Materials and process development for the monolithic interconnected module (MIM) InGaAs/InP TPV devices.

In: Coutts TJ, Allman CS, Benner JP, editors. The Third NREL Conference on the Thermophotovoltaic Generation of Electricity. Am Inst Phys Conf Series. New York: American Institute of Physics 1997;401:249–62.

[68] Fatemi NS, Wilt DM, Jenkins PP, Weizer VG, Hoffman Jr. RW, Murray CS, Scheiman D, Brinker D, Riley D. InGaAs monolithic interconnected modules (MIMs). In: The Twenty-Sixth IEEE Photovoltaic Specialists Conference. Piscataway NJ: IEEE. 1997;799–804.

[69] Wojtczuk S. Comparison of 0.55 eV InGaAs single junction vs multi-junction TPV technology. In: Coutts TJ, Allman CS, Benner JP, editors. The Third NREL Conference on the Thermophotovoltaic Generation of Electricity. Am Inst Phys Conf Series. New York: American Institute of Physics 1997;401:205–13.

[70] Ward JS, Duda A, Wanlass MW, Coutts TJ. A novel design for interconnects in a TPV converter. In: Coutts TJ, Allman CS, Benner JP, editors. The Third NREL Conference on the Thermophotovoltaic Generation of Electricity. Am Inst Phys Conf Series. New York: American Institute of Physics 1997;401.

[71] Cotter TM, Thomas ME, Tropf WJ. Magnesium fluoride (MgF_2). In: Palik ED, editor. Handbook of Optical Constants II. Boston, San Diego, New York, London, Sydney, Tokyo, Toronto: Academic Press, 1991. pp. 899–918.

[72] Palik ED, Addamiano A. Zinc sulfide (ZnS). In: Palik ED, editor. Handbook of Optical Constants. Orlando, San Diego, New York, London, Toronto, Montreal, Sydney, Tokyo: Academic Press, 1985. pp. 804.

[73] Coutts TJ, Wu X, Mulligan WP. High performance transparent conducting oxides based on cadmium stannate. Journal of Electronic Materials 1996;25(6):935–43.

[74] Born M, Wolf E. Principles of Optics: Electromagnetic Theory of Propagation, Interference and Diffraction of Light. Oxford, New York, Beijing, Frankfurt, São Paulo, Sydney, Tokyo, Toronto: Pergamon Press, 1985.

[75] Mulligan WP. A study of the fundamental limits to electron mobility in cadmium stannate thin films. Ph.D. thesis, Colorado School of Mines, Golden, Colorado, 1997.

[76] Dhere RG, Gessert TA, Schilling LL, Nelson AJ, Jones KM, Aharoni H, Coutts TJ. Electro-optical properties of thin indium tin oxide films: limitations on performance. Solar Cells 1987;21:281–90.

[77] Nozik AJ. Optical and electrical properties of Cd_2SnO_4: a defect semiconductor. Phys Rev B 1972;6(2):453–9.

[78] Charache GW, DePoy DM, Egley JL, Dziendziel RJ, Freeman MJ, Baldasaro PF, Campbell BC, Sharps PR, Timmons ML, Fahey RE, Zhang K, Borrego JM. Electrical and optical properties of degenerately-doped n-type $In_xGa_{1-x}As$. In: Coutts TJ, Allman CS, Benner JP, editors. The Third NREL Conference on the Thermophotovoltaic Generation of Electricity. Am Inst Phys Conf Series. New York: American Institute of Physics 1997;401:215–26.

[79] Rhoads CM, Damon EK, Munk BA. Mid-infrared filters using conducting elements. App Opt 1982;21(15):2814–16.

[80] Tomaselli VP, Edewaard DC, Gillan P, Moller, KD. Far-infrared bandpass filters from cross-shaped grids. App Opt 1981;20(8):1361–6.

[81] Horne WE, Morgan MD, Day AC. Radioisotope enhanced solar thermophotovoltaic power for the lunar surface. Solar Engineering 1992;2:861–5.

[82] Ebbesen TW, Lezec HJ, Ghaemi HF, Thio T, Wolff PA. Extraordinary optical transmission through sub-wavelength hole arrays. Nature 1998;391:667–9.

[83] Whitbourn LB, Compton RC. Equivalent-circuit formulas for metal grid reflectors at a dielectric boundary. App Opt 1985;24(2):217–20.

[84] Borrego J, Zierak M, Charache G. Parameter extraction for TPV cell development. In: Coutts TJ, Benner JP, editors. The First NREL Conference on the Thermophotovoltaic Generation of Electricity. Am Inst Phys Conf Series. New York: American Institute of Physics 1994;321:371–8.

[85] Wu X. Data on the performance of a back-surface reflector. Personal communication, 1998.

[86] Regan TM, Martin JG, Riccobono J. TPV conversion of nuclear energy for space applications. In: Coutts TJ, Benner JP, editors. The First NREL Conference on the Thermophotovoltaic Generation of Electricity. Am Inst Phys Conf Series. New York: American Institute of Physics 1994;321:321–30.

[87] Schock A, Kumar V. Radioisotope thermophotovoltaic system design and its applications to an

illustrative space mission. In: Coutts TJ, Benner JP, editors. The First NREL Conference on the Thermophotovoltaic Generation of Electricity. Am Inst Phys Conf Series. New York: American Institute of Physics 1994;321:139–52.
[88] Demichelis F, Minetti-Mezzetti E. A solar thermophotovoltaic converter. Solar Cells 1979/1980;1:395–403.
[89] Horne WE, Day AC, Gregor RB, Milliman LD. Solar thermophotovoltaic space power system. In: Silverman SW, editor. The 15th Intersociety Energy Conversion Engineering Conference. New York: American Institute of Aeronautics and Astronautics 1980;1:377–82.
[90] Stone KW, Kusek SM, Drubka RE, Fay TD. Analysis of solar thermophotovoltaic test data from experiments performed at McDonnell Douglas. In: Coutts TJ, Benner JP, editors. The First NREL Conference on the Thermophotovoltaic Generation of Electricity. Am Inst Phys Conf Series. New York: American Institute of Physics 1994;321:153–62.
[91] Pelka DG, Santos A, Yuen WW. Natural gas-fired thermophotovoltaic system. In: Berger C, editor. The 32nd International Power Sources Symposium. Electrochemical Society 1986;110–23.
[92] Schroeder KL, Rose MF, Burkhalter JE. An experimental investigation of hybrid kerosene burner configurations for TPV applications. In: Coutts TJ, Benner JP, editors. The First NREL Conference on the Thermophotovoltaic Generation of Electricity. Am Inst Phys Conf Series. New York: American Institute of Physics 1994;321:106–18.
[93] DeBellis CL, Scotto MV, Scoles SW, Fraas L. Conceptual design of 500 watt portable thermophotovoltaic power supply using JP-8 fuel. In: Coutts TJ, Allman CS, Benner JP, editors. The Third NREL Conference on the Thermophotovoltaic Generation of Electricity. Am Inst Phys Conf Series. New York: American Institute of Physics 1997;401:355–67.
[94] Demichelis F, Minetti-Mezzetti E, Agnello M, Perotto V. Bandpass filters for thermophotovoltaic conversion systems. Solar Cells 1982;5:135–41.
[95] Fraas LM, Ferguson L, McCoy LG, Pernisz UC. SiC ir emitter design for thermophotovoltaic generators. In: Benner JP, Coutts TJ, Ginley DS, editors. The Second NREL Conference on the Thermophotovoltaic Generation of Electricity. Am Inst Phys Conf Series. New York: American Institute of Physics 1995;358:488–94.
[96] Wedlock BD, Debs A, Siegel R, Taylor G. Investigation of germanium diodes for thermo-photovoltaic energy convertors, Final Technical Report DA 44-009-AMC-625(T). Fort Belvoir, Virginia: U.S. Army Research and Development Laboratories, 1965.
[97] Wojtczuk S, Gagnon E, Geoffroy L, Parodos T. $In_xGa_{1-x}As$ thermophotovoltaic cell performance vs bandgap. In: Coutts TJ, Benner JP, editors. The First NREL Conference on the Thermophotovoltaic Generation of Electricity. Am Inst Phys Conf Series. New York: American Institute of Physics 1994;321:177–87.
[98] Ballinger CT. New capabilities in the RACER-X photon Monte Carlo code for TPV applications, Internal TIS-RPC-97-2. Knolls Atomic Power Laboratory, 1997.
[99] Ballinger CT. Further comments on Monte Carlo modelling of the TPV optical cavity. Personal communication, 1998.
[100] Schroeder KL, Rose MF, Burkhalter JE. An improved model for TPV performance predictions and optimization. In: Coutts TJ, Allman CS, Benner JP, editors. The Third NREL Conference on the Thermophotovoltaic Generation of Electricity. Am Inst Phys Conf Series. New York: American Institute of Physics 1997;401:505–19.
[101] Stone KW, Chubb DL, Wilt DM, Wanlass MW. Testing and modeling of a solar thermophotovoltaic power system. In: Benner JP, Coutts TJ, Ginley DS, editors. The Second NREL Conference on the Thermophotovoltaic Generation of Electricity. Am Inst Phys Conf Series. New York: American Institute of Physics 1995;358:199–209.
[102] Schock A, Or C, Kumar V. Small radioisotope thermophotovoltaic (RTPV) generators. In: Benner JP, Coutts TJ, Ginley DS, editors. The Second NREL Conference on the Thermophotovoltaic Generation of Electricity. Am Inst Phys Conf Series. New York: American Institute of Physics 1997;358:81–97.
[103] Guazzoni G, McAlonan M. Multifuel (liquid hydrocarbons) TPV generator. In: Coutts TJ, Allman CS, Benner JP, editors. The Third NREL Conference on the Thermophotovoltaic Generation of Electricity. Am Inst Phys Conf Series. New York: American Institute of Physics 1997;401:341–54.

[104] Becker FE, Doyle EF, Shukla K. Development of portable thermophotovoltaic power generator. In: Coutts TJ, Allman CS, Benner JP, editors. The Third NREL Conference on the Thermophotovoltaic Generation of Electricity. Am Inst Phys Conf Series. New York: American Institute of Physics 1997;401:329–39.

[105] Fraas LM, Han Xiang H, Hui S, Ferguson L, Samaras J, Ballantyne R, Seal M, West E. Development of a small air-cooled 'Midnight Sun' thermophotovoltaic electric generator. In: Benner JP, Coutts TJ, Ginley DS, editors. The Second NREL Conference on the Thermophotovoltaic Generation of Electricity. Am Inst Phys Conf Series. New York: American Institute of Physics 1995;358:128–37.

[106] Schroeder KL, Rose MF, Burkhalter JE. A parametric study of TPV systems and the importance of thermal management in system design and optimization. In: Goswami DY, Kannberg LD, Mancini TR. et al., editors. The 30th Intersociety Energy Conversion Engineering Conference: Energy Technologies for a Sustainable Future. New York: American Society of Mechanical Engineering 1995;1:719–24.

[107] Chen Z, Adair PL, Rose MF. Selective emitters for thermophotovoltaic energy conversion—a study based on material prospects. In: The 31st Intersociety Energy Conversion Engineering Conference. Piscataway, NJ: IEEE 1996;2:1013–17.

[108] Kushch AS, Skinner SM, Brennan R, Sarmiento PA. Development of a cogenerating thermophotovoltaic powered combination hot water heather/hydronic boiler. In: Coutts TJ, Allman CS, Benner JP, editors. The Third NREL Conference on the Thermophotovoltaic Generation of Electricity. Am Inst Phys Conf Series. New York: American Institute of Physics 1997;401:373–86.

[109] Krist K. GRI research on thermophotovoltaics. In: Coutts TJ, Benner JP, editors. The First NREL Conference on the Thermophotovoltaic Generation of Electricity. Am Inst Phys Conf Series. New York: American Institute of Physics 1994;321:54–63.

[110] Fraas L, Avery J, Ballantyne R, Custard P, Ferguson L, Xiang HH, Keyes J, Mulligan B, Samaras J, Williams D. 2-amp TPV cogenerator using forced-air cooled gallium antimonide cells. In: Coutts TJ, Allman CS, Benner JP, editors. The Third NREL Conference on the Thermophotovoltaic Generation of Electricity. Am Inst Phys Conf Series. New York: American Institute of Physics 1997;401:369–72.

[111] Schock A, Or C, Mukunda M. Effect of expanded integration limits and of measured infrared filter improvements on performance of RTPV systems. In: Benner JP, Coutts TJ, Ginley DS, editors. The Second NREL Conference on the Thermophotovoltaic Generation of Electricity. New York: American Institute of Physics 1997;358:55–80.